

**INSTRUMENTATION OF A SUBMILLIMETRE WAVE  
HOLOGRAM COMPACT ANTENNA TEST RANGE**  
Thesis for the degree of Doctor of Science in Technology

**Jussi Säily**



TEKNILLINEN KORKEAKOULU  
TEKNISKA HÖGSKOLAN  
HELSINKI UNIVERSITY OF TECHNOLOGY  
TECHNISCHE UNIVERSITÄT HELSINKI  
UNIVERSITE DE TECHNOLOGIE D'HELSINKI

# **INSTRUMENTATION OF A SUBMILLIMETRE WAVE HOLOGRAM COMPACT ANTENNA TEST RANGE**

**Jussi Säily**

Dissertation for the degree of Doctor of Science in Technology to be presented with due permission for public examination and debate in Auditorium S4 at Helsinki University of Technology (Espoo, Finland) on the 19th of September 2003 at 12 o'clock noon.

**Helsinki University of Technology**

**Department of Electrical and Communications Engineering**

**Radio Laboratory**

**Teknillinen korkeakoulu**

**Sähkö- ja tietoliikennetekniikan osasto**

**Radiolaboratorio**

Distribution:

Helsinki University of Technology

Radio Laboratory

P.O.Box 3000

FIN-02015 HUT

Tel. +358-9-451 2252

Fax. +358-9-451 2152

© Jussi Säily and Helsinki University of Technology Radio Laboratory

ISBN 951-22-6689-X

ISSN 1456-3835

Otamedia Oy

Espoo 2003

## **Preface**

The work of this thesis has been carried out at the Radio Laboratory of the Helsinki University of Technology during 1997–2003.

I wish to thank Professor Antti Räisänen for the interesting research topic, support and guidance, and the opportunity to work in the Radio Laboratory all these years.

I would also like to thank all my co-workers in the Radio Lab for fruitful discussions and all the fun we've shared together. Especially I want to thank Mr. Ville Möttönen, Professor Pekka Eskelinen, and the hologram research group members Dr. Juha Ala-Laurinaho, Mr. Janne Häkli, Ms. Anne Lönnqvist, Mr. Tomi Koskinen, and Professor Jussi Tuovinen.

The valuable suggestions and corrections for improving this thesis from the pre-examiners, Professor Neal Erickson and Dr. Taavi Hirvonen, are also greatly appreciated.

This work was financed by Academy of Finland, European Space Agency, National Technology Agency (TEKES), Helsinki University of Technology, and the Graduate School of Electronics, Telecommunication and Automation (GETA). I have also received personal research grants from Foundation of Technology (TES), Foundation of the Finnish Society of Electronics Engineers (EIS), Nokia Foundation, and the Finnish Cultural Foundation. Their support is warmly appreciated.

Finally, I would like to thank my wife Katja, my daughter Silja, and my parents for their support and endurance during my studies and thesis work.

Espoo, August 6th, 2003

Jussi Säily

## **Abstract**

This thesis presents the developed instrumentation and measurement techniques suitable for use in a submillimetre wave compact antenna test range (CATR) for testing high-gain antennas and the quiet-zone quality of the CATR, but also for use in antenna testing with planar near-field scanning at submillimetre wavelengths. The thesis work is focused on improving the phase measurement accuracy and the dynamic range of a commercial submillimetre wave vector network analyser. The full angular scattering properties of radiation absorbing materials (RAM) suitable for the CATR are also analysed in the thesis.

A CATR can be used for testing of electrically large antennas at millimetre and submillimetre wavelengths. These high-gain dish antennas are required for spaceborne astronomy and limb sounding of the Earth atmosphere. The most common CATR configuration at millimetre waves uses a reflector as the collimating element. However, the surface accuracy requirement of the reflector becomes very stringent at frequencies over 200 GHz, and the manufacturing of the reflector thus very expensive. An alternative collimator to the reflector is the binary amplitude hologram which is studied in this thesis. The hologram is a planar transmission type device, which is realised as a slot pattern on a metallised dielectric film. The surface (pattern) accuracy requirement of the hologram is less stringent than that of a reflector and it is potentially of lower cost. The amplitude and phase ripples of the CATR quiet-zone field need to be below  $\pm 0.5$  dB and  $\pm 5^\circ$ . The hologram CATR operating at 310 GHz discussed in this thesis is shown to be able to achieve these limits even at submillimetre wavelengths.

The amplitude and phase measurement accuracies of a vector network analyser largely depend on the strength of the detected signal. The quiet-zone tests of planned large hologram CATRs require larger dynamic range than is possible with the standard solid-state source configuration, so a phase-lock system for submillimetre wave backward-wave oscillators (BWO) had to be developed. The powerful phase-locked BWO source described in this thesis can improve the dynamic range and the accuracy of the measurement system considerably. The improvement in dynamic range over the standard source based on a frequency-multiplied Gunn oscillator is 16–40 dB over the frequency range of 300–700 GHz.

Problems in the phase measurement accuracy arise when the receiver is moved across the quiet-zone area with microwave cables connected to it. The flexing of the cables causes phase errors reaching tens of degrees due to changes in their electrical lengths. The novel phase error measurement and correction system described in this thesis is based on the use of a pilot signal to track changes in the electrical length of a microwave cable. The error analysis shows that phase correction of the detected submillimetre wave signal is possible down to a level of  $2^\circ$  with the constructed system. Accurate operation has also been verified by measurements.

The CATR facility needs large quantities of high-performance absorbers. In order to select suitable absorbers, the specular and non-specular reflectivities of several commercially available, state-of-the-art absorber materials have been measured between 200–600 GHz. Selected wool and synthetic floor carpet materials were also included in the tests. The results show that specular reflectivities between  $-40\dots-50$  dB are possible over a considerable angular range when the materials are oriented properly. The best floor carpet materials have reflectivities below  $-15$  dB over a wide angular range and are useful in the less critical areas by reducing backscatter. The published report is the first in the open literature showing the full angular performance of these materials across a wide frequency range.

## List of Publications

This thesis is based on the work presented in the following papers:

- [P1] J. Säily, P. Eskelinen, A.V. Räisänen, "Pilot signal based real-time measurement and correction of phase errors caused by microwave cable flexing in planar near-field tests", *IEEE Transactions on Antennas and Propagation*, Vol. 51, No. 2, Feb. 2003, pp. 195–200
- [P2] J. Säily, J. Ala-Laurinaho, J. Häkli, J. Tuovinen, A. Lehto, A.V. Räisänen, "Test results of a 310 GHz hologram compact antenna test range", *Electronics Letters*, Vol. 36, No. 2, 2000, pp. 111–112
- [P3] J. Säily, J. Ala-Laurinaho, J. Häkli, T. Koskinen, A. Lönnqvist, J. Tuovinen, A.V. Räisänen, "Measuring satellite antennas with a compact hologram test range", *IEEE Aerospace and Electronic Systems Magazine*, Vol. 17, No. 5, May 2002, pp. 13–19
- [P4] J. Ala-Laurinaho, T. Sehm, J. Säily, A.V. Räisänen, "Cross-polarization performance of the hologram CATR", *Microwave and Optical Technology Letters*, Vol. 27, No. 4, 2000, pp. 225–229
- [P5] J. Säily, J. Mallat, A.V. Räisänen, "Using a phase-locked backward wave oscillator to extend the dynamic range of a vector network analyzer", *Proceedings of the 31<sup>st</sup> European Microwave Conference*, London, UK, Sept. 24-28, 2001, pp. 57–60
- [P6] J. Säily, A.V. Räisänen, "Studies on specular and non-specular reflectivities of radar absorbing materials (RAM) at submillimetre wavelengths", *Report S 258*, Helsinki University of Technology Radio Laboratory Publications, February, 2003, 66 pages

Contribution of the author in [P1-P6] is presented on the next page. Furthermore, the author of this thesis has authored or co-authored 43 other papers [O1-O43] relevant to the topic of this thesis.

## **Contribution of the Author**

Paper [P1] was mainly contributed by the author. Professor Eskelinen assisted in developing the measurement instrumentation. Professor Räsänen supervised the instrument development and writing of the manuscript.

Paper [P2] is a result of collaborative work. The author developed the measurement instrumentation, constructed the range in the laboratory, and was responsible for all the measurements. Mr. Häkli assisted in some of the measurements. Dr. Ala-Laurinaho designed the hologram for the range, ran the simulations, and was responsible for the hologram manufacturing. Professor Tuovinen, Dr. Lehto, and Professor Räsänen supervised the work.

Paper [P3] is a result of collaborative work. The author is responsible for writing most of the manuscript. Dr. Ala-Laurinaho contributed the Odin satellite measurements results, Mr. Häkli the dual reflector feed system (DRFS) simulation results, Mr. Koskinen the 322 GHz and 650 GHz hologram designs, and Ms. Lönnqvist to the measurement instrumentation. Professors Tuovinen and Räsänen supervised the work.

Paper [P4] is a result of collaborative work. Dr. Ala-Laurinaho is responsible for the manuscript and the hologram designs and simulation results. Dr. Sehm assisted in the 39 GHz planar link antenna measurements. The author developed the submm wave near-field measurement system and was responsible for the 310 GHz measurements.

Paper [P5] was mainly contributed by the author. Dr. Mallat and Professor Räsänen supervised the development work.

Paper [P6] was mainly contributed by the author. Professor Räsänen supervised the research work and assisted in preparing the report.

## Contents

<b>PREFACE</b> .....	<b>3</b>
<b>ABSTRACT</b> .....	<b>4</b>
<b>LIST OF PUBLICATIONS</b> .....	<b>5</b>
<b>CONTRIBUTION OF THE AUTHOR</b> .....	<b>6</b>
<b>CONTENTS</b> .....	<b>7</b>
<b>SYMBOLS</b> .....	<b>9</b>
<b>ABBREVIATIONS</b> .....	<b>12</b>
<b>1 INTRODUCTION</b> .....	<b>14</b>
1.1    GENERAL.....	14
1.2    SCOPE AND CONTENTS OF THIS THESIS.....	15
1.3    NEW SCIENTIFIC RESULTS.....	15
<b>2 PRINCIPLES AND TECHNIQUES OF ANTENNA MEASUREMENTS</b> .....	<b>16</b>
2.1    ANTENNA CHARACTERISTICS.....	16
2.1.1    Measured parameters for antennas.....	17
2.2    ANTENNA TESTING TECHNIQUES.....	19
2.3    FAR-FIELD MEASUREMENTS.....	20
2.4    NEAR-FIELD SCANNING MEASUREMENTS.....	20
2.4.1    Planar near-field measurements.....	21
2.4.2    Cylindrical and spherical near-field measurements.....	22
2.5    COMPACT RANGES.....	23
2.5.1    Reflector CATRs.....	23
2.5.2    Lens CATRs.....	26
2.5.3    Hologram CATR.....	27
2.6    OTHER METHODS.....	28
<b>3 MILLIMETRE AND SUBMM WAVE VECTOR NETWORK ANALYSER</b> .....	<b>31</b>
3.1    DESCRIPTION OF OPERATION.....	31
3.2    SOURCE SYSTEM.....	32
3.2.1    ABmm ESA-1 transmitter.....	32
3.3    RECEIVER SYSTEM.....	33
3.3.1    ABmm ESA-2 receiver.....	34
3.4    DYNAMIC RANGE AND MEASUREMENT ACCURACY.....	34
<b>4 PHASE-LOCKED OSCILLATORS</b> .....	<b>37</b>
4.1    THE IMPORTANCE OF PHASE-LOCKED SOURCES FOR VECTOR ANTENNA MEASUREMENTS.....	37
4.2    PHASE NOISE CHARACTERISTICS OF OSCILLATORS AND PLL SYSTEMS.....	37
4.3    PHASE-LOCKED LOOP FUNDAMENTALS.....	39
4.3.1    Loop transfer functions.....	39
4.3.2    Phase-lock acquisition.....	41
4.4    MODELING AND DESIGN OF A PHASE-LOCKED BWO SOURCE FOR 180–714 GHz.....	43
4.4.1    Operating principle of the BWO.....	43

4.4.2	<i>Design of the BWO-PLL</i> .....	44
4.4.2.1	Loop filter.....	44
4.4.2.2	PLL signal coupling to the BWO.....	46
4.4.3	<i>APLAC circuit simulator model of the BWO-PLL</i> .....	47
4.4.4	<i>Construction and testing of the BWO-PLL</i> .....	48
4.5	ASSOCIATION OF THE BWO TO THE SUBMM-WAVE VECTOR NETWORK ANALYSER...	50
4.5.1	<i>Measured dynamic range improvement over the standard source system</i> .....	51
<b>5</b>	<b>PHASE-CORRECTION SYSTEM FOR PLANAR NEAR-FIELD MEASUREMENTS</b> .....	<b>53</b>
5.1	PHASE AND AMPLITUDE EFFECTS OF REFERENCE CABLES.....	53
5.2	CONSTRUCTION OF THE PHASE-CORRECTION SYSTEM.....	54
5.2.1	<i>Description of operation</i> .....	54
5.2.3	<i>Error analysis</i> .....	55
5.3	MEASUREMENT RESULTS.....	61
5.4	DISCUSSION.....	65
<b>6</b>	<b>ABSORBER MATERIALS</b> .....	<b>66</b>
6.1	INTRODUCTION.....	66
6.1.1	<i>Tested materials</i> .....	66
6.2	SPECULAR SCATTERING MEASUREMENTS AT 200–600 GHz.....	67
6.3	NON-SPECULAR SCATTERING MEASUREMENTS AT 300 AND 400 GHz.....	68
6.4	CONCLUSIONS.....	68
<b>7</b>	<b>COMPACT ANTENNA TEST RANGE DESIGN</b> .....	<b>70</b>
7.1	TESTING ENVIRONMENT FOR SUBMM-WAVE CATRS.....	70
7.2	INSTRUMENTATION.....	71
<b>8</b>	<b>SUMMARY OF PUBLICATIONS</b> .....	<b>72</b>
<b>9</b>	<b>DISCUSSION AND CONCLUSIONS</b> .....	<b>74</b>
	<b>ERRATA</b> .....	<b>77</b>
	<b>REFERENCES</b> .....	<b>78</b>

## Symbols

$\bar{a}$	maximum error vector in cable phase correction
$A$	amplitude [V], DC gain of an operational amplifier
$\bar{b}$	vector with the wanted information in cable phase correction
$c$	speed of light, $2.998 \cdot 10^8$ m/s
$C$	capacitance [F]
$d$	distance [m]
$d\Omega$	elementary unit of the solid angle [rad]
$D$	the largest dimension of an antenna [m], directivity [dB]
$E_R$	received electrical field
$E_T$	transmitted electrical field
$\bar{E}$	electric field vector
$E(\theta, \phi)$	electrical field strength in spherical coordinates [V/m]
$f$	frequency [Hz]
$f(t)$	ideal signal in time domain [V]
$f_0$	reference frequency for the receiver Gunn-PLL [Hz]
$f_1$	1 <sup>st</sup> local oscillator frequency (transmitter) [Hz]
$f_2$	2 <sup>nd</sup> local oscillator frequency (receiver) [Hz]
$f_A$	frequency of the Gunn oscillator in the transmitter [Hz]
$f_B$	frequency of the Gunn oscillator in the receiver [Hz]
$f_c$	frequency of a signal [Hz]
$f_m$	frequency separation from the carrier frequency [Hz]
$f_{mm}$	output frequency of the MVNA transmitter [Hz]
$f_n(t)$	signal containing amplitude and phase noise in time domain [V]
$f_R$	intermediate frequency for the vector receiver [Hz]
$f_s$	reference frequency for the transmitter Gunn-PLL [Hz]
$F(\infty)$	loop filter gain at infinity
$F(0)$	loop filter DC gain
$F(s)$	loop filter transfer function
$F_a(s)$	loop filter transfer function using an active lag-lead filter
$g_e$	cable gain factor
$G$	gain of an antenna [dB]
$H_\phi(s)$	closed loop phase error transfer function
$H_\theta(s)$	closed loop phase transfer function
$H_{\theta,a}(s)$	closed loop phase transfer function using an active loop filter
$\bar{H}^*$	complex conjugate of the magnetic field vector
$k$	harmonic number in the Gunn-PLL downconversion
$K_d$	phase detector gain [V/rad]
$K_o$	VCO gain [rad/sV]
$l$	cable length [m]
$L_{hm}$	conversion loss of the receiver [dB]
$L_{SSB}(f_m)$	single sideband phase noise in a 1 Hz bandwidth [dBc/Hz]
$M$	integer number
$n_1(t)$	amplitude unstability coefficient

$N$	integer number
$P(\theta, \phi)$	radiated power density of an antenna in spherical coordinates
$P_{mm}$	transmitter power [dBm]
$P_n$	noise floor of the vector receiver [dBm]
$P_n(\theta, \phi)$	normalised radiated power density of an antenna in spherical coordinates
$r$	the far-field distance of an antenna [m]
$R_1, R_2$	resistors of an active loop filter [ $\Omega$ ]
$s$	Laplace operator, $s=j\omega$
$\bar{S}$	complex Poynting vector
$S/N$	signal-to-noise ratio [dB]
$t$	time [s]
$T_1$	forward transmission coefficient
$T_2$	backward transmission coefficient
$\overline{T_P(\Delta\omega)}$	pull-in time from the pull-in range to the edge of the lock-in range [s]
$\bar{u}_\theta, \bar{u}_\phi$	unit vectors in the spherical coordinate system
$v_c$	VCO control voltage [V]
$v_d$	output voltage from the phase detector [V]
$x, y, z$	coordinate axes in a rectangular coordinate system
$\beta$	propagation coefficient [rad/m]
$\Gamma_1, \Gamma_2, \Gamma_3$	complex reflection coefficients
$ \Delta f_{hold} $	hold range of a PLL [Hz]
$ \Delta f_L $	lock-in range of a PLL [Hz]
$ \Delta f_P $	pull-in range of a PLL [Hz]
$\Delta f / \Delta V$	VCO gain [Hz/V]
$\Delta\phi$	phase error after correction [ $^\circ$ ]
$\Delta\phi_{max}$	maximum phase error after correction [ $^\circ$ ]
$\Delta\omega$	initial angular frequency error of the VCO [rad/s]
$\epsilon_r$	relative dielectric constant
$\eta_p$	polarisation efficiency of an antenna
$\eta_r$	radiation efficiency of an antenna
$\theta$	elevation angle [ $^\circ$ ], electrical length of the cable [rad],
$\theta_l$	angle between $\bar{a}$ and $\bar{b}$ [ $^\circ$ ]
$\theta_e(s)$	phase difference between the input and the VCO signals [rad]
$\theta_i$	incident angle in the reflectivity measurements [ $^\circ$ ]
$\theta_i(s)$	phase of the input (reference) signal [rad]
$\theta_o$	receiving angle in the reflectivity measurements [ $^\circ$ ]
$\theta_o(s)$	phase of the VCO output signal [rad]
$\lambda$	wavelength [m]
$\xi_a$	damping factor of a PLL using an active loop filter
$\rho_1$	magnitude of reflection coefficient $\Gamma_1$
$\rho_3$	magnitude of reflection coefficient $\Gamma_3$
$\tau_1, \tau_2$	time constants of a loop filter [s]
$\tau_{1a}, \tau_{2a}$	time constants of an active loop filter [s]

---

$\phi$	azimuth angle [°]
$\phi_1$	phase angle of reflection coefficient $\Gamma_1$ [°]
$\phi_3$	phase angle of reflection coefficient $\Gamma_3$ [°]
$\phi_n(t)$	phase instability coefficient
$\psi(\theta, \phi)$	phase pattern of an antenna in spherical coordinates [°]
$\omega_1$	angular frequency of the first loop filter pole [rad/s]
$\omega_2$	angular frequency of the stabilizing zero for the loop filter [rad/s]
$\omega_3$	unity gain angular frequency of the loop filter [rad/s]
$\omega_{n,a}$	loop natural angular frequency with an active loop filter [rad/s]

## Abbreviations

AC	Alternating Current
AM	Amplitude Modulation
APLAC	Analysis Program for Linear Active Circuits, general purpose circuit simulator
AUT	Antenna-under-test
BWO	Backward-wave Oscillator
CATR	Compact Antenna Test Range
dB	Decibel
D-band	110–170 GHz
DC	Direct Current
DRFS	Dual Reflector Feed System
DVM	Digital Volt Meter
EOS MLS	Earth Observing System Microwave Limb Sounder
ESA	European Space Agency
ESA-1	External Source Association 1, transmitter
ESA-2	External Source Association 2, receiver
EVA	Ethylene Vinyl Acetate
FDTD	Finite Difference Time Domain
FF	Far-field
FFT	Fast Fourier Transform
FIRST	Far-Infrared and Submillimeter Telescope
FM	Frequency Modulation
GPIB-bus	General Purpose Instrument Bus
GPS	Global Positioning System
HM	Harmonic Mixer
HUT	Helsinki University of Technology
IF	Intermediate Frequency
LNA	Low Noise Amplifier
LPF	Loop Filter
MASTER	Millimeter-wave Acquisitions for Stratosphere/Troposphere Exchanges Research
MilliLab	Millimetre Wave Laboratory of Finland
mm wave	Millimetre Wave
MVNA	Millimetre Wave Vector Network Analyser
NF	Near-field
PA	Power Amplifier
PCB	Printed Circuit Board
PD	Phase Detector
PIRAMHYD	Passive Infrared Atmospheric Measurements of Hydroxyl
PLL	Phase-locked Loop
PM	Phase Modulation
PO	Physical Optics
RAM	Radiation Absorbing Material
RCS	Radar Cross Section
RF	Radio Frequency
RMS	Root Mean Square
SCATR	Semi-compact Antenna Test Range

---

SNR	Signal-to-Noise Ratio
SOPRANO	Sub-millimetric Observation of Processes in the Atmosphere Noteworthy for Ozone
SPCR	Single-plane Collimating Range
SSB	Single Sideband
submm wave	Submillimetre Wave
SWAS	Submillimeter Wave Astronomy Satellite
TWT	Traveling Wave Tube
V-band	50–75 GHz
VCO	Voltage Controlled Oscillator
VLBI	Very Large Baseline Interferometry
VNA	Vector Network Analyser
VSWR	Voltage Standing Wave Ratio
W-band	75–110 GHz
WR-3	Standard rectangular waveguide for 220–325 GHz
WR-8	Standard rectangular waveguide for 90–140 GHz
WR-10	Standard rectangular waveguide for 75–110 GHz
YIG	Yttrium Iron Garnet

# 1 Introduction

## 1.1 General

In the next 10–15 years, many scientific satellites carrying millimetre (30–300 GHz) and submillimetre (>300 GHz) wave instruments and antennas will be launched. The European Space Agency (ESA) shall have several missions for spaceborne astronomy (Herschel Space Observatory/FIRST, Planck Surveyor) and limb sounding of the Earth atmosphere (MASTER, SOPRANO, PIRAMHYD) [1]. The diameters of the reflector antennas are from 0.5 to 3.5 meters and they operate in the frequency range of 200–3000 GHz. Limb sounders are used to monitor atmospheric processes like the greenhouse effect and ozone depletion. Astronomy space missions use this frequency band because most of the fundamental absorption and emission lines of astrochemically significant molecules like water and oxygen exist there. The Earth atmosphere makes it impossible to observe these lines from the ground. Spaceborne radiotelescope observations of many distant galaxies are not impaired by interstellar dust like in the optical region. Formation of galaxies and the origin of the Universe are best studied in this wavelength region where most of the emitted and the background radiation occurs.

Antennas are generally required to be tested in the far-field conditions. The required far-field distance of an electrically large antenna at 1 THz can be tens of kilometers. High atmospheric attenuation and signal distortion due to temperature and humidity variations along the required distance make conventional far-field measurements impossible. The most practical test methods are the compact antenna test range (CATR) and near-field scanning methods [2]. Both of these allow accurate characterisation of the antennas indoors with controlled atmosphere and humidity.

The compact antenna test range simulates far-field conditions by transforming the spherical wave radiated by a feed horn into a plane wave. The collimating element can be a reflector, a lens, or a hologram. Reflector CATRs have been used for frequencies up to 200 GHz [3], the surface accuracy of the reflector being the limiting factor. Calibration measurements up to 500 GHz have been conducted on the same CATR by measuring the reflector surface inaccuracies and removing their effect computationally [4]. Dielectric lenses are not suitable for submillimetre wave CATR operation because of material inhomogeneity and manufacturing problems associated with large lenses. The hologram CATR is a relatively new concept developed in the Radio Laboratory of the Helsinki University of Technology [5]. It has significantly less stringent surface accuracy demands compared to reflectors and is potentially of lower cost. Submillimetre wave operation of the hologram CATR has also been demonstrated [P2,P3].

The near-field scanning method is based on measuring the radiating near-field of the antenna from which the far-field radiation pattern can be derived mathematically. For electrically large antennas, the scanning grid becomes very dense and accurate positioning of the receiver difficult. Also the requirement for instrument stability during long scanning times can cause problems. The near-field scanning method has been used for measuring antennas with operating frequencies up to 650 GHz [6].

## **1.2 Scope and contents of this thesis**

This thesis summarises the development of new measurement techniques and submillimetre wave instrumentation aimed for accurate testing of the hologram CATR. The developed instrumentation can be applied also to other CATR and planar near-field scanning methods. The research has been carried out in the Radio Laboratory of the Helsinki University of Technology. In this thesis work the main emphasis has been on developing new measurement techniques, including correction of phase errors due to flexing cables, improving the dynamic range of vector measurements, and absorber reflectivity characterisation.

Chapter 2 discusses the basic principles and techniques of antenna measurements, including CATRs and near-field techniques. Chapter 3 presents the operation and performance of the submillimetre wave vector network analyser used in the measurement system. Phase-locked loop fundamentals and the development of a phase-locked backward-wave oscillator (BWO) source for use with the vector network analyser are presented in Chapter 4. Chapter 5 describes the constructed phase error measurement and correction system for near-field scanning measurements at submillimetre waves. Chapter 6 discusses the properties and shows the measured reflectivities for several commercially available submillimetre wave absorber materials. The design for a large-sized hologram CATR facility for the frequency range of 300–1000 GHz is presented in Chapter 7. Summary of publications is presented in Chapter 8, and conclusions in Chapter 9.

## **1.3 New scientific results**

The work presented in this thesis has produced new knowledge in the following areas:

- 1) The feasibility of a compact antenna test range based on an amplitude hologram has been demonstrated at the submm-wave region.
- 2) A pilot signal based real time correction of phase errors due to cable flexing in near-field scanning has been introduced and developed.
- 3) The full specular and non-specular scattering performance at frequencies from 200 to 600 GHz of several widely used absorbing materials has been measured and presented.
- 4) The BWO has been for the first time used to extend the dynamic range of a vector network analyser in the submm-wave region.

## 2 Principles and techniques of antenna measurements

### 2.1 Antenna characteristics

An antenna is a certain structure which launches guided electromagnetic waves into free-space propagation and vice versa. Transmit and receive antennas can be found on almost every application of radio engineering. Accurate knowledge of the antenna properties is vital for designing efficient communications devices and systems. A poorly designed antenna may disturb the performance of an otherwise good device. Most antennas are reciprocal, so they can be tested in either receiving or transmitting mode. However, if active, nonlinear, or nonreciprocal elements are present, the assumption may not be valid and the antenna must be tested in the intended configuration.

The complex Poynting vector  $\bar{S} = \bar{E} \times \bar{H}^*$  is used to characterise the radiation field from an antenna, and it has components which decay with distance as  $1/r$ ,  $1/r^2$ , and  $1/r^3$  [7,8]. The field can be separated into reactive near-field, radiating near-field, and radiating far-field regions. The reactive near-field is the region where the imaginary (non-radiating) component of the Poynting vector dominates, and decays rapidly as  $1/r^2$  or  $1/r^3$ . Reactive near-field typically exists only within a few wavelengths from the antenna. For the special case of an electrically small dipole (Hertzian dipole), the field components decaying with  $1/r$  and  $1/r^2$  are equal in magnitude at a distance of  $\lambda/2\pi$ . This distance is commonly used as the point after which the radiating fields dominate.

The radiating region can be separated into the radiating near-field (Fresnel) and the far-field (Fraunhofer) parts. The former exists for most electrically large antennas, but the latter for all types of antennas. The radiating fields decay as  $1/r$  when moving away from the antenna. The two regions are separated by the dependence of the angular field distribution on distance. In the radiating near-field where the Poynting vector has both real and imaginary components, the angular field distribution changes as a function of distance. In the far-field where the Poynting vector is real (radiating field), the angular field distribution remains constant over distance, and a spherical wavefront propagates along the main beam direction of the antenna. The reactive and radiating fields are illustrated in Figure 2.1 [8].

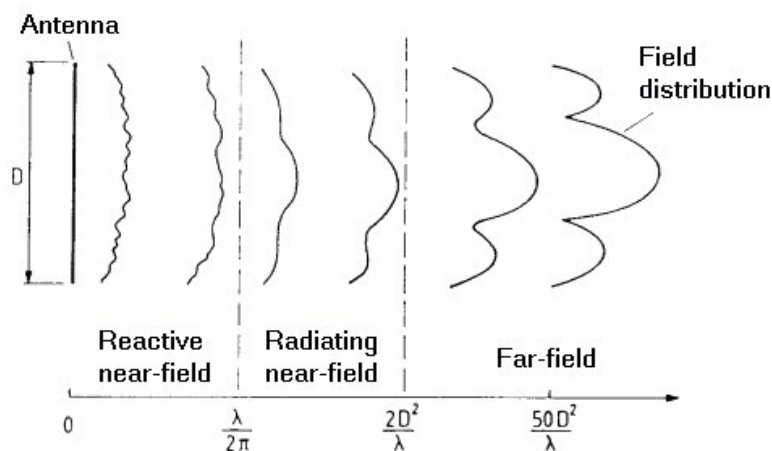


Figure 2.1 The antenna radiation regions and corresponding distances.

Antenna measurements are usually carried out in the far-field, indicating a long distance between the transmit and receive antennas. In the far-field, a plane wave (actually a part of the spherical wavefront) can be thought to illuminate the antenna-under-test (AUT). The far-field distance for electrically large antennas is usually defined as

$$r \geq \frac{2D^2}{\lambda}, \quad (2.1)$$

where  $D$  is the largest dimension of the antenna along the illumination direction normal and  $\lambda=c/f$  the wavelength [7]. The phase variation across the antenna surface at this distance is  $22.5^\circ$  if the radiation originates from an omnidirectional point source. The phase variation is caused by the different path lengths of the rays reaching the antenna. A better plane wave, i.e., smaller phase error of less than  $10^\circ$ , maybe required for testing highly directive antennas [2].

Equation (2.1) shows that the far-field distance increases with frequency (frequency is inversely proportional to the wavelength). At millimetre and submillimetre wavelengths there exist also several molecular resonance frequencies, which can cause signal attenuation up to thousands of decibels per kilometer. The available transmit power from millimetre and submillimetre wave signal sources is limited when compared to microwave sources, so conventional far-field measurement methods are ruled out by the strong attenuation and atmospheric disturbances over the required distance. Several new test methods have been developed to overcome the limited dynamic range of far-field measurements, including near-field scanning and compact antenna test range methods. Antenna test methods are discussed further in Sections 2.2–2.6.

### 2.1.1 Measured parameters for antennas

The antenna parameters to be measured are usually linked to the intended application. For the simplest applications, only the E- and H-plane directional patterns or the antenna gain need to be known. Other important electrical parameters include directional pattern in the diagonal plane, directivity, phase pattern, polarisation, impedance, efficiency, and bandwidth. Important mechanical properties include, e.g., weight and size of the antenna assembly. Figure 2.2 shows the spherical coordinate system commonly used in defining the antenna electrical parameters [7]. In this coordinate system, the angle  $\theta$  (elevation) increases along the circle from the positive  $z$ -axis ranging from  $0$  to  $180^\circ$ . The angle  $\phi$  (azimuth) is defined as the angle between the  $xy$ -plane projection of the direction vector and the positive  $x$ -axis. The azimuth angle ranges from  $0$  to  $360^\circ$  starting from the positive  $x$ -axis and increasing to the counter-clockwise direction. The origin of the coordinate system is usually set based on the structure of the antenna-under-test (AUT).

The directional pattern of an antenna shows the angular dependence of the radiated power density  $P(\theta, \phi)$  or the electrical field strength  $E(\theta, \phi)$  (the square root of power density). The directional pattern is usually normalised, and the maximum of the main beam is marked as 1 (0 dB). For example, the main beam and side lobe locations, half power beamwidth, and null locations are readily seen from the directional pattern. If the normalised directional pattern  $P_n(\theta, \phi)$  is known, the directivity of the antenna can be calculated by integrating over the full  $4\pi$  solid angle as

$$D = \frac{4\pi}{\iint_{4\pi} P_n(\theta, \phi) d\Omega}, \quad (2.2)$$

where  $d\Omega$  is the elementary unit of the solid angle [8].

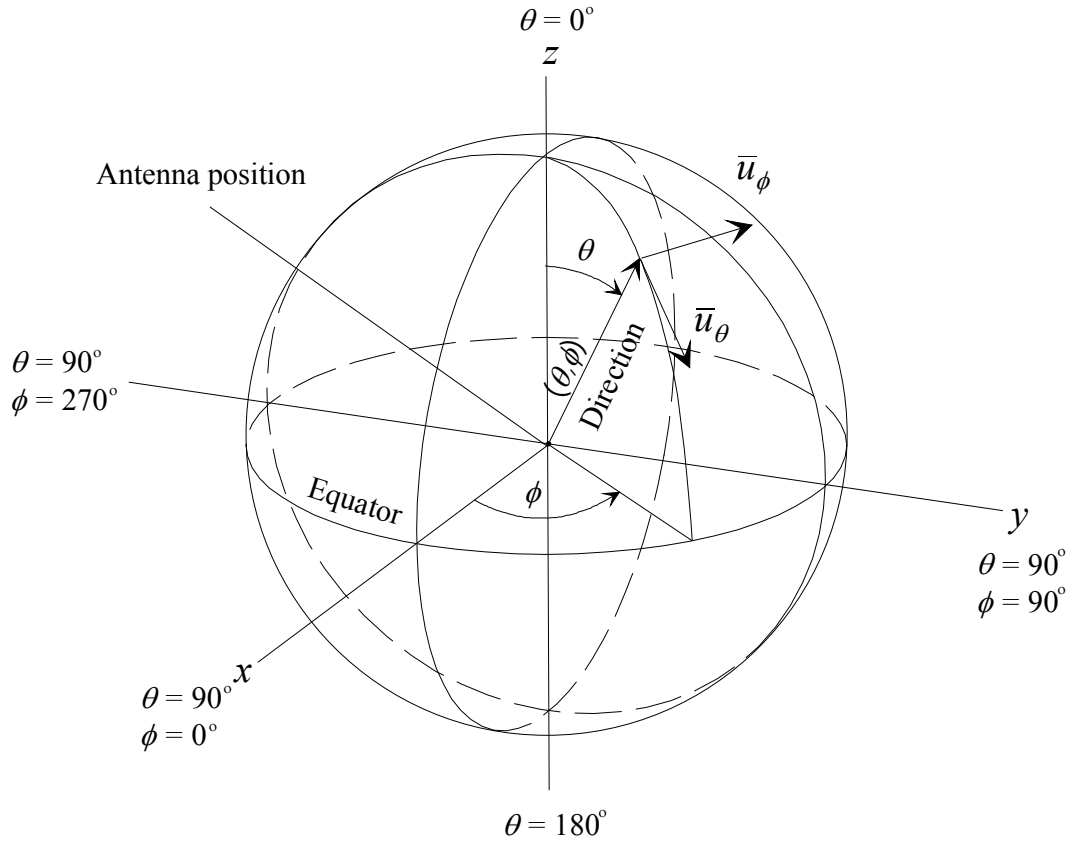


Figure 2.2 The spherical coordinate system used in antenna measurements [7].

The gain of an antenna is defined as the ratio between its radiated power density and the power density of a lossless isotropic antenna, when both antennas have the same input power [8]. The gain of a lossless antenna equals its directivity. The gain of an antenna is related to its directivity through the formula

$$G = \eta_r D, \quad (2.3)$$

where  $\eta_r$  is the radiation efficiency. The gain of a real antenna is always less than its directivity. The directivity and gain as functions of the pointing angle can be calculated by multiplying the formulas by the normalised directional pattern  $P_n(\theta, \phi)$ . Gain transfer or gain comparison measurements using a known reference antenna are the most common way of determining the antenna gain [9]. If the resistive and mismatch losses of the antenna can be measured separately, the directivity can easily be calculated from (2.3).

The phase pattern  $\psi(\theta, \phi)$  of an antenna is given as a function of the directional angle and tells how its radiated phase front differs from an ideal spherical wavefront. The phase pattern is related to a certain reference point where the spherical wavefront is thought to be originated. Phase centre is the reference point where the phase error along the main beam

region is minimized. Accurate knowledge of the location of the phase centre is important for design of reflector antennas.

The behaviour of the electric field vector direction for an antenna as a function of the directional angle  $(\theta, \phi)$  is called the polarisation of the antenna. During one cycle, the tip of the vector is thought to draw an ellipse in a plane orthogonal to the propagation direction. Special cases of this so-called elliptical polarisation are the linear and circular polarisations. Furthermore, based on the direction of rotation, the polarisations are divided into right-hand (clockwise) and left-hand (counter clockwise) polarisations.

Antennas are usually designed to operate only on a single polarisation which is called the main polarisation. An orthogonal polarisation to this is called the cross-polarisation. For example, the cross-polarisation of the horizontal linear polarisation is the vertical linear polarisation. Similarly, the cross-polarisation of the right-handed circular polarisation is the left-handed circular polarisation. The cross-polarisation level of an antenna is especially important in many communications systems, where different signals are transmitted at the same frequency but with orthogonal polarisations. For efficient reception, the polarisation of the received signal should be the same as the antenna polarisation. The polarisation mismatch is given as the polarisation efficiency  $\eta_p$  [8].

Power is coupled to the antenna from a waveguide, and the impedance mismatch between them causes reflections and coupling losses. In practice, perfect matching of the antenna is not possible because the antenna impedance is affected by its environment. For example, reflected signals from the surroundings and couplings between different antenna array elements may change the effective antenna impedance.

Finally, the antenna bandwidth is defined as the frequency range where the wanted specifications for, e.g., matching, gain, beamwidth, and cross-polarisation are met.

## **2.2 Antenna testing techniques**

An antenna test range is a facility dedicated to the measurements of the electrical properties of antennas. The test range includes also the necessary measurement equipment, mechanical positioners and controllers. Commonly used test ranges using the far-field techniques include the free-space range, ground reflection range, anechoic chamber, and various compact antenna test ranges [9]. The far-field techniques are based on getting flat amplitude and phase responses across the whole aperture of the antenna-under-test. Also near-field scanning methods can be used to measure the antenna parameters.

An anechoic chamber is a room whose walls, floor, and ceiling are covered with radiation absorbing material (RAM) in order to prevent reflections. The anechoic chamber is suitable for measuring electrically small antennas for which the far-field distance is relatively small. The compact range and near-field methods have the advantage that measurements of also electrically large antennas can be done indoors in a controlled environment. The CATR and near-field measurements should be done inside an anechoic chamber to prevent reflections from the enclosure walls.

Compact antenna test ranges are based on transforming the amplitude and phase of an incoming spherical wave into that of a plane wave [9]. The volume where the accurate plane wave is present is called the quiet-zone of the CATR. The requirements for the quiet-zone

amplitude and phase ripples are usually  $\pm 0.5$  dB and  $\pm 5^\circ$ , respectively [2]. The collimating element may be a reflector (or a set of reflectors), a lens, or a hologram. These are discussed in more detail in Section 2.5.

In the near-field scanning methods, a small-sized known probe antenna is used to sample the radiating near-field across the aperture of the AUT [9]. Different scanning geometries include planar, cylindrical, and spherical near-field methods. The far-field directional pattern of the AUT can be calculated by Fourier transforming the measured near-field data. The near-field methods are discussed in more detail in Section 2.4.

### 2.3 Far-field measurements

The far-field method is the oldest and the most straightforward antenna measurement technique. Generally, the transmit and receive antennas are located far from each other so that an accurate enough plane wave is present across the aperture of the AUT. The required far-field distance can be calculated from (2.1). Table 2.1 shows the calculated far-field distances for some typical antenna sizes at frequencies of 1–1000 GHz. For example, the far-field distance of a 1 meter dish antenna at 300 GHz is two kilometers (allowing maximum phase variation of  $22.5^\circ$ ). The impracticality of the method for testing electrically large antennas is evident.

**Table 2.1** Calculated far-field distances for 1–4 meter antennas between 1–1000 GHz.

Diameter [m]	Far-field distance as a function of frequency					
	1 GHz	10 GHz	100 GHz	300 GHz	650 GHz	1000 GHz
1	6.67 m	66.7 m	667 m	2.00 km	4.34 km	6.67 km
2	26.7 m	267 m	2.67 km	8.0 km	17.3 km	26.7 km
3	60.0 m	600 m	6.00 km	18.0 km	39.0 km	60.0 km
4	107 m	1.07 km	10.7 km	32.0 km	69.4 km	107 km

Conventional far-field techniques include the free-space and ground reflection methods [9]. However, the ground reflection range is not applicable at mm or submm wavelengths. In the free-space far-field range, the antennas are elevated high above ground to avoid main beam reflections from the surface between them. Very large high-gain radiotelescopes can sometimes use a radio star or a satellite beacon as the transmitter. If the far-field distance allows, the free-space range can be located indoors in an anechoic chamber. One of the antennas is rotated around the azimuth and elevation angles and the received power is recorded. The directional pattern is readily obtained from the recorded data after normalisation.

### 2.4 Near-field scanning measurements

Near-field scanning techniques are based on sampling the radiating near-field of the AUT according to a certain geometry. The sampling interval must be smaller than or equal to  $\lambda/2$  in order to satisfy the Nyquist sampling criterion [10]. Knowledge of the probe location should also be better than  $\lambda/100$ . The most common sampling geometry is planar, but cylindrical and spherical scanning can also be used (see Figure 2.3). The mathematical near-field to far-field transformation done on a computer is different for each scanning geometry. The probe

antenna used in the scanning should have a wide directional pattern, and be small-sized so it does not disturb the measured field through multiple reflections.

The true angular pattern of the AUT is distorted by the convolution between the AUT and the probe angular patterns. Accurate results require that the probe pattern must be deconvolved from the AUT by dividing the complex AUT angular spectrum by the complex probe spectrum [10]. The angular spectrum is defined as the two-dimensional Fourier transform of the phase front, and convolution of two functions as the product of the Fourier transforms of the two functions. Deconvolution is the inverse process. Probe correction formulas in matrix form suitable for computer application can be found in [10] and [11].

The measurement time for large antennas can be several hours or even days, so high electrical and mechanical stability are required from the instrumentation. The frequency switching speed of a modern vector network analyser is so fast that the near-field pattern can be measured at several frequencies at the same time with continuous probe movement. In order to be able to calculate all the common antenna parameters, the measurements must be done at two orthogonal polarisations [10]. The near-field scanner and the AUT should be located inside an anechoic chamber to avoid reflections.

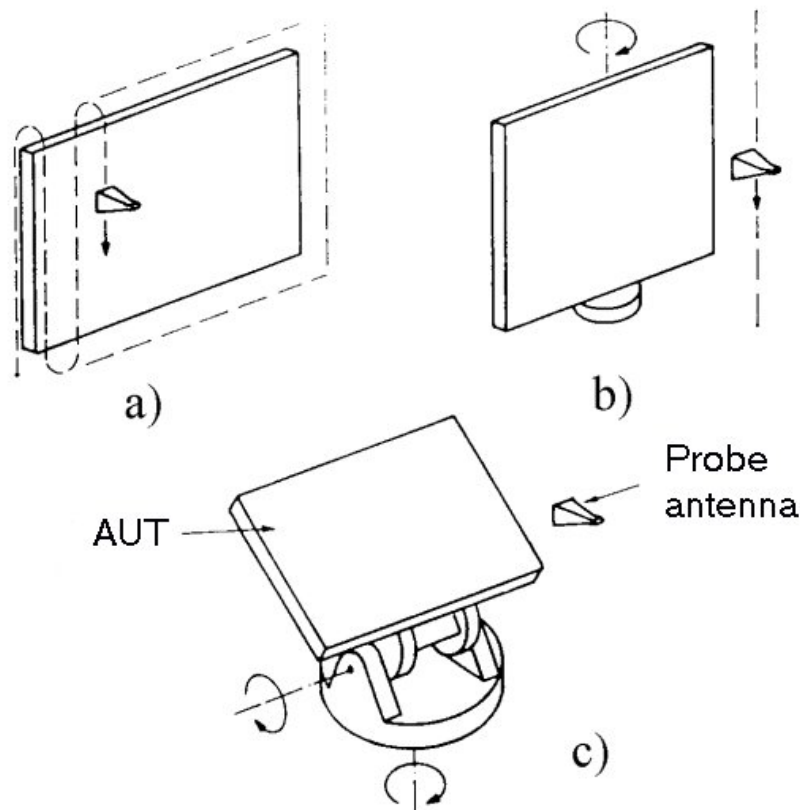


Figure 2.3 Near-field scanning geometries : a) planar, b) cylindrical, c) spherical [8].

#### 2.4.1 Planar near-field measurements

Planar near-field scanning requires great accuracy from the probe positioning system, but the mathematics involved are relatively simple. Planar scanning is especially suitable for antennas that are designed to radiate in one direction only, e.g., dish and horn antennas. Far sidelobes and backlobes can not be measured without repositioning. In the typical planar scanning

geometry shown in Figure 2.3 a) the AUT remains stationary and the probe is moved across the scanning plane in front of the AUT. Fragile antenna systems and spacecrafts are well suited for planar scanning because heavy positioners are not needed. The far-field pattern of the AUT can be directly calculated by applying the Fast Fourier Transform (FFT) to the measured near-field data. The possibility to use FFT reduces the computation time by at least an order of magnitude compared to the basic Fourier transforming. The scanning area must be at least a couple of wavelengths larger than the AUT aperture in order to avoid far-field pattern errors due to beam truncation [10,11].

The highest operational frequency of the planar near-field scanning system is determined by the wanted measurement accuracy. The mechanical properties of the scanner are the most important, especially the planarity of the scan plane and the positioning accuracy of the probe antenna. The sampling interval needs to be smaller than  $\lambda/2$ , and the amount of sample data can raise to millions of points for electrically large antennas making the mathematical processing time and memory consuming.

The flexing of measurement cables during scanning causes phase errors in the measurements. Several methods of bringing a stable phase reference to the receiver and measuring the phase error are discussed in [10]. The developed system by the author of this thesis for measuring and correction of these types of errors is presented in Chapter 5 and in [P1]. Error and uncertainty analysis for the planar scanning method can be found in [12].

The highest frequency reported planar near-field measurements have been done at 650 GHz for the Earth Observing System Microwave Limb Sounder (EOS MLS) satellite [6] and at 550 GHz for the Submillimeter Wave Astronomy Satellite (SWAS) [13] using a granite-based scanner. The EOS MLS antenna has a diameter of 1.6 m, and the size of the used scanner was  $2.4 \times 2.4 \text{ m}^2$ . The measured RMS planarity over the scan area was better than  $4 \text{ }\mu\text{m}$ . The size of the SWAS antenna is  $53 \times 68 \text{ cm}^2$ , and the size of the used scanner was  $90 \times 90 \text{ cm}^2$ . The measured RMS planarity of the scanner was better than  $5 \text{ }\mu\text{m}$ . In both experiments, the probe antenna was configured as the transmitter, and the spacecraft's own receivers were used.

## 2.4.2 Cylindrical and spherical near-field measurements

The mechanical instrumentation required for scanning on cylindrical and spherical geometries is much simpler than for planar scanning. These geometries make it possible to also measure antennas with multiple main lobes in different directions. However, this comes with a penalty: much more data points than in the planar geometry are required, and the mathematical near- to far-field transformation is substantially more complex [11]. In the typical cylindrical scanning geometry shown in Figure 2.3 b), the AUT is rotated in the azimuth plane and the probe antenna is moved vertically. The most common spherical scanning geometry (Figure 2.3 c) is based on rotation of the AUT in both azimuth and elevation planes while the probe antenna remains stationary. The probe corrected near- to far-field transformation formulas for both cylindrical and spherical scanning methods can be found in [11].

The near- to far-field transformation in the cylindrical geometry may use the FFT algorithm, but since the number of data points for a similarly sized antenna is approximately doubled compared to the planar case this leads to twice the computational time per frequency. The situation is worse with the spherical geometry where efficient FFT algorithms are not available, leading to longer processing time for a single far-field cut than for the planar and cylindrical geometries [11]. Also the number of data points for the spherical geometry is

considerably larger than for the cylindrical case. The memory and processor power limitations of even the most modern computers are reached easily with large cubically expanding matrices.

The highest operating frequency for cylindrical and spherical near-field scanning is limited by the tolerable error limits like in the planar case. The planar scanning method is more suitable for millimetre and submillimetre wave antenna measurements due to the smaller amount of required data points.

## 2.5 Compact ranges

The compact antenna test range can be used to simulate far-field conditions inside an indoor chamber with controlled temperature and atmosphere. This is especially useful at millimetre and submillimetre wavelengths where the far-field distance grows easily to kilometers (Table 2.1). CATRs require low transmitted power levels due to the relatively small distance between the antennas. Military and commercial satellite manufacturers also benefit from the increased security of the indoor chambers compared to outdoor far-field ranges. The history and development of the CATR concept is presented in [14].

In a CATR, a collimator is used to transform an incoming spherical wavefront into a plane wave. The volume where the plane wave is optimised is called the quiet-zone of the CATR. The collimator can be a reflector, a lens, or a hologram. The quiet-zone size must be large enough to surround the AUT also under rotation.

A CATR is also very useful for radar cross section (RCS) measurements of aircraft, tank, and warship scale models. The reflector, lens, and (phase) hologram CATRs collimate the reflected radiation from the target back to the range feed horn. High frequency operation is desirable, because the size of the scale model is inversely proportional to the frequency [9]. For example, if the RCS properties of a 20 meter long fighter plane at 10 GHz (common military radar frequency) are to be found out, a scale model length of 2 m at 100 GHz and 67 cm at 300 GHz is required. Simple scaling of size provides accurate results for metallic objects with high conductivity, but if lossy dielectrics (cockpit windows, radomes, sea water, etc.) are present their conductivity must be scaled with frequency.

### 2.5.1 Reflector CATRs

The reflector CATR is commonly used to test large-sized antennas at microwave and millimetre wave frequencies. The range uses one or more shaped reflectors to create a plane wave inside the quiet-zone volume. Cylindrical or offset paraboloidal reflectors can be used, although the latter is by far the most common type. The offset reflector CATRs can be divided into three types based on the number of reflectors: single, dual, and tri-reflector CATRs.

The upper frequency limit of the CATR operation is set by the surface accuracy of the reflector, which should be better than  $\lambda/50$  [14]. The low frequency limit is set by the diffraction from the reflector edges that causes fluctuations in the quiet-zone field. Effects related to edge diffraction can be minimised by decreasing the edge illumination and by shaping the edges. Common edge shaping techniques in use are: serrated edge, rolled edge, and resistive tapering [9]. Serrated edge reflector is the most common type in CATRs, and it

is illustrated in Figure 2.4. The effect of the serrations is that they scatter the diffracted signal in other directions from the quiet-zone. Area needed for effective serrations may be substantial, even 25% of the reflector area (depending on the wanted lowest operation frequency), and it reduces the obtainable quiet-zone/reflector size ratio [9]. Rolled edge directs the scattered signals towards the anechoic chamber walls, where they are absorbed. Resistive tapering should absorb the excess edge illumination.

The CATR quiet-zone area and thus the maximum diameter of the AUT are determined by the reflector size and the range topology. The ratio between the quiet-zone and reflector sizes is set by the maximum allowable edge illumination, and it is different for single, dual and tri-reflector CATRs. For a typical single offset reflector CATR, the quiet-zone size is only about 30% of the reflector size [14,15]. The dual and tri-reflector configurations can have quiet-zone sizes of over 75% of the main reflector size [3,16].

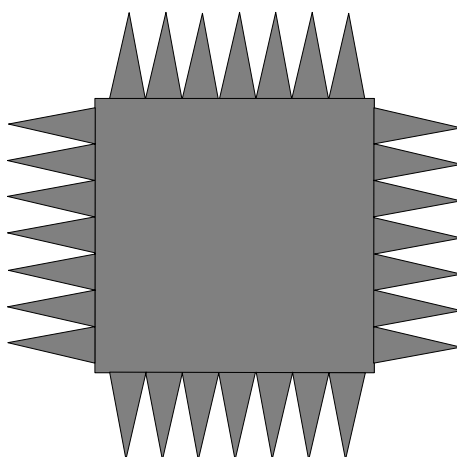


Figure 2.4 Serrated reflector.

In the single reflector CATR, an offset paraboloidal reflector is commonly used [15]. The edge illumination at the reflector edges must be below  $-10$  dB in order to prevent the diffracted fields from deteriorating the quiet-zone field. The required strong amplitude taper across the reflector aperture limits the usable area of the reflector and the quiet-zone size to about 30% of the total area. For measurements of large antennas, a very large and expensive reflector is needed. A single reflector can generate quiet-zone fields with amplitude ripple below  $\pm 0.5$  dB and phase ripple below  $\pm 5^\circ$ . The problem with the single offset reflector geometry is the relatively high level of cross-polarisation which is  $-30$  dB [14]. A typical single offset reflector CATR is shown in Figure 2.5. The reflector can be made from a single piece or from joined panels.

By using two reflectors, quiet-zone sizes of 75% compared to the main reflector size can be achieved [3]. The drawback is that two reflectors of nearly the same size are required. The reflectors can be cylindrical or shaped. Cylindrical reflectors are easier to manufacture, but the cross-polarisation level remains quite high [14]. Shaped reflectors are more common and better results have been achieved with them. The dual reflector geometry can be used to overcome the cross-polarisation limitations of single offset reflectors, and cross-polarisation levels below  $-40$  dB can be achieved by canceling the cross-polar components [3,14].

The layout of the dual reflector CATR in use at Astrium GmbH (Ottobrunn, Germany) is shown in Figure 2.6 [3]. The size of the main reflector is  $7.5 \times 6.0 \text{ m}^2$  and the subreflector is  $5.6 \times 5.3 \text{ m}^2$ . Volume of the quiet-zone has been measured to be  $5.5 \times 5.0 \times 6.0 \text{ m}^3$  at 200 GHz. The RMS mechanical accuracy of the reflector system is about  $22 \text{ } \mu\text{m}$  ( $\lambda/70$  at 200 GHz), resulting in a phase error of about  $5^\circ$  at 200 GHz. The same range has been used for testing of an electrically large reflector antenna with a diameter of 1.5 m at 503 GHz [4]. The mechanical accuracy of the reflectors was not good enough, so modeling and computer compensation of the inaccuracies was used in the tests.

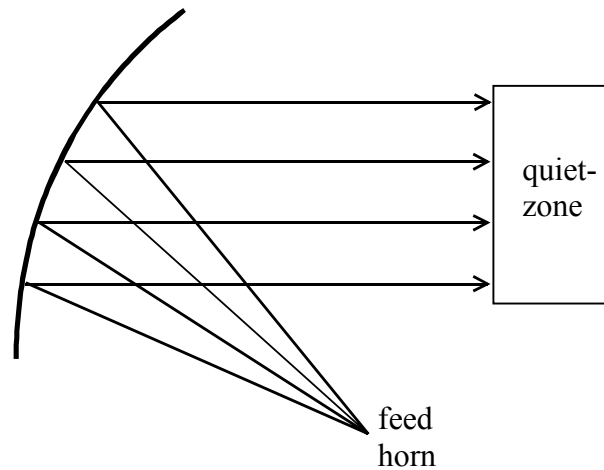


Figure 2.5 The layout of a single offset reflector CATR.

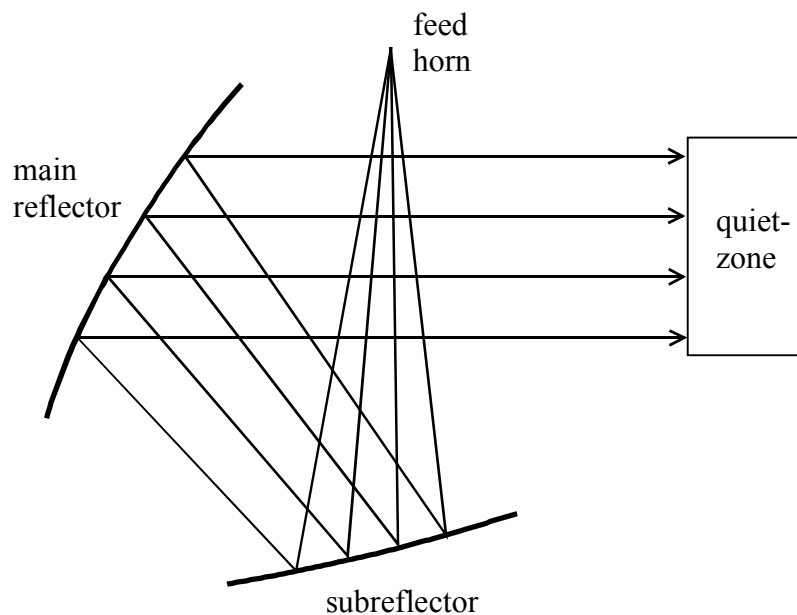


Figure 2.6 The layout of a dual reflector CATR.

A tri-reflector CATR uses a dual-reflector feed system (DRFS) to illuminate a paraboloidal or spherical main reflector [16–18]. The sizes of the two shaped subreflectors are considerably smaller than the main reflector. The DRFS has been used to enlarge the quiet-zone of an

existing single reflector CATR by a factor of 2.2 [17]. A tri-reflector CATR with a spherical main reflector has been proposed by the Queen Mary and Westfield College (University of London, UK) [16,18], but problems with the alignment and diffraction due to the chosen geometry have prevented a practical realisation so far. The spherical surface would be very desirable for large reflectors because well-developed machining methods from optics could be used.

### 2.5.2 Lens CATRs

A dielectric lens can be used as the collimating element in CATRs instead of reflectors [19–22]. The lens transforms a spherical wavefront radiated by a feed horn into a planar wavefront at the secondary surface of the lens. The lens material should be homogeneous and have low transmission losses. The thickness of the required lens is determined by the dielectric constant of the material. A large dielectric constant makes it possible to manufacture thin and compact lenses, but at the same time the surface reflections and cross-polarisation produced by the lens are increased [19]. Good lens materials with a low dielectric constant include Rexolite, teflon, polyethylene, and various foam materials such as polystyrene [19].

One or both sides of the lens can be shaped, but according to [19] the thinnest lens is produced by having a flat secondary surface. The edges of the lens should be shaped similarly as those of reflectors in order to reduce the effect of edge diffraction. A polyethylene lens with a diameter of 30 cm used in a CATR at 110 GHz is shown in Figure 2.7 [22]. A thin copper foil with etched cosine-shaped serration patterns is placed behind the lens in order to reduce edge diffraction. The quiet-zone amplitude ripple for the lens CATR at 110 GHz was measured to be  $\pm 1$  dB across a diameter of 20 cm.

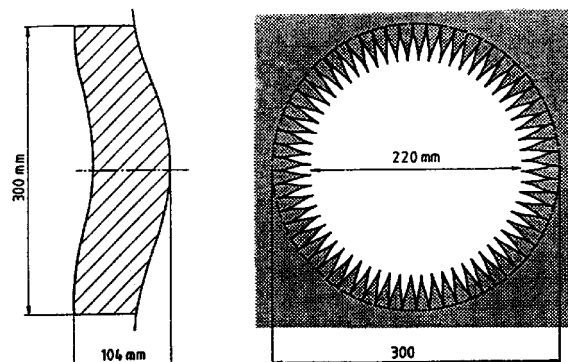


Figure 2.7 A lens manufactured from polyethylene ( $\epsilon_r = 2.32$ ) for use in a CATR [22].

The required surface accuracy of the lens depends on the dielectric constant  $\epsilon_r$  of the material. For a lens the phase error due to its surface inaccuracy is weighted by a factor of  $(\sqrt{\epsilon_r} - 1) / \sqrt{2}$  compared to a reflector [22]. The smaller the  $\epsilon_r$ , the thicker the lens and thus higher dielectric losses. Manufacturing large lenses from foam materials is difficult because the foam is not homogeneous enough for submillimetre applications.

The use of lenses in CATRs has been very limited because the reflectors perform so well at microwave frequencies and are easy to manufacture. However, as was already discussed in Section 2.5.1, the manufacturing of millimetre and submillimetre wave reflectors with

extreme surface accuracies is very expensive. Lenses are suitable for measurements of small antennas at millimetre wavelengths, but manufacturing of large lenses is problematic due to material difficulties. The hologram CATR discussed in the next section can overcome some of the manufacturing and surface accuracy problems related to lenses and reflectors.

### 2.5.3 Hologram CATR

The most recent alternative for the CATR collimator is the binary amplitude hologram [5]. It is especially suitable for millimetre and submillimetre wave operation. A hologram is an interference pattern of two wavefronts on a certain plane. If the hologram is illuminated with one, then it will generate the other and propagate it into the designed direction. In the CATR application, the hologram is used to transform a spherical wavefront into a planar wavefront.

The hologram is designed to modulate either the amplitude or the phase of the transmitted field. Accordingly, the hologram is called an amplitude or a phase hologram. The latter is sometimes called a kinoform [5]. The holograms in use at the HUT Radio Laboratory are computer-generated amplitude holograms and have been designed to propagate the plane wave into a direction of  $33^\circ$  relative to the hologram normal [P2–P4,O1,5,23–28]. The direction is chosen so that the unwanted diffraction modes propagating along the normal do not disturb the quiet-zone fields. The binary amplitude hologram pattern is designed and simulated with a computer using a combination of the FDTD (finite difference time domain) and PO (physical optics) methods. The hologram consists of several hundreds of curved slots that are tapered near the edges in order to reduce edge diffraction. The design procedure is described e.g. in [23]. The layout of the hologram CATR and a typical hologram pattern are shown in Figure 2.8.

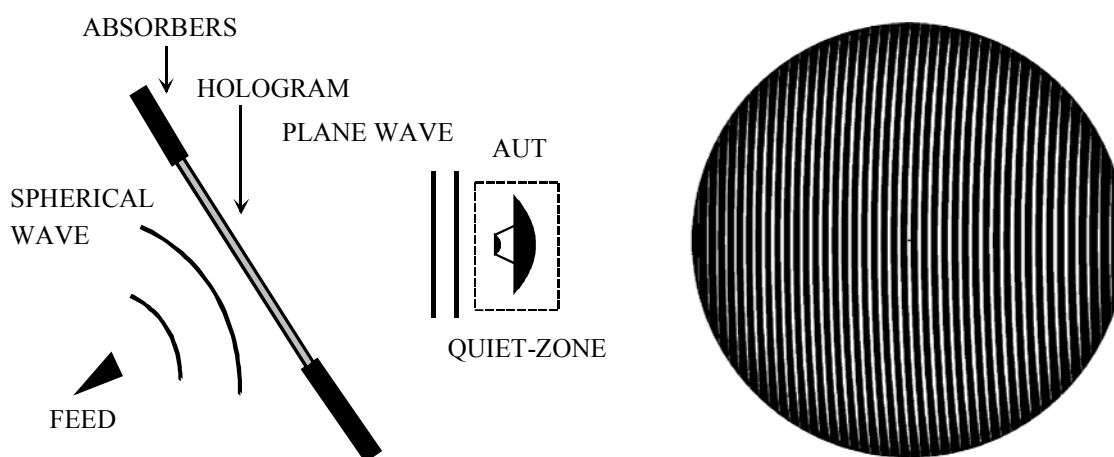


Figure 2.8 Layout of the CATR based on a hologram and an example of a typical computer-generated amplitude hologram pattern [23].

The transmission-type amplitude hologram used in CATRs can be manufactured with good accuracy as a slot pattern on a metallised dielectric substrate. Standard printed circuit board (PCB) exposure and etching methods or more advanced laser processing can be used to generate the wanted patterns. A large-sized hologram can be made from several pieces through joining by tape or by soldering [27]. However, the joints introduce disturbances in the

quiet-zone field, and should be avoided if possible. Simulation results for the quiet-zone field disturbances caused by joints at 300 GHz and at 500 GHz can be found in [O1] and [28].

The surface accuracy demand for a transmission-type hologram used in CATRs is less stringent than for the CATR reflectors [28]. The hologram is also tensioned in a frame, which ensures excellent planarity of the surface. A hologram CATR has been used for testing of the Swedish Odin-spacecraft at 119 GHz [27], and a planar link antenna at 40 GHz [25,26]. Submillimetre wave operation has also been demonstrated [P2]. The hologram CATR is being applied for measuring a large submillimetre telescope in the 1.5 meter class at 322 GHz and for a demonstrator at 650 GHz [P3].

A drawback of the hologram CATR method is the strong dependence on frequency and polarisation due to its diffractive nature [23]. The bandwidth of the hologram CATR is about  $\pm 5\text{...}10\%$  depending on the required quiet-zone quality. Due to the pattern structure composed of curved slots, operation only on a single linear polarisation is possible. A separate hologram must be designed for vertical and horizontal polarisations. The cross-polarisation level of  $-20$  dB produced by the hologram [P4] is also relatively strong compared to the  $-30$  dB in single reflector CATRs [14]. Further, the coupling loss of a typical amplitude hologram can reach 20 dB which limits its suitability for RCS applications. A better alternative for RCS measurements is to use a phase hologram [O34, O37].

The ratio between the quiet-zone and hologram areas depends on the size of the quiet-zone and the frequency. The tapering area required near the slot edges remains more or less the same for small and large holograms. For larger holograms, a better quiet-zone/hologram size ratio is achieved. For example, at 119 GHz, the quiet-zone of a 55 cm hologram was 43% [23] and the quiet-zone of a  $2.4 \times 2.0 \text{ m}^2$  was 70% of the smallest hologram dimension [27].

## 2.6 Other methods

Other antenna measurement methods than the common far-field, near-field, and CATR methods have also been developed. Usually these are cost-driven extensions or modifications of the typical methods. An interesting extension to the near-field method is the possibility to do phaseless near-field measurements using phase retrieval techniques on cylindrical or planar surface geometries [29–34]. The required amplitude-only measurements can be done accurately even at high frequencies and with relatively inexpensive equipment. The phase retrieval method can also tolerate higher probe position errors than conventional planar near-field measurement [31]. The algorithm requires measurement of the near-field amplitude on two planes which are separated by a few wavelengths. An initial guess, based on the geometry of the AUT, for the amplitude and phase in the aperture plane of the AUT are required. The phase retrieval algorithm uses Fourier iteration for calculating the complex near-field distribution on the AUT aperture plane and on the two measurement planes. After the iteration procedure, the far-field characteristics of the antenna can be calculated by a standard NF-to-FF transformation from the obtained complex near-field distribution. In [30], good correlation between phaseless and conventional planar near-field measurements for an array antenna at 9.3 GHz were obtained.

The semi-compact antenna test range (SCATR) [35,36] and the single-plane collimating range (SPCR) [37] are hybrids between the CATR and near-field methods. The SCATR uses a line source probe consisting of a pillbox antenna to provide a quasi-cylindrical wavefront in the

test zone. The pillbox antenna performs instantaneous integration of the field in one dimension, reducing the typically two-dimensional near-field data acquisition and processing problem into a one-dimensional one. The AUT is rotated in the azimuth direction and the complex near-field is measured, after which cylindrical wavefront expansion theory is used to calculate the far-field. A SCATR facility can also use the phaseless near-field algorithms for predicting the far-field of the AUT, and is potentially of low cost and suitable for high frequencies [35].

The SPCR range presented in [37] uses a parabolic cylinder. RCS measurement results for two targets in the range are also shown in the reference. The inherent field disturbances and RCS measurement discrepancies arising from the cylindrical illumination instead of planar have been shown to be correctable using a relatively simple algorithm denoted as the 'reference bar method'. Very good correlation between the measurements done with a dual-reflector CATR and the SPCR using correction have been obtained [37].

Holographic methods have also been used for analysing, measuring, and optimising high gain antennas at millimetre and submillimetre wavelengths [38,39]. In [38], the far-field amplitude and phase patterns of a 14 meter radio telescope were measured by using a satellite beacon at 38 GHz as the transmitter. The amplitude and phase in the aperture plane can then, according to the reciprocity theorem, be calculated by applying two-dimensional Fourier transform. The aperture phase distribution was used to optimise the panel alignment of the telescope.

Gabor holography can be used to determine the far-field pattern from near-field measurements [39]. The method is based on sampling the near-field intensity or field magnitude, and forming the hologram i.e. the interference pattern between the AUT and the small reference antenna used for sampling. The phase information of the near-field can be obtained from the generated hologram by calculating out the known reference antenna pattern. The calculated far-field pattern produced by the holographic method is shown to be more sensitive to errors in the sample locations along the scan axis than the conventional near-field method [39]. On the other hand, holography is relatively insensitive to planarity errors which are the most significant source of error in conventional near-field measurements, and also the most difficult to reduce.

Finally, refocusing of certain types of antennas can be used to measure their far-field patterns [40]. This method can be used when long enough far-field ranges or CATRs are not available. Suitable antennas include the paraboloidal and lens antennas that can be focused by axial movement of the feed, linear arrays that can be physically bent along a circular arc of radius corresponding to the test distance, and electronically phased arrays focusable through phasing of individual elements [40]. In the far-field refocusing method, radiation pattern measurements are done with the antenna focused at the test distance inside its radiating near-field region. The antenna is then refocused at infinity, and the measured patterns at the test distance are assumed to represent the true far-field patterns of the AUT focused at infinity but with a certain error range. The method usually predicts accurately the direction of the main beam, but strong perturbations in the sidelobe structure occur when the test distance is too small [40].

The described far-field refocusing method has been proposed for large spaceborne radiotelescope arrays, specifically designed for VLBI (Very Large Baseline Interferometry) imaging [41]. Some of these arrays would be so large that some objects inside our solar system would be inside the near-field of the arrays, making it impossible to use common

imaging methods. According to [41], it is possible to image radio sources inside the near-field distance of the antenna array, if the array itself is in the far-field of the radio source. Refocusing of a VLBI array can be done electronically by changing the phasing between the individual telescopes, or by modified computer processing of the obtained data from the telescopes. The cost of applying these techniques to existing telescopes would be minimal.

### 3 Millimetre and submm wave vector network analyser

#### 3.1 Description of operation

A network analyser is a device which is capable of measuring the reflection and transmission coefficients (S-parameters) from the ports of a device connected between the analysers terminals. A network analyser usually consists of two parts: the analyser part and the test unit. The test unit contains the RF transmitter and receiver modules, and the analyser part processes and displays the measured data. Network analysers are further divided into scalar and vector network analysers. Vector analysers can measure both the amplitude and the phase, but scalar analysers are only capable of amplitude measurements.

Vector network analysers based on the heterodyne principle downconvert the received signal to a low IF frequency and compare its phase with a reference signal [42]. The reference signal can be obtained from the transmitted signal with a directional coupler, or it can be derived from a reference oscillator common to the transmitter and the receiver. The vector network analyser HP8510 from Agilent Technologies, Inc. uses the former principle, and the MVNA-8-350 vector analyser from AB Millimètre uses the latter. The advantage of the common reference approach is that lossy mm-wave directional couplers are not needed for transmission measurements, and operation at submillimetre wavelengths is possible. However, a reflectivity measurement without a directional coupler is not possible.

All network analysers capable of operating at millimetre wavelengths and beyond use frequency multiplication in the transmitter and harmonic mixing in the receiver [42]. Extensions for the HP8510 analyser are available upto 110 GHz from Agilent Technologies and to even higher frequencies from other manufacturers. The operational frequency range of the MVNA-8-350 with transmitter and receiver extensions ESA-1 and ESA-2 extends from 8–800 GHz [43]. In this thesis work, the instrumentation development took place around the MVNA-8-350. A schematic diagram of the MVNA with extensions is shown in Figure 3.1.

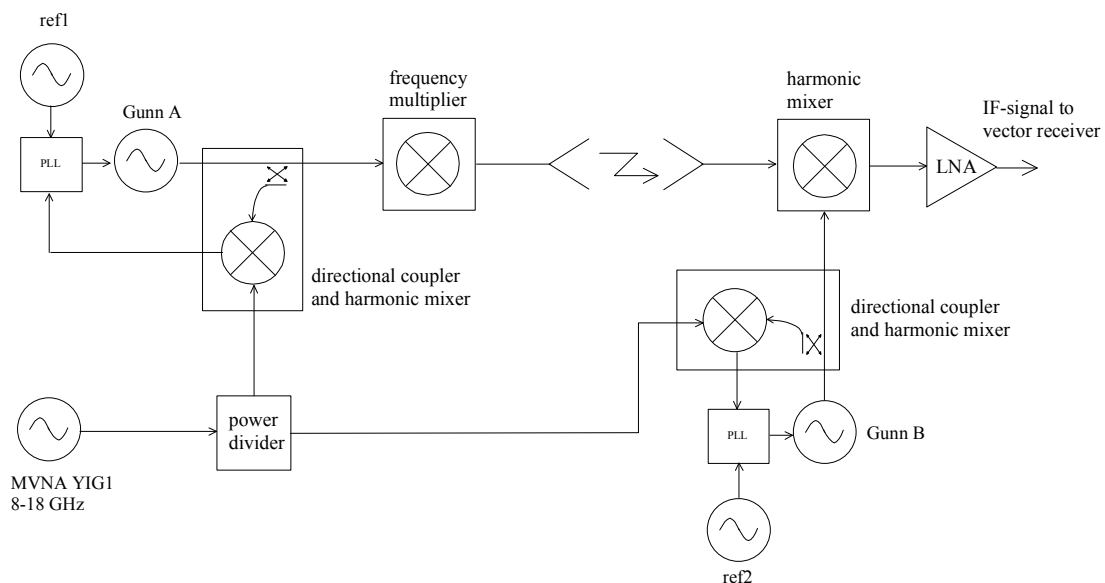


Figure 3.1 Schematic diagram of the MVNA-8-350 with extensions [43].

### 3.2 Source system

Many types of signal sources, including electron tube and solid-state oscillators, can be associated with the MVNA analyser. Electron tube oscillators such as the backward-wave oscillator (BWO), klystron, and traveling-wave tube (TWT) are interesting for many applications because they have high output powers. However, the BWO is the most suitable of these for submillimetre wavelengths due to its structure. Disadvantages of the electron tubes are the required stable high voltage source, relatively short lifetime, and bulky size. A solid-state oscillator usually has significantly lower output power, but it is small, lightweight, has small power consumption, and is much more reliable. Power combining can be used to increase the maximum output power from solid-state devices, but a limit is imposed by the lossy on-chip combining networks at high frequencies. Low loss power combining at high frequencies is possible by using quasi-optical devices such as wire grids and dielectric slabs, but with the disadvantage of the system being bulky in size.

The next section presents the standard MVNA extension ESA-1 which facilitates continuous coverage across the frequency band of 75–800 GHz. Design of a more powerful phase-locked BWO source and the achievable improvement in dynamic range when associated with the MVNA are presented in Chapter 4.

#### 3.2.1 ABmm ESA-1 transmitter

The ESA-1 transmitter is based on a phase-locked Gunn oscillator followed by a multiharmonic frequency multiplier. The center frequency of the Gunn oscillator can be tuned mechanically between 75–115.5 GHz, and electronically about  $\pm 250$  MHz by adjusting the bias-voltage. A waveguide high-pass filter is used after the frequency multiplier to select the wanted harmonic to the output.

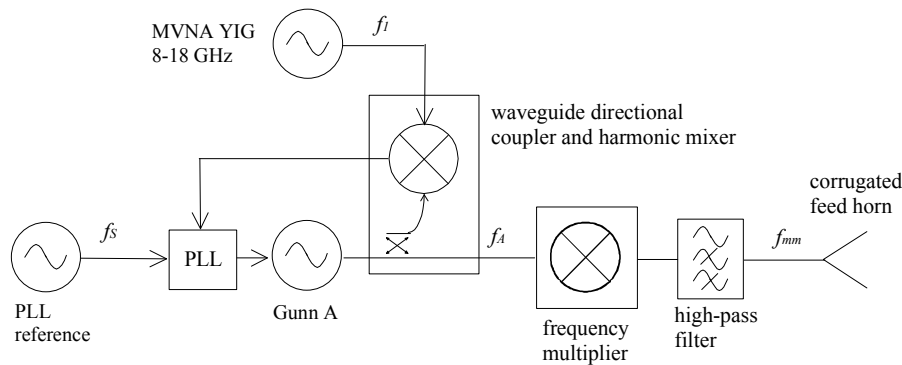


Figure 3.2 Schematic diagram of the ABmm ESA-1 transmitter.

The output frequency from the phase-locked transmitter shown in Figure 3.2 is

$$f_{mm} = Mf_A = M(kf_1 - f_s), \quad (3.1)$$

where  $M$  is the multiplier harmonic number,  $k$  the harmonic number in the Gunn oscillator phase-lock loop downconverter,  $f_A$  the Gunn oscillator frequency,  $f_1$  the local oscillator frequency for the downconverter, and  $f_s$  the Gunn-PLL reference frequency. A photograph of the ESA-1 transmitter is in Figure 3.3.

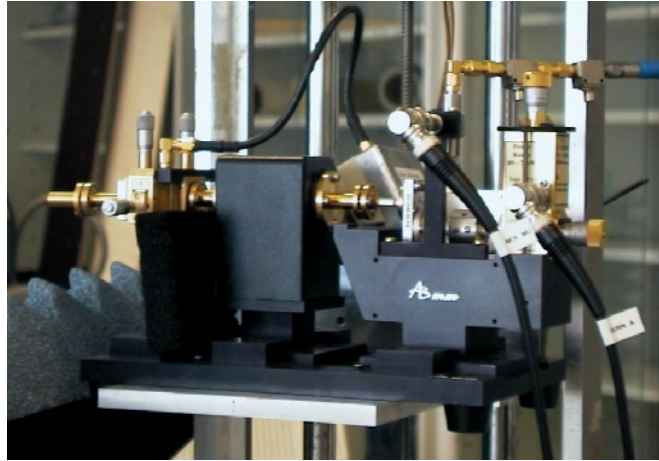


Figure 3.3 Photograph of the ABmm ESA-1 transmitter.

### 3.3 Receiver system

The MVNA can use a simple Schottky-diode harmonic mixer shown in Figure 3.4 as the receiver for the frequency range of 50–170 GHz. A set of receiver modules is needed to cover the full waveguide bands of 50–75 GHz (V-band), 75–110 GHz (W-band), and 110–170 GHz (D-band). The D-band mixer (HM-D) can be used to detect strong signals up to 300 GHz and beyond, but with high conversion loss due to a high harmonic number. The intermediate frequency (IF) signal for the vector receiver is

$$f_R = f_{mm} - Nf_2, \quad (3.2)$$

where  $f_{mm}$  is the received signal frequency,  $N$  the harmonic number in downconversion, and  $f_2$  the local oscillator frequency.

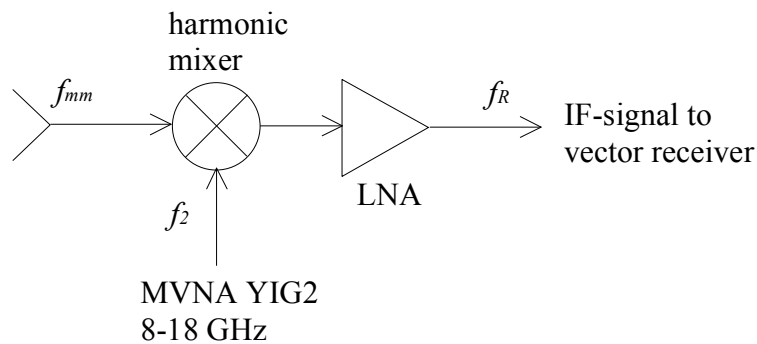


Figure 3.4 Receiver based on harmonic mixing (ABmm HM).

A better alternative for frequencies over 300 GHz is the ESA-2 receiver (see next section), which has about 40 dB lower conversion loss [44]. The dynamic range obtainable with different transmitter and receiver configurations is discussed in Section 3.4.

### 3.3.1 ABmm ESA-2 receiver

A sensitive submillimetre wave receiver must use as low a harmonic number as possible. The ABmm ESA-2 extension shown in Figure 3.5 is based on a sensitive Schottky-diode harmonic mixer, which accepts local oscillator signals between 75–115 GHz from a phase-locked Gunn oscillator. A fixed waveguide high-pass filter with a cutoff frequency of 260 GHz is used between the horn antenna and the harmonic mixer in order to prevent lower harmonics from saturating the receiver. The ESA-2 receiver is very similar in construction to the ESA-1 shown in Figure 3.3.

The intermediate frequency going into the vector receiver is

$$f_R = M(f_A - f_B) = M(kf_1 - f_s - kf_1 + f_0) = M(f_0 - f_s). \quad (3.3)$$

In equation (3.3),  $M$  is the Gunn oscillator frequency multiplication factor,  $k$  the harmonic number in both Gunn-PLLs,  $f_0$  the reference frequency of the receiver Gunn-PLL (fixed at  $f_0 = 50$  MHz in normal operation), and  $f_s$  the reference frequency of the transmitter Gunn-PLL.

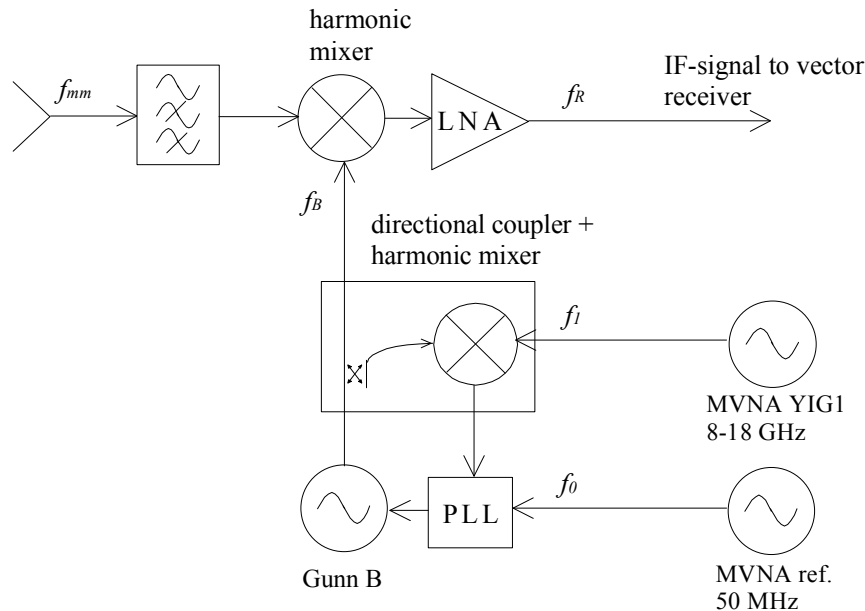


Figure 3.5 Schematic diagram of the ABmm ESA-2 receiver.

## 3.4 Dynamic range and measurement accuracy

The dynamic range or the signal-to-noise ratio of a vector network analyser is defined as the ratio between the maximum detected signal level and the receiver noise floor [43]. The available dynamic range when the transmitter and receiver are connected to each other (back-to-back configuration) can be calculated as

$$\frac{S}{N} (\text{dB}) = P_{mm} (\text{dBm}) - L_{nm} (\text{dB}) - P_n (\text{dBm}), \quad (3.4)$$

where  $P_{mm}$ (dBm) is the transmitted power,  $L_{hm}$ (dB) the conversion loss of the receiver, and  $P_n$ (dBm) the noise floor of the vector receiver [43]. The noise floor depends on the used sampling speed and averaging. In equation (3.4) the effect of phase noise of the local oscillator signal in case of a Gunn oscillator plus multipliers is taken into account in the receiver noise floor. Phase noise effects in conjunction with the phase-locked BWO source are discussed in Sections 4.4.4 and 4.5. It is shown that a phase-locked BWO instead of a frequency-multiplied Gunn oscillator does not raise the receiver noise floor. The vector receiver in use at the MilliLab, HUT Radio Laboratory has a fast receiver mode with 10 kHz sampling speed allowing 0.1 ms sample spacing. The lowest noise floor can be achieved by averaging. For example,  $P_n = -150$  dBm is obtained with averaging over 500 samples (20 frequency points/second), and  $P_n = -160$  dBm with averaging over 5000 samples (2 frequency points/second) [43].

The available dynamic ranges over frequency from the MVNA-8-350 analyser in use at MilliLab are shown in Figure 3.6. The curve labeled ‘MVNA’ corresponds to the standard configuration with the lightweight mm-wave heads, ‘MVNA+ESA-1’ to the usage of the ESA-1 transmitter and the HM-D mm-wave receiver, and the ‘MVNA+ESA-1+ESA-2’ to the usage of the ESA-1 transmitter and the ESA-2 receiver.

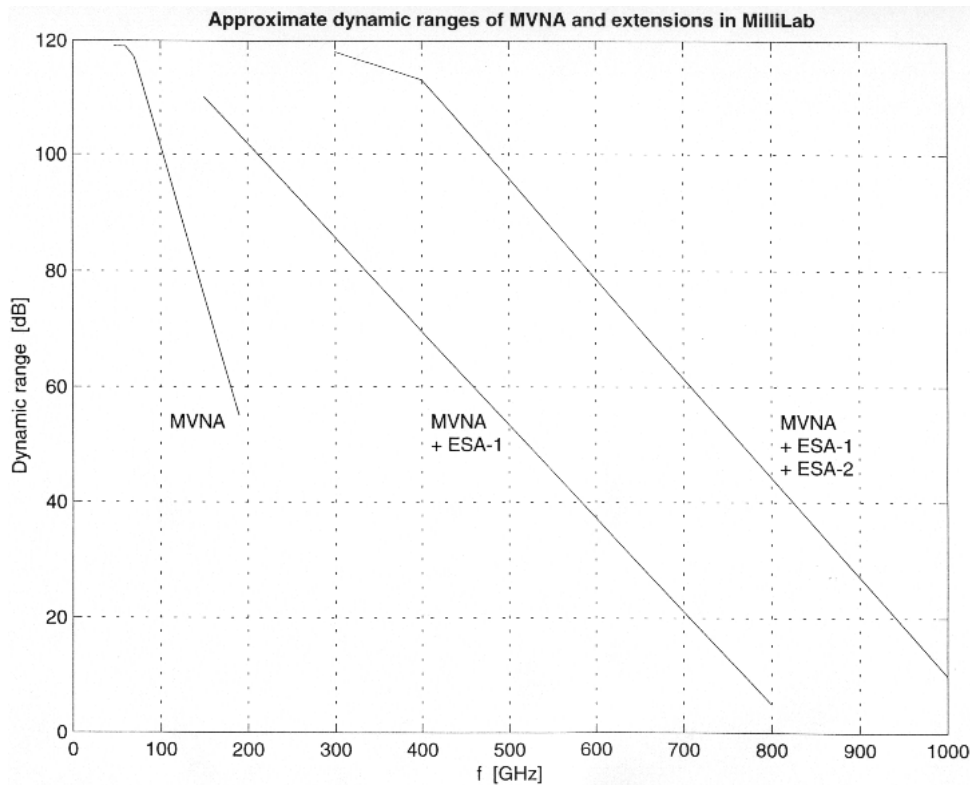


Figure 3.6 Approximate dynamic range of the standard MVNA and with extensions (maximum averaging over 10 000 points is used).

The amplitude and phase measurement uncertainties on the MVNA vector network analyser system depend heavily on the configuration of the transmitter and receiver and on the attenuation between them. The manufacturer states that the amplitude measurement uncertainty is smaller than 0.1 dB, and the phase measurement uncertainty smaller than  $1^\circ$  when indicated the dynamic range is over 40 dB.

Problems with the measurement uncertainty arise in certain measurement configurations, like planar near-field scanning. The receiver requires several cables to be connected to it, and the flexing of the phase reference cable introduces large variations to the measured phase. A correction system for the cable flexing effect was designed and constructed for the MVNA system. A detailed description including error analysis is given in Chapter 5 of this thesis and in [P1].

Studies have also been done on the short-term and long-term stability of the MVNA at 100 GHz [O16,O23]. The results indicate some problems with the frequency references and their distribution inside the analyser. Observed short-term effects include sudden phase jumps close to  $1^\circ$ . The long-term amplitude and phase drifts due to reference frequency drifting with time can prevent long measurement periods extending over several hours. A new reference clock generation board, based on a GPS-stabilized rubidium oscillator, for the MVNA analyser is being constructed at the time of writing. The new reference distribution system should improve the long-term accuracy and make possible accurate planar near-field scanning with a dense scanning grid.

## 4 Phase-locked oscillators

### 4.1 The importance of phase-locked sources for vector antenna measurements

Microwave and millimetre wave oscillators are usually phase-locked to a low-noise reference frequency or one of its harmonics. Several advantages can be obtained in the phase-locked mode compared to a free-running oscillator. The goal of a phase-locked loop (PLL) is to generate a stable, low-noise signal that does not depend on the application environment. The individual PLL components need to have low-noise characteristics in order to minimize the total phase noise of the locked oscillator.

Inside the PLL closed-loop bandwidth, the phase noise of the output signal follows that of the reference oscillator, and outside it follows the free-running oscillator [45]. The closed-loop bandwidth is determined by the loop transfer function, the phase detector coefficient, and the voltage controlled oscillator (VCO). A well-designed PLL combines the good qualities of both the reference and the VCO: the low close-carrier phase noise and good frequency stability of the reference, and the low noise floor of the VCO. Only a phase-locked transmitter will be able to maintain the required amplitude and phase accuracy in vector network analyser measurements over time.

A frequency synthesizer is a device that can generate output frequencies from a certain range and with a minimum step size (resolution) [45–48]. The VCO inside a good frequency synthesizer should be of a low phase noise type. The output frequency is selected by adjusting the digital dividers in the loop. In millimetre wave synthesizers, harmonic mixers are commonly used for downconversion of the output signal, and adjusting of the local oscillator frequency can be used to change the output frequency [45]. Fast-switching phase-locked frequency synthesizers are commonly used with VNAs in antenna measurements to facilitate measurements at multiple frequencies in a single antenna rotation.

### 4.2 Phase noise characteristics of oscillators and PLL systems

Phase noise is one of the most important parameters for an oscillator. Other important parameters include the output power, frequency tuning range, tuning step, and power consumption. All the power of an ideal, noiseless signal is concentrated on a single spectral line in the frequency domain. The ideal signal in the time domain is

$$f(t) = A \sin(2\pi f_c t), \quad (4.1)$$

where  $A$  is the amplitude and  $f_c$  the frequency of the signal [47]. A real signal with amplitude and phase noises has the form of

$$f_n(t) = A[1 + n_1(t)] \sin[2\pi f_c t + \phi_n(t)], \quad (4.2)$$

where  $n_1(t)$  denotes the amplitude noise and  $\phi_n(t)$  the phase noise [47].

The noise can be thought to originate when the signal is modulated with some disturbances. The disturbances can be separated to amplitude modulation (AM) and frequency modulation (FM) parts. The AM part is usually negligible compared to the FM part. The frequency modulation can be understood also as phase modulation (PM) causing the phase noise of the signal. Amplitude modulation can increase the phase noise through AM-PM conversion. The involved mathematics are presented in [47].

The total phase noise of an oscillator can be divided into long-term and short-term phase noises. The long-term phase noise has a slowly changing nature, and is mainly caused by changes in the Q-value of the resonator, aging, temperature, mechanical construction, pressure, gravity, and the stability of the power supply [47]. The short-term phase noise has deterministic and random parts. The deterministic phase noise can be caused by upconversion of the 50 Hz mains frequency or by mechanical shocks to the device, and it is seen as discrete spectral lines around the carrier frequency. The random phase noise has a wide symmetrical spectrum around the carrier. Its level is strongest near the carrier and it drops quickly when moving away from the carrier.

The phase noise performance of an oscillator can be specified in many ways. The most common way is to specify the single sideband (SSB) phase noise  $L_{SSB}(f_m)$  at a certain separation  $f_m$  from the carrier (see Figure 4.1 below). The SSB phase noise is calculated as the ratio between the phase noise power measured within a 1 Hz bandwidth and the carrier power, and its unit is dBc/Hz.

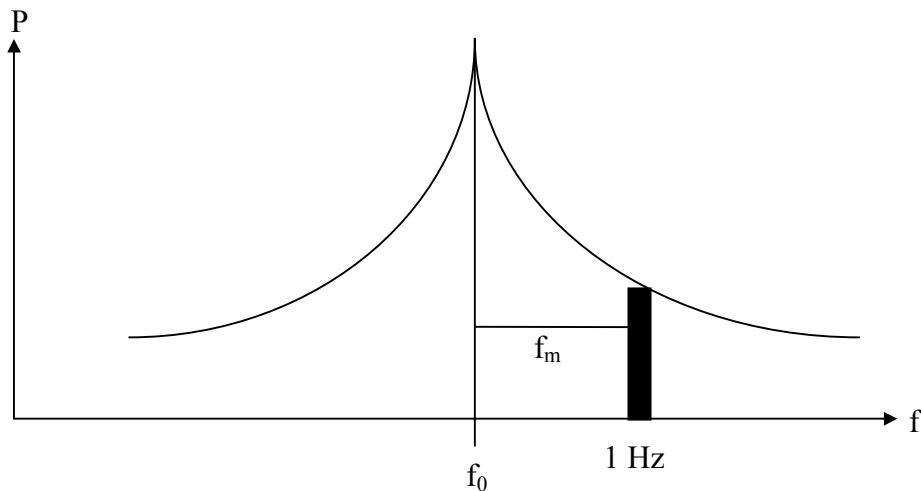


Figure 4.1 The definition of the SSB phase noise  $L_{SSB}(f_m)$  measured within a 1 Hz bandwidth [47].

Another commonly used method to specify the phase noise performance is the integrated phase noise [47]. The integrated single sideband phase noise across a frequency band of  $B$  is measured, and given as the relative power compared to the carrier power in units of dBc. The integrated phase noise is easier to measure than the SSB phase noise, but it does not give detailed information about the oscillator's spectral performance.

Sometimes it is useful to describe the frequency stability of an oscillator in the time domain. The Allan-variance characterises the fractional frequency deviations of the oscillator over time, and it is calculated by averaging the differences between consecutive sample pairs [46].

In addition to the phase noise, there exist also spurious and harmonically related components in the oscillator output spectrum. Spurious components are seen as discrete spectral lines, and include various subharmonic mixing results produced by nonlinear components in the circuit. Harmonically related components are integer multiples of the carrier frequency. The spurious and harmonic components are specified relative to the carrier power in dBc [47].

The phase noise generated in a PLL system can be modeled as a function of the individual component noises [49]. Millimetre and submillimetre wave signal sources are commonly based on frequency multiplication with harmonic generators. In the ideal case of a noiseless multiplier, multiplication by  $N$  increases the phase noise of the resulting signal as multiplied by  $N^2$ . A practical guide into minimizing the total phase noise of a PLL system is given in [46].

### 4.3 Phase-locked loop fundamentals

#### 4.3.1 Loop transfer functions

The simplest PLL topology is the phase follower shown in Figure 4.2. The linearised model consists of three components: the phase detector (PD), loop filter (LPF), and voltage controlled oscillator (VCO) [45]. The phase detector compares the phases of its input signal and the VCO, and outputs a DC voltage proportional to their difference. The output voltage is integrated and filtered in the loop filter, after which it is coupled to the VCO. The VCO output frequency changes so that its phase matches that of the reference signal to the PD. Phase-locked loop synthesizers commonly use a divide-by- $N$  divider in the feedback line from the VCO, resulting in an output frequency of  $N$  times the reference frequency. A second divider in the reference path can be used to adjust the step size of the synthesizer [46].

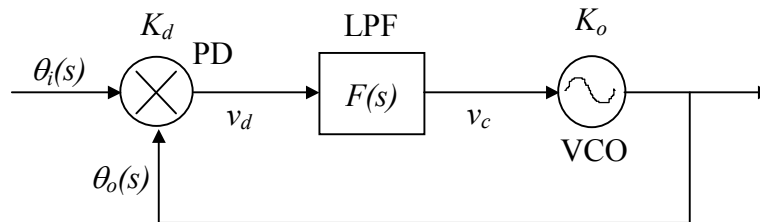


Figure 4.2 Schematic model of a linearised phase-locked loop (phase follower) [45].

The symbols used in Figure 4.2 are defined as:

- $K_d$  = phase detector gain [V/rad],
- $K_o$  = VCO gain [rad/sV],
- $v_d$  = output voltage from the phase detector [V],
- $v_c$  = VCO control voltage [V],
- $\theta_i(s)$  = phase of the input (reference) signal [rad],
- $\theta_o(s)$  = phase of the VCO output signal [rad],
- $F(s)$  = loop filter transfer function.

The closed loop phase transfer function of the model in Figure 4.2 can be derived to be [45]

$$H_{\theta}(s) = \frac{\theta_o(s)}{\theta_i(s)} = \frac{K_0 K_d F(s)}{s + K_0 K_d F(s)}. \quad (4.3)$$

Accordingly, the closed loop phase error transfer function can be derived to be [45]

$$H_{\phi}(s) = \frac{\theta_i(s) - \theta_o(s)}{\theta_i(s)} = \frac{\theta_e(s)}{\theta_i(s)} = \frac{s}{s + K_0 K_d F(s)} = 1 - H_{\theta}(s). \quad (4.4)$$

The dynamic response of the PLL is mainly determined by the loop filter transfer function  $F(s)$ . The number of integrators in the PLL is called the order of the loop. PLLs are always at least of the first order because the VCO itself performs integration of its control voltage [45]. Practical PLL realisations are mostly of the 2<sup>nd</sup> order because of its good qualities and simple construction. The commonly used loop filters in 2<sup>nd</sup> order PLL constructions are the passive and active lag-lead filters shown in Figure 4.3.

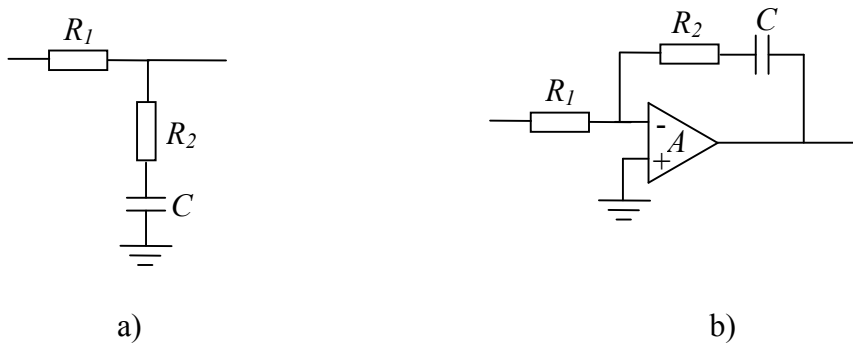


Figure 4.3 a) Passive and b) active lag-lead loop filter.

Let's introduce briefly the design equations for the 2<sup>nd</sup> order PLL using an active loop filter, because the phase-locked backward-wave oscillator (BWO) presented in Section 4.4 and in [P5] is of this type. The design equations for the passive loop filter can be found, e.g., in [45]. The loop filter transfer function of the active lag-lead filter, assuming infinite DC gain  $A$ , is [45]

$$F_a(s) = -\frac{s\tau_{2a} + 1}{s\tau_{1a}}, \quad (4.5)$$

where the time constants are defined as

$$\tau_{1a} = R_1 C, \text{ and} \quad (4.6)$$

$$\tau_{2a} = R_2 C. \quad (4.7)$$

Introducing (4.5)–(4.7) to (4.3), the closed loop phase transfer function can be written in the so-called servo-technical form as

$$H_{\theta,a}(s) = \frac{2\xi_a \omega_{n,a} \cdot s + \omega_{n,a}^2}{s^2 + 2\xi_a \omega_{n,a} \cdot s + \omega_{n,a}^2}. \quad (4.8)$$

In (4.8), the loop natural angular frequency  $\omega_{n,a}$  is defined as

$$\omega_{n,a} = \sqrt{\frac{K_0 K_d}{\tau_{1a}}}, \quad (4.9)$$

and the damping factor  $\xi_a$  as

$$\xi_a = \frac{\tau_{2a} \omega_{n,a}}{2}. \quad (4.10)$$

The closed loop phase transfer function (4.3) is of the low-pass type, and the phase error transfer function (4.4) of the high-pass type. It is evident that the PLL will attenuate phase variations of its noisy input signal (reference or the VCO) outside the closed loop bandwidth. Two typical PLL applications are described below, in which either the reference or the VCO is assumed noisy and the other noiseless.

The phase follower of Figure 4.2 can be used, e.g., for clock recovery in communication systems. If a noisy input signal and a noiseless VCO are assumed, the PLL will modulate the VCO output signal with the input noise. In this case the phase noise of the input signal is filtered by the low-pass function  $H_{\theta}(s)$ , and the disturbances outside the closed loop bandwidth are attenuated. The phase noise of the recovered signal is minimised by decreasing the closed loop bandwidth.

Phase-locking can also be used to improve the phase noise characteristics and frequency tunability of a VCO by locking it to a low noise reference signal. If a noiseless reference signal and a noisy VCO are assumed, the VCO output is filtered by the high-pass function  $H_{\phi}(s)$  and the PLL will attenuate the VCO's own phase noise inside the closed loop bandwidth. The phase noise of the VCO output signal is minimised by increasing the closed loop bandwidth.

### 4.3.2 Phase-lock acquisition

Four important parameters can be defined for the PLL: hold-in range, pull-in range, pull-in time, and lock-in range [45]. The ranges are defined as frequency ranges around the wanted carrier frequency. The hold-in range is the largest, and it is defined as the maximum deviation in the reference frequency while keeping the VCO locked. An unlocked PLL can pull a VCO frequency that is inside its pull-in range into the lock-in range within the pull-in time. While the VCO is inside the pull-in range, 'cycle slipping' can occur, i.e. it takes a couple of cycles before the VCO is locked. If the VCO is inside the lock-in range, it will lock within the same cycle and no cycle slipping can occur.

The hold-in range of a PLL using a sinusoidal phase detector (both input signals are sinusoidal) can be derived to be [45]

$$|\Delta f_{hold}| = \frac{1}{2\pi} K_d K_0 F(0). \quad (4.11)$$

In (4.11),  $F(0)$  is the loop filter DC gain, which for a passive loop filter is  $F(0) = 1$  and for an active filter  $F(0) = A$ . It would seem that an arbitrary large hold range is possible just by increasing the DC gain, but in reality the hold range is limited by the output voltage range of the operational amplifier and the maximum control voltage accepted by the VCO. If the control voltage reaches either of these limits, the loop will drop out of lock.

The pull-in range of a PLL with a sinusoidal phase detector is [45]

$$|\Delta f_p| = \frac{1}{2\pi} \sqrt{2K_d^2 K_0^2 F(0)F(\infty)}, \quad (4.12)$$

where  $F(\infty)$  is the loop filter gain at infinity. For a lag-lead type loop filter,  $F(\infty) = \frac{\tau_2}{\tau_1}$ , and

(4.12) simplifies to

$$|\Delta f_p| = \frac{K_d K_0}{2\pi} \sqrt{2F(0) \frac{\tau_2}{\tau_1}}. \quad (4.13)$$

The time required to pull the VCO from the middle of the pull-in range to the edge of the lock-in range is called the pull-in time of the PLL. If  $\Delta\omega$  is the initial frequency error of the VCO, the pull-in time can be approximated as [45]

$$T_p(\Delta\omega) = \frac{(\Delta\omega)^2 \tau_2}{\left(\frac{K_d K_0 \tau_2}{\tau_1}\right)^2} = \frac{(\Delta\omega)^2 \tau_1^2}{(K_d K_0)^2 \tau_2}. \quad (4.14)$$

The lock-in range is the same as the hold-in range for a first order PLL. However, the observed lock-in range of second and higher order loops is considerably smaller than the hold-in range. The lock-in range of a PLL using a sinusoidal phase detector can be approximated as [45]

$$|\Delta f_L| = \frac{1}{2\pi} K_d K_0 F(\infty) = \frac{1}{2\pi} K_d K_0 \frac{\tau_2}{\tau_1}. \quad (4.15)$$

The formulas presented in this chapter assume sinusoidal reference and VCO output frequencies. They give very optimistic values and are based on assumptions of perfectly linear and frequency independent components. A phase detector can also operate on nonsinusoidal input waveforms, e.g. triangle and square waves. The hold-in, pull-in, and lock-in ranges for nonsinusoidal signals are determined by the phase detector characteristics, and can be larger or smaller than the ones predicted by (4.11)–(4.15).

## 4.4 Modeling and design of a phase-locked BWO source for 180–714 GHz

### 4.4.1 Operating principle of the BWO

The backward-wave oscillator is an electron tube oscillator, whose operation is based on the interaction between a collimated electron beam and an electromagnetic wave propagating along the backward (reverse) direction in a periodical slow-wave structure. A BWO can have very wide electrical tuning range (up to 40%) and relatively high output power at frequencies up to 1200 GHz [50]. Disadvantages are the large weight and size of the device with its strong magnets, required high-voltage power supply and water cooling, high power consumption, and the limited lifetime of the tube [50,51]. The available output power decreases with frequency, mainly due to the increased propagation losses, non-ideal electron beam, and manufacturing difficulties of the slow-wave structure.

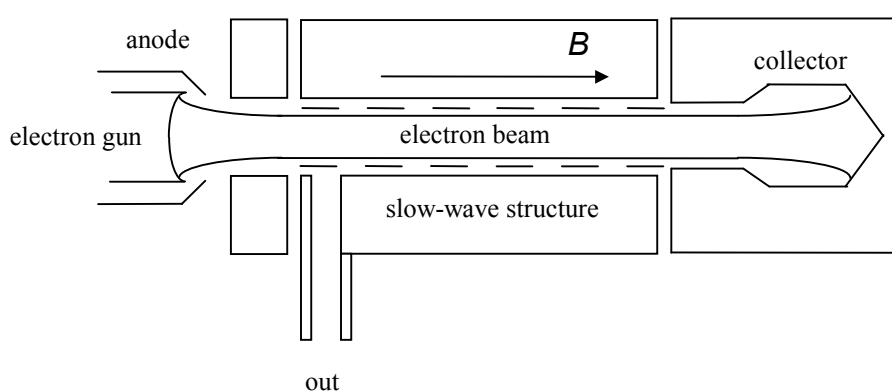


Figure 4.4 A schematic view of a typical BWO tube [50].

The configuration of a typical BWO tube is shown in Figure 4.4 [50]. The electron beam emitted by the electron gun is collimated with a strong magnetic field along its axial direction. Either permanent or solenoid magnets can be used to produce the required fields in the order of 1 T. The longitudinal component of the electromagnetic wave propagating inside the periodical slow-wave structure modulates the velocity and density of the electrons, and consequently some of the electron beams kinetic energy is transferred to the electromagnetic wave. Strong interaction is possible if the phase velocity of the wave is close to the electron velocity. The design and construction of different slow-wave structures are analyzed in detail in [50].

The efficiency of a typical BWO is very low and only about 1% of the original beam energy is coupled to the output waveguide [51]. Simulation results using improved individual BWO components including a depressed collector and a better transition from the slow-wave structure to the output waveguide are presented in [51]. The simulations with the improved components indicate that an order of magnitude improvement in the efficiency is possible at 600–700 GHz, making water cooling unnecessary.

The spectral quality of the BWO is determined mainly by the quality of the high-voltage power supply. The cathode voltage is DC, but its residual AC ripple modulates directly the output spectrum and shows as noise sidebands around the carrier frequency [50]. The beam current fluctuations due to the high-voltage and heating current ripples also increase the sideband noise. The spectral quality and frequency stability of a free-running BWO are quite

poor, but they can be improved by phase-locking it to a stable reference, as is shown in the next section and in [P5]. Table 4.1 shows the properties of the BWO tubes in use at the Radio Laboratory of HUT [52].

**Table 4.1 Properties of the BWOs at HUT Radio Lab [52].**

Type	Freq. range GHz	Wavelength mm	$\Delta f / \Delta V$ MHz/V	DC-range kV	Output power mW
OB-66	179 - 263	1.67 - 1.14	35.5	1.0 - 4.0	10.0 - 50.0
OB-65	258 - 375	1.16 - 0.80	54.0	1.0 - 4.0	10.0 - 40.0
OB-32	370 - 535	0.81 - 0.56	73.3	1.0 - 5.0	1.0 - 5.0
OB-74	526 - 714	0.57 - 0.42	76.0	1.5 - 6.0	5.0 - 10.0

#### 4.4.2 Design of the BWO-PLL

A phase-locked submillimetre wave BWO is very useful in vector antenna measurements with the MVNA analyser introduced in Chapter 3. The design, modeling, and construction of a PLL system for BWOs are presented in this chapter and partly in [P5]. The association to the MVNA and the obtained improvement in dynamic range are shown in Section 4.5 and in [P5].

The design for a phase-locking system applicable to the BWOs presented in Table 4.1 was started with selection of the loop topology. The dual-loop scheme based on separate frequency- and phase-locked loops used in [53] and [54] was an attractive option, but the system would become very complicated. Good results have been obtained earlier at 600 GHz with a simple 2<sup>nd</sup> order phase-locked loop [55], so this was chosen as the loop topology. The used topology is based on an active lag-lead type loop filter described in Section 4.3.1.

The submm wave output signal is downconverted with a harmonic mixer to the intermediate frequency (IF) of the PLL. A simple integrated waveguide directional coupler and a Schottky diode mixer (ABmm DC-HM-F-FB) can be used across the 180–375 GHz range. Above this it is advantageous to use a quasioptical power divider and a sensitive low-harmonic mixer to guarantee a strong enough beat signal for phase detection. The IF frequency of the PLL depends on the phase detector and the IF amplifiers. In the constructed system, it can be selected between 40–400 MHz.

##### 4.4.2.1 Loop filter

The loop filter determines the dynamic characteristics of the loop, so it must be designed very carefully. The initial design for the loop filter was done according to the rules-of-thumb presented in [45,48]. The design parameters were then verified in the APLAC circuit simulator [56]. The spectral width of a free-running BWO with a state-of-the-art high-voltage power supply is about 1 MHz, so the closed loop bandwidth should be wider than that in order to cleanse most of the sideband noise. The presented design aims for a bandwidth of 30 MHz

for compatibility with lower quality switched-mode power supplies having noise sidebands extending to 20 MHz. The input parameters used in the initial design are:

$$\begin{aligned} \text{VCO gain (BWO OB-65):} & \quad K_0 = 54 \text{ MHz / V} = 339,292 \cdot 10^6 \text{ rad / sV} \\ \text{phase detector gain (MPD-21):} & \quad K_d = -400 \text{ mV / rad} \\ \text{unity gain (closed loop) bandwidth :} & \quad \omega_3 = 2\xi_a \omega_{n,a} = 2\pi \cdot 30 \text{ MHz} \end{aligned}$$

The frequency response of a 2<sup>nd</sup> order active loop filter can be studied with the Bode diagram presented in Figure 4.5 [45]. At low frequencies, the VCO integration is dominant, causing the amplitude to fall at a rate of  $-6$  dB/octave and the phase to be  $-90^\circ$ . The 2<sup>nd</sup> order active loop filter has a pole at angular frequency

$$\omega_1 = \frac{1}{A \tau_{1,a}}, \quad (4.16)$$

which causes the amplitude to fall at a rate of  $-12$  dB/octave and the phase to approach  $-180^\circ$ .

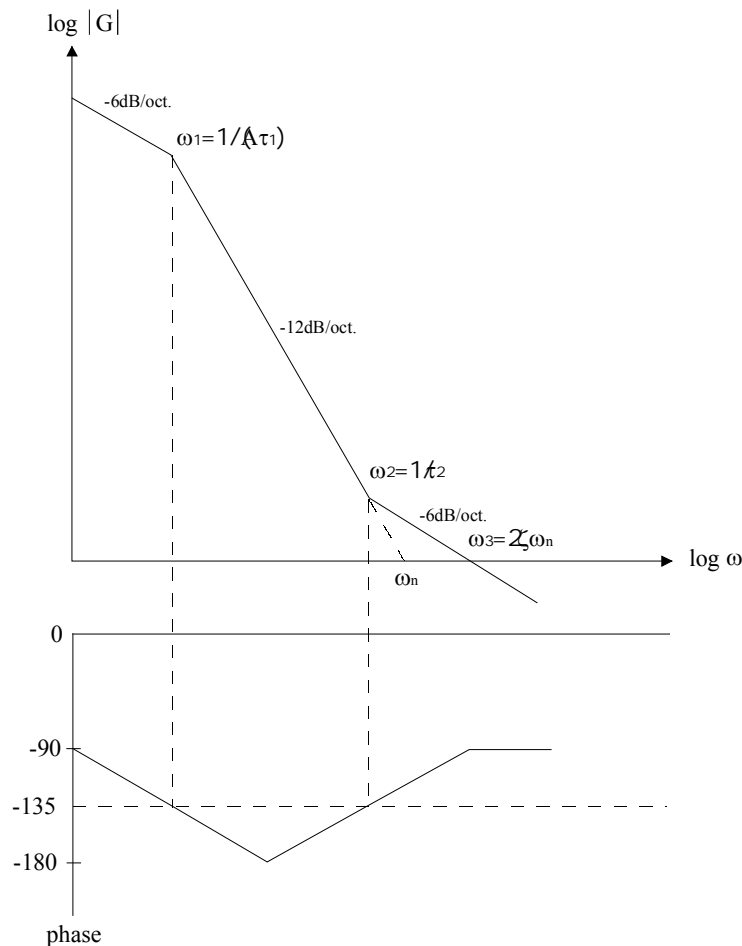


Figure 4.5 Bode diagram for a 2<sup>nd</sup> order active loop filter [45].

The stabilising zero at angular frequency of

$$\omega_2 = \frac{1}{\tau_{2,a}} \quad (4.17)$$

causes the amplitude fall rate to return to  $-6$  dB/octave and the phase to return to  $-90^\circ$  at high frequencies.

The loop natural angular frequency  $\omega_{n,a}$  is defined as the frequency where the  $-12$  dB/octave falling line crosses the unity gain line. If  $\omega_{n,a} = \omega_3$ , the damping factor is  $\xi_a = 0.5$ . Usually it is advantageous to select  $\omega_{n,a} > \omega_3$  [45,46,48].

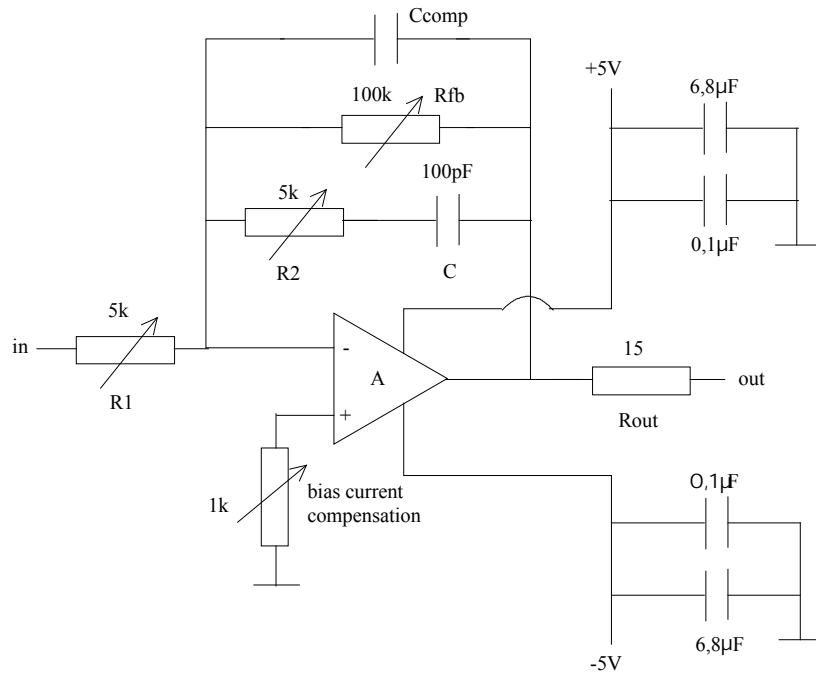


Figure 4.6 Schematic diagram of the constructed loop filter.

Selection of the  $\omega_2$  can be done according to a rule-of-thumb presented in [48] to ensure comfortable phase margin and loop stability:  $\omega_2 = \omega_3 / 4 = 47.124 \cdot 10^6$  rad/s. This selection ends up with  $\xi_a = 1.0$  and  $\omega_{n,a} = 0.5\omega_3$ , which agree with the design of [54]. The ratio between the  $\tau_{1,\alpha}$  and  $\tau_{2,\alpha}$  (and the  $R_1/R_2$  ratio) can be calculated from the unity gain bandwidth by substituting the formula for the loop natural frequency. By selecting a suitable value for  $C$  one can get a value for  $R_2$  from (4.17) and (4.7). Schematic diagram of the loop filter is shown in Figure 4.6 and its component values from the initial design are:  $R_1 = 153\Omega$ ,  $R_2 = 212\Omega$ , and  $C = 100\text{pF}$ .

#### 4.4.2.2 PLL signal coupling to the BWO

The output frequency of the BWO depends mainly on its accelerating voltage. The dependence is close to linear across the PLL bandwidth. The PLL control voltage can be coupled to the cathode high-voltage (0–6kV) like in [53–55], or to the anode at ground potential. The constructed system in this thesis modulates the anode voltage, as shown in Figure 4.7. The advantages of using anode modulation are that a wideband high-voltage optocoupler is not needed and the PLL signal can be coupled directly to the BWO tube. The

BWO output waveguide is galvanically isolated from the tube ground, which in turn is lifted from the laboratory ground by a  $100\Omega$  resistor connected in parallel with two back-to-back zener diodes. If the resistor breaks, the zeners will prevent the BWO anode from floating to a dangerous voltage level, which could damage the sensitive phase-lock electronics.

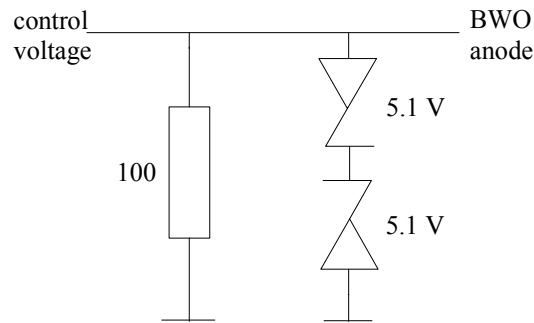


Figure 4.7 PLL control voltage coupling to the BWO anode.

#### 4.4.3 APLAC circuit simulator model of the BWO-PLL

The loop filter of Figure 4.6 and the whole PLL were modeled in the APLAC<sup>TM</sup> circuit simulator. APLAC has good internal system level linear models for various PLL component like phase detectors, dividers, and VCOs [56]. The manufacturer's macro model for the loop filter op amp OPA687 worked with the loop filter AC-simulations, but it caused converging problems in the system simulator when modeling the whole PLL. For this reason, the op amp was modeled with the APLACs simple 'op amp'-component by specifying its poles (from the datasheet) in the frequency domain, giving accurate enough response at least up to 1 GHz.

The amplitude and phase responses from the loop filter AC-simulations with the component values from the initial design are shown in Figure 4.8. The unity gain frequency is 140 MHz and the corresponding phase margin is  $132^\circ$ , ensuring stability. The shape of the curves is very similar to the ones in Figure 4.5.

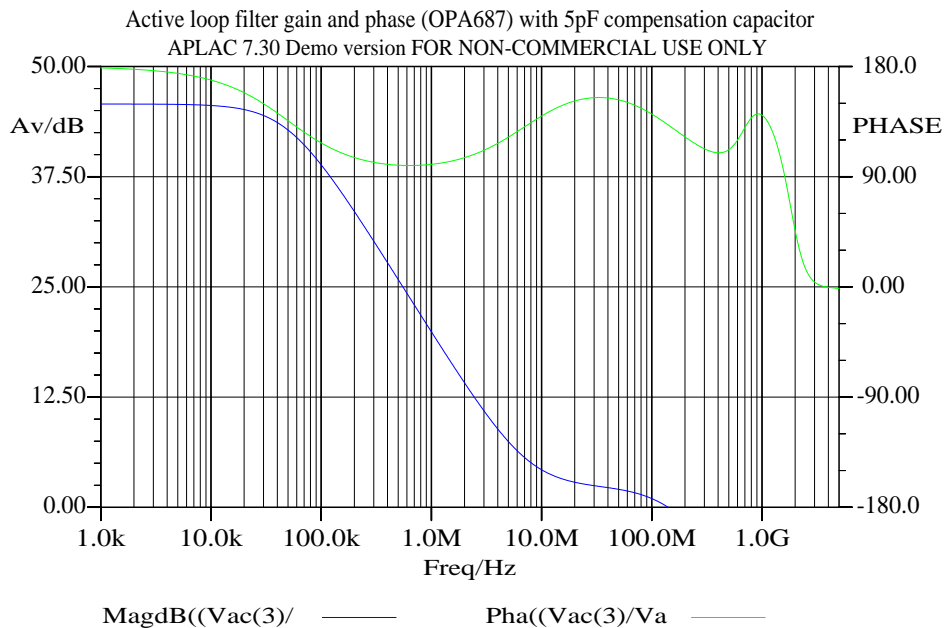


Figure 4.8 The simulated frequency response of the loop filter.

The phase detector, VCO, and the loop filter were simulated in a closed loop configuration with the APLAC system simulator. The simulated amplitude and phase responses of the whole PLL are shown in Figure 4.9. The amplitude curve is of the low-pass type as it should, and with a closed loop bandwidth of about 26 MHz (the design value was 30 MHz). The small difference between the simulated closed loop bandwidth and the design value is caused by the better accuracy of the simulator compared to the rules-of-thumb. The phase curve behaves smoothly and is turned  $55^\circ$  at 26 MHz, indicating a phase margin of  $125^\circ$  and stability.

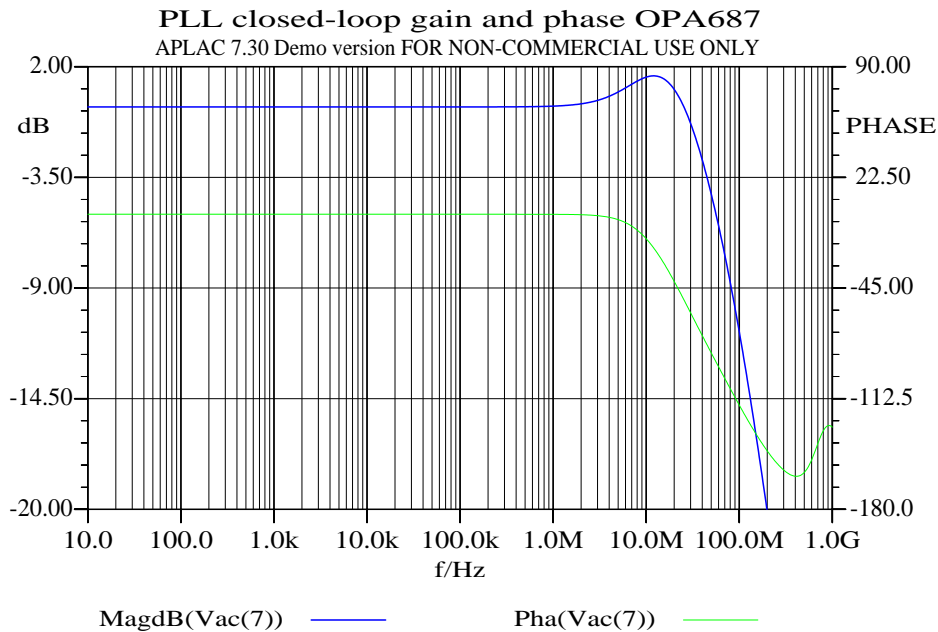


Figure 4.9 The simulated closed loop frequency response.

#### 4.4.4 Construction and testing of the BWO-PLL

The loop filter was constructed on a PCB with all the pole and gain setting resistors as trimmer potentiometers with the initial design values. The BWO tube enclosures were modified to include the ground lifting resistor, zeners, and a SMA connector for the PLL signal input. The PLL was found to operate as designed and simulated. The measured maximum closed loop bandwidth is 20 MHz, which is somewhat lower than the 26 MHz predicted by the simulator [P5]. The difference is believed to be caused by additional phase shifts due to parasitic components (like inductances and capacitances in the potentiometers) not included in the model and variations in the VCO gain with frequency compared to the average value of 54 MHz/V.

The best phase noise performance was obtained by reducing the closed loop bandwidth to 4 MHz. The measured single sideband phase noise for the BWO-PLL at 311 GHz is presented in Figure 4.10 and in [P5], and it is below  $-91$  dBc/Hz at offset frequencies  $f_m=1$  kHz – 2 MHz. The phase noise measurements were carried out at an IF frequency of 300 MHz and, of course, include the contribution of the frequency multiplied local oscillator signal used in downconversion. The measured phase noise level agrees very well with the results presented in [57] measured for a 350 GHz phase-locked BWO with a quasioptical frequency discriminator. Another highly sensitive quasioptical phase noise measurement system is

presented in [58], showing phase noise levels for a free-running BWO at 160 GHz to be between  $-30$  to  $-110$  dBc/Hz at offset frequencies  $f_m=10$  kHz – 10 MHz. The free-running BWO curve in Figure 4.10 is not a ‘true’ phase noise plot but instead shows an envelope of the noisy signal for comparison.

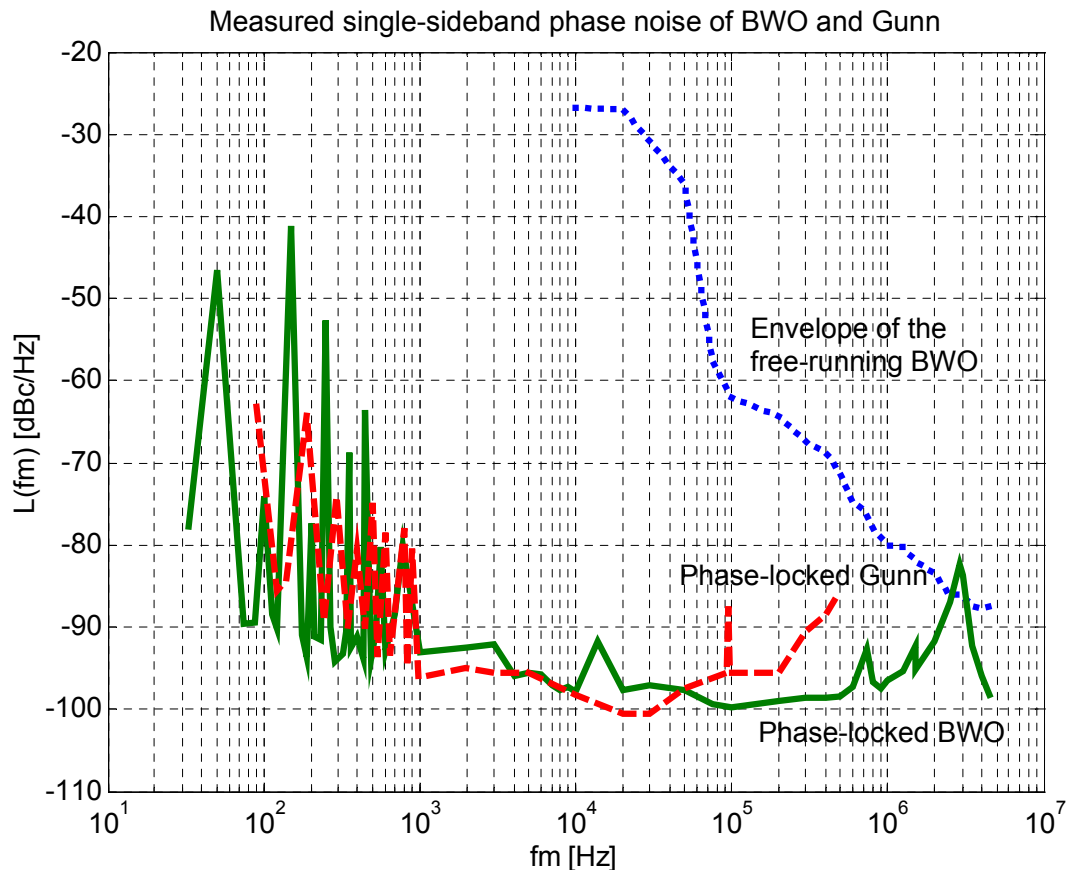


Figure 4.10 Phase noise plots of BWO at 311 GHz and frequency-multiplied Gunn at 310 GHz.

Figure 4.10 shows also the measured phase noise of the Gunn-oscillator in the ESA-1 extension. This was measured at the IF frequency of the Gunn phase-lock at 30 MHz and includes the contribution of the frequency multiplied local oscillator signal. The Gunn frequency is 103.33 GHz, and the shown phase noise was frequency-scaled to 310 GHz by adding 9.5 dB (phase noise increases as the square of the multiplication factor, i.e.  $10\log 3^2$ ) to the measured curve. Comparison of the BWO and Gunn signals shows that the difference in the phase noise floor is only a few dBs inside the vector receiver bandwidth of 10 kHz. The reason that the BWO phase noise is lower close to the carrier is that a state-of-the-art laboratory signal generator is used as the local oscillator, and in the Gunn characterisation the MVNA system’s own YIG synthesizer is used. The line frequency harmonics shown at integer multiples of 50 Hz are present in both spectrums. Part of their measured amplitude comes from the spectrum analyser itself. The bandwidths of the line-frequency related peaks are so narrow that not much energy from the carrier is lost in them.

It might have been useful to be able to measure the phase noise spectrum closer to the carrier, but PLL analysers capable of this are generally not portable and were not available for the

tests. The phase noise plots show that the source powers are emitted in very narrow lines, probably within a few Hz. This permits to use narrow equivalent receiver bandwidths of 10–20 Hz in the vector analyser thus increasing the observed signal-to-noise ratio. The sampling speed of the vector receiver is fixed at 10 kHz, and software averaging is used to reduce the equivalent bandwidth.

The pull-in range of the PLL was measured to be  $\pm 10$  MHz, and the hold-in range  $\pm 20$  MHz. The lock-in range was not measured because a specialised PLL analyser was not available for the tests.

The PLL system has been tested with BWOs at frequencies of 180–400 GHz and 600–650 GHz. The loop filter transfer function needs to be adjusted with the trimmers to adapt for a different VCO gain factor (see  $\Delta f / \Delta V$  in Table 4.1). A beat signal with an amplitude of +7 dBm and SNR > 20 dB (measured inside the closed-loop bandwidth) at the phase detector are required for reliable, spurious-free operation.

#### 4.5 Association of the BWO to the submm-wave vector network analyser

A BWO tube has been associated with the MVNA vector network analyser between 300–400 GHz. Schematic layout of the test system is shown in Figure 4.11 [P5]. The MVNA provides the local oscillator (YIG 8–18 GHz) and phase-lock reference signals. Coherent detection is obtained by using signals from the same base reference in the receiver. The selection of the exact IF frequency for the BWO-PLL between 40–400 MHz is done automatically by the MVNA.

In addition to the nonlinear voltage/frequency relation of the BWO tube, the output power varies 10–15 dB with frequency. The loop filter requires manual tuning between each change of frequency for optimal phase noise performance, and wide phase-locked frequency sweeps are thus not possible. This is not a problem for the hologram CATR testing since the hologram is also optimised for a certain frequency.

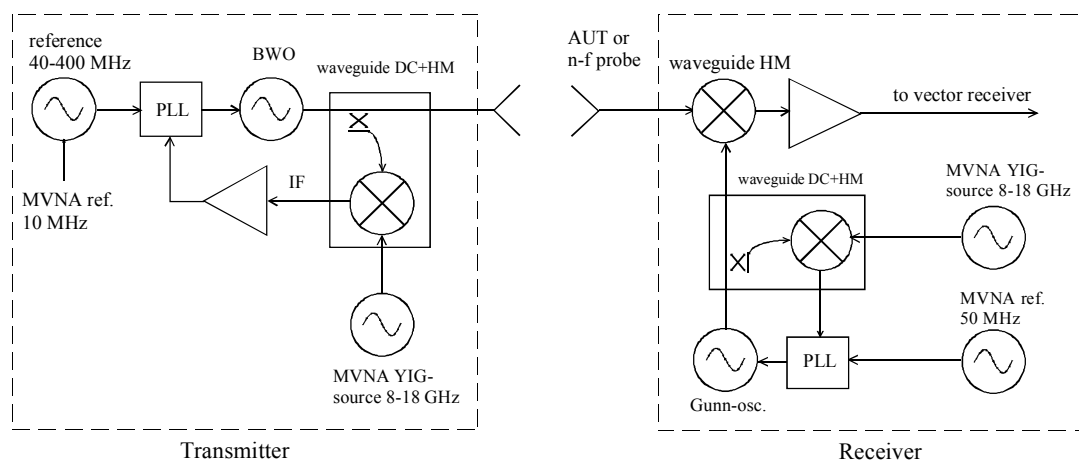


Figure 4.11 BWO association to the MVNA analyser system.

#### 4.5.1 Measured dynamic range improvement over the standard source system

The dynamic range improvement over the standard ESA-1 source (introduced in Section 3.2.1) by using a BWO was studied with both power meter measurements and transmission ( $S_{21}$ ) tests with the vector analyser [P5]. Comparisons between the frequency-multiplied Gunn oscillator (ABmm ESA-1) and the BWO were done at several frequencies between 300–400 GHz using the same receiver. According to the transmission tests, the dynamic range of the measurement system can be improved by 16–20 dB in the 300–400 GHz range by using the phase-locked BWO (see Figure 4.12). With the BWO, a flange-to-flange dynamic range of 145 dB is observed across the 300–400 GHz range.

A calorimeter-based power meter Dorado DPM-2A was used to measure the absolute power levels from the sources between 300–400 GHz. Output power from the frequency-multiplied Gunn oscillator varied between  $-6$  to  $-7$  dBm, and the BWO output power between  $+9$  to  $+13$  dBm. The measured power level difference equals the observed difference in dynamic range, so it can be stated that the BWO-PLL system works well and the emitted signal is very narrow. The BWO output power was measured after two waveguide transitions (WR-10 to WR-8 and WR-8 to WR-3) and a directional coupler. The unwanted modes inherent in the oversized BWO output waveguide [51] cannot propagate through the final transition, so the measured power is on the fundamental mode.

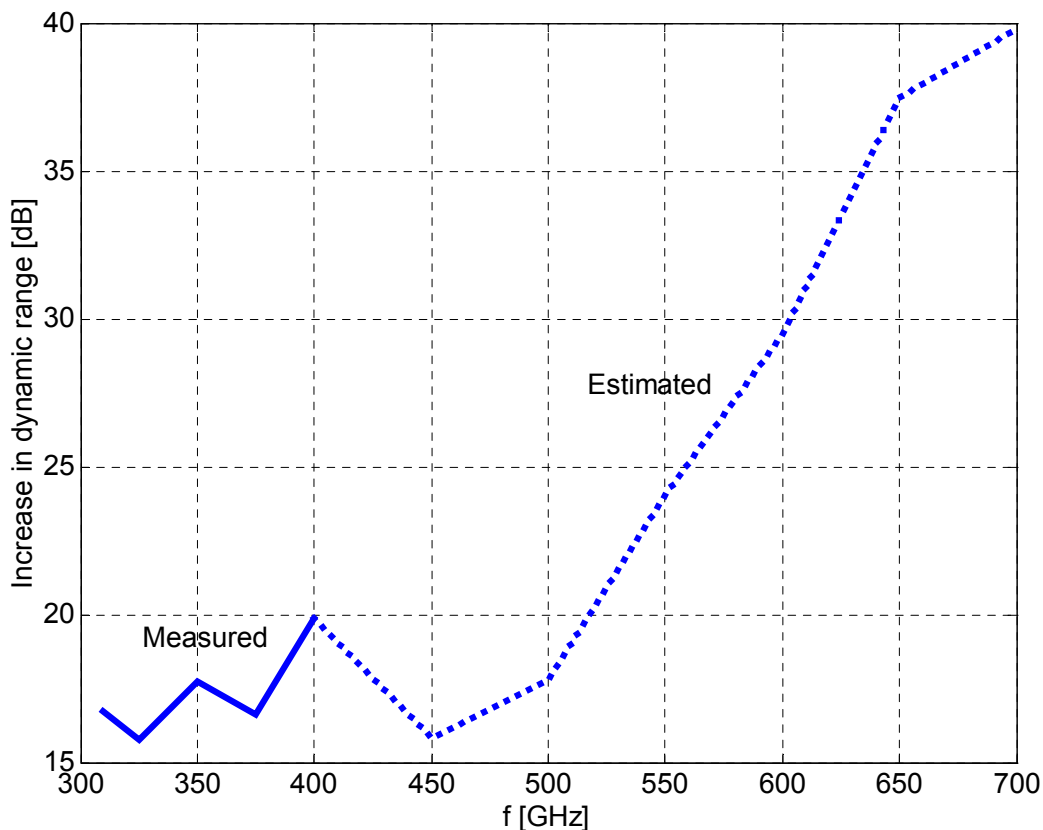


Figure 4.12 Measured and estimated improvement in dynamic range by using a BWO instead of the standard ESA-1 source.

An estimate for the dynamic range improvement of 15–40 dB at the 450–700 GHz range is based on the approximate source power differences between the frequency-multiplied Gunn oscillator (–11 to –35 dBm) and the BWO (+1 to +10 dBm). The output power from the solid-state source decreases rapidly above 500 GHz, which explains the large increase in dynamic range when using the BWO. The power levels between 400–700 GHz were not measured since a calibrated power meter was not available, and they are based on the information from the manufacturers datasheets. A 3 dB loss was assumed for the BWO waveguide transitions and unwanted mode truncation.

## 5 Phase-correction system for planar near-field measurements

### 5.1 Phase and amplitude effects of reference cables

A theoretical analysis of the electromagnetic fields in a bent coaxial cable is presented in [59]. The analysis shows that bending causes changes in the propagation constant that are dependent on the bending radius and the signal frequency. The propagation constant may increase or decrease compared to that of a straight line and, assuming small curvatures, its change in magnitude is inversely proportional to the square of the radius of curvature. Further, frequency dispersion (frequency dependence of the propagation constant or phase velocity) causes different frequencies to experience different delays when travelling through the cable. Dispersion effects are minimised by not allowing strong bending of the cable in the measurements. Too strong bending is prevented by the cable armouring, available in specially designed flex cables. One should also be careful about the dispersion effects if the flex cable is routed in cable tracks like in near-field scanners.

Methods for accurately measuring and compensating changes in the electrical path length of transmission media have been developed during the years for antenna arrays used in radio astronomy [60–65]. The arrays can consist of many antennas located tens of kilometres apart or even in space, and their associated receivers need to have a common phase reference. The phase reference signal from a common master oscillator (e.g. a hydrogen maser) can be provided to individual receivers by means of cables, optical fibers, or microwave links. Regardless of the transport medium, the reference signal experiences phase variations due to, e.g., temperature variations, frequency dispersion, and connector mismatches at the antenna stations.

Synchronization of the reference phases at the antennas can be done by using round-trip phase measurement techniques. Commonly used techniques in astronomical arrays include the use of a modulated reflector [61], the frequency offset technique [62], and the automatically correcting system using frequency translation at antenna stations [63]. Measured phase errors can be compensated either in the post-processing data analysis, in real-time by using adjustable phase shifters, or automatically by sampling and combining two signals traveling into opposite directions in the cable [60]. A digital phase shifter for accurately controlling and rotating the phase of microwave signals designed for the Australia Telescope array is presented in [64]. The phase shifter is based on digital dividers, counters, and offset-frequency phase-locked loops, and the achievable resolution in adjusting the phase of a 10 GHz signal is  $0.18^\circ$ .

Space VLBI (Very Long Baseline Interferometry) satellites use two-way microwave timing links to establish a stable reference frequency onboard the satellite [65]. The ground station transmits timing information derived from its hydrogen maser clock, and the timing link transponder at the satellite returns the signal on a slightly different frequency band. The round-trip phase error due to atmospheric disturbances and the satellite velocity and distance can be measured at the ground station, and the uplink timing signal adjusted to compensate for the errors accordingly. Design and error analysis of such a system are presented in [65].

Optical fibres can also be used to transfer phase reference signals to, e.g., antenna arrays. They have some advantages over conventional coaxial cables and waveguides including low loss, low thermal coefficient of delay, low susceptibility to interference, light weight, and large bandwidth [66]. Fiber optics reference distribution has become the preferred choice in modern antenna arrays. Similar round-trip techniques discussed above can be applied to optical fibres carrying microwave signals for ultimate phase stability [66,67].

The near-field scanning and the CATR quiet-zone quality verification procedures need highly accurate vector measurements with a moving receiver. The associated flexing cables, and especially the cable carrying the microwave local oscillator signal, introduce amplitude and phase errors to the measured vector values of the field [P1,O18,12,68–70]. The errors are mostly due to changes in the cable's electrical length caused by bending and thermal expansion/compression. According to the experiments presented in [68], the amplitude effects of cable flexing are negligible when remote mixing is used, i.e. downconversion is done close to the near-field probe. If the downconversion is done at the network analyser using local mixing, then the amplitude errors can be severe. The phase errors due to cable flexing are considerable in both cases.

The new phase correction system based on the use of a pilot signal is presented in the next section and in [P1,O18]. Basically, the system is an interferometer which measures the phase difference between the reference and the round-trip reflected signals. In the author's view, the use of a round-trip pilot signal to continuously measure the phase changes due to cable flexing in a near-field scanner is a new idea and has not been published earlier.

## **5.2 Construction of the phase-correction system**

### **5.2.1 Description of operation**

The phase error measurement systems proposed in earlier studies, e.g. in [68–70], are not suitable for continuous operation and integration with the MVNA. The novel system designed in this thesis and published in [P1] is based on a new idea and designed to work with the MVNA. It provides information for real-time correction of the phase errors caused by cable flexing during scanning.

The real-time phase error measurement and correction system is based on the use of a lower frequency pilot signal that is injected to the microwave cable carrying the local oscillator signal for the submm-wave receiver. The pilot signal gets reflected back into the cable from the waveguide high-pass filter at the receiver and is coupled to a phase detector. A digital voltmeter (DVM) is used to sample the detected DC voltage. The near-field scanner control software triggers the DVM at each sampling grid point and reads back the data through GPIB-bus. After calibrating the phase detector coefficient (voltage/phase relationship), the measured vector values of the field can be corrected as a postprocessing step. The demonstrator system was constructed to operate on 310 GHz. The local oscillator (LO) frequency for the receiver is 17.2 GHz, and the pilot frequency was chosen to be 14.5 GHz since it is the closest directivity maximum (40 dB) of the coupler to the LO frequency. A schematic diagram of the constructed system is shown in Figure 5.1.

The calibration procedure, based on introducing small known phase shifts, is described in detail in [P1]. The directivity of the directional coupler is a critical parameter regarding the

accuracy of the correction. An error analysis of the coupler-related phase offsets is given in [P1], showing that offset levels of 1–2° are possible when the directivity is over 40 dB. The multiple reflections due to imperfect matching also introduce phase offsets at the phase detector. Their effect is analysed in Section 5.2.3 along with the total error budget in the pilot signal phase measurement.

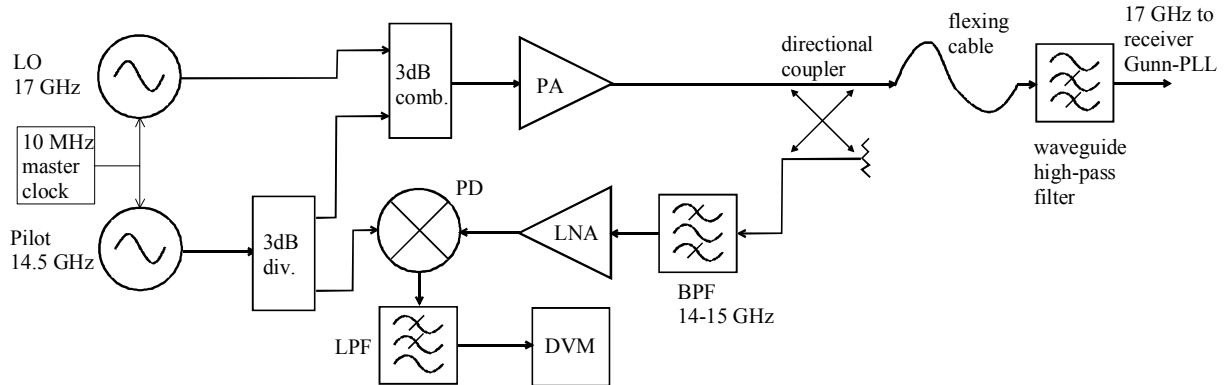


Figure 5.1 Schematic diagram of the phase error measurement system.

### 5.2.3 Error analysis

Mismatches in both ends of the flexible cable introduce multiple reflections that can alter the response of the phase detector and the phase correction system [60,69]. A simplified diagram suitable for analysing the effect of the real-world VSWRs on both sides of the cable is shown in Figure 5.2.

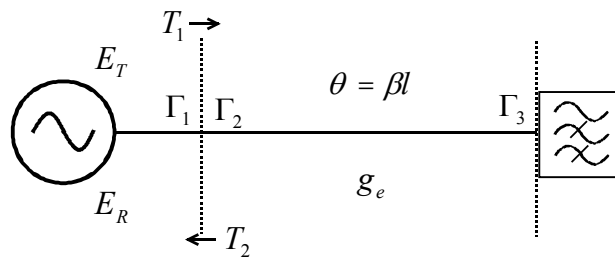


Figure 5.2 Illustration of multiple reflections in the cable.

At the interface between the directional coupler and the cable, the reflection coefficients are

$$\Gamma_1 = \rho_1 e^{j\phi_1} \quad (5.1)$$

$$\Gamma_2 = -\rho_1 e^{j\phi_1} \quad (5.2)$$

and the corresponding transmission coefficients

$$T_1 = 1 + \Gamma_1 = 1 + \rho_1 e^{j\phi_1} \quad (5.3)$$

$$T_2 = 1 - \Gamma_1 = 1 - \rho_1 e^{j\phi_1}. \quad (5.4)$$

Similarly, the reflection coefficient of the reflective high-pass filter is

$$\Gamma_3 = \rho_3 e^{j\phi_3} . \quad (5.5)$$

Now, the electrical field returning from the cable can be formulated as

$$\begin{aligned} E_R &= E_T \left[ \Gamma_1 + T_1 g_e \Gamma_3 g_e T_2 e^{-j2\theta} + T_1 g_e \Gamma_3 g_e \Gamma_2 g_e \Gamma_3 g_e T_2 e^{-j4\theta} + \dots \right] \\ &= E_T \left[ \Gamma_1 + T_1 T_2 \Gamma_3 g_e^2 e^{-j2\theta} + T_1 T_2 \Gamma_2 \Gamma_3^2 g_e^4 e^{-j4\theta} \left( 1 + \Gamma_2 \Gamma_3 g_e^2 e^{-j2\theta} + \dots \right) \right] \\ &= E_T \left[ \Gamma_1 + T_1 T_2 \Gamma_3 g_e^2 e^{-j2\theta} + \frac{T_1 T_2 \Gamma_2 \Gamma_3^2 g_e^4 e^{-j4\theta}}{1 - \Gamma_2 \Gamma_3 g_e^2 e^{-j2\theta}} \right] \end{aligned} \quad (5.6)$$

where  $E_T$  is the transmitted field,  $g_e$  the cable gain factor ( $g_e \leq 1$ ), and  $\theta = \beta l$  the electrical length of the cable. In deriving (5.6) it is taken into account that  $|\Gamma_2 \Gamma_3 g_e^2 e^{-j2\theta}| < 1$ , which certainly holds for all realistic values of the variables. Substituting (5.1)–(5.5) into (5.6) and re-arranging we get

$$E_R = E_T \left[ \rho_1 e^{j\phi_1} + \left( 1 - \rho_1^2 e^{j2\phi_1} \right) \rho_3 g_e^2 e^{j(\phi_3 - 2\theta)} - \frac{\left( 1 - \rho_1^2 e^{j2\phi_1} \right) \rho_1 \rho_3^2 g_e^4 e^{j(\phi_1 + 2\phi_3 - 4\theta)}}{1 + \rho_1 \rho_3 g_e^2 e^{j(\phi_1 + \phi_3 - 2\theta)}} \right] . \quad (5.7)$$

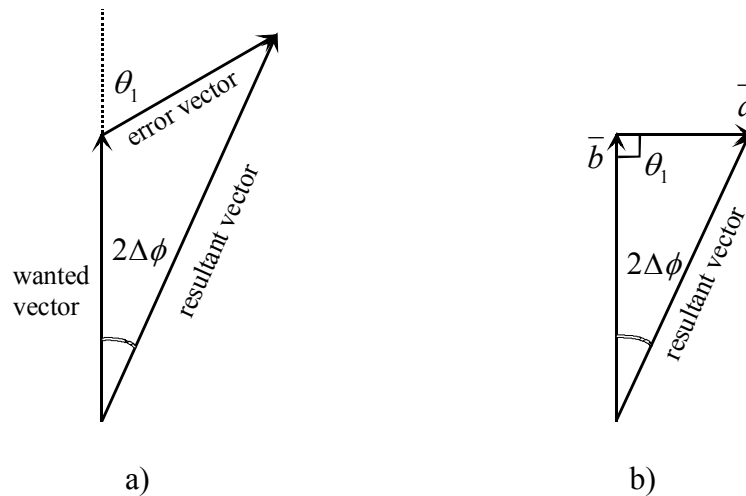


Figure 5.3 Vector notations: a) random error vector angle, b) maximum  $\Delta\phi$  when  $\theta_1 = 90^\circ$ .

The second term inside the brackets in (5.7) is the wanted signal reflected once from the reflective highpass filter, and the others are the error terms caused by unwanted reflections. Figure 5.3. a) shows the resulting electrical field vector at the phase detector input as the sum of the wanted vector and the error vector with random angle  $\theta_1$ . The phase angle between the wanted and the resultant vector is  $2\Delta\phi$ . The error caused by the multiple reflections to the corrected phase value is  $\Delta\phi$  since one half of the phase of the measured reflected signal (round-trip phase) is subtracted from the phase of the transmitted signal [60,69]. The maximum phase error due to reflections occurs when  $\theta_1 = 90^\circ$ , as indicated in Figure 5.3. b).

The error vector is noted as

$$\bar{a} = \rho_1 e^{j\phi_1} - \frac{(1 - \rho_1^2 e^{j2\phi_1}) \rho_1 \rho_3^2 g_e^4 e^{j(\phi_1 + 2\phi_3 - 4\theta)}}{1 + \rho_1 \rho_3 g_e^2 e^{j(\phi_1 + \phi_3 - 2\theta)}} \quad (5.8)$$

and the wanted vector as

$$\bar{b} = (1 - \rho_1^2 e^{j2\phi_1}) \rho_3 g_e^2 e^{j(\phi_3 - 2\theta)}. \quad (5.9)$$

Now we can get a limit for the phase error (after correction) caused by reflections as

$$\Delta\phi = \frac{1}{2} \arctan \left[ \left( \frac{\rho_1 e^{j\phi_1}}{(1 - \rho_1^2 e^{j2\phi_1}) \rho_3 g_e^2 e^{j(\phi_3 - 2\theta)}} - \frac{\rho_1 \rho_3 g_e^2 e^{j(\phi_1 + \phi_3 - 2\theta)}}{1 + \rho_1 \rho_3 g_e^2 e^{j(\phi_1 + \phi_3 - 2\theta)}} \right) \right]. \quad (5.10)$$

The value of (5.10) is always less than

$$\Delta\phi_{\max} = \frac{1}{2} \arctan \left[ \left( \frac{\rho_1}{(1 - \rho_1^2) \rho_3 g_e^2} + \frac{\rho_1 \rho_3 g_e^2}{1 + \rho_1 \rho_3 g_e^2} \right) \right]. \quad (5.11)$$

The phase error can now be calculated by specifying values for the variables. The loss of the 4 meter cable used with the near-field scanner (Stormflex II™ with soft neoprene armour by Reynolds Industries Ltd.) at 15 GHz was measured to be 5 dB corresponding to  $g_e = 0.562$ . Typical values of the reflection coefficients are [69]:  $\rho_1 = 0.2$  (VSWR=1.5/1) or 0.1 (VSWR=1.25/1), and  $\rho_3 = 0.95$ . The value of  $\Delta\phi_{\max}$  is 18.5° if  $\rho_1 = 0.2$  and 10.0° if  $\rho_1 = 0.1$ .

It is evident from equation (5.11) that the second term containing the multiple reflections quickly becomes negligible compared to the first term when  $g_e < 1$ . However, increasing the cable loss does not reduce the phase errors because it does not affect the reflection occurring at the directional coupler output, but instead reduces the amplitude of the wanted signal. The situation is illustrated in Figure 5.4 which shows the resulting total maximum phase error and the contributions of the two individual terms inside the brackets in (5.11) when the other term is assumed zero. Due to the nonlinearity of the arcus tangent function the resulting total maximum error is not exactly the sum of the contributions from the individual terms. A reflection coefficient of  $\rho_1 = 0.2$  was used in the calculations. The value of (5.11) approaches asymptotically 45° when the cable gain factor approaches zero ( $g_e \rightarrow 0$ ) since the maximum value of the arcus tangent function is 90°.

Changes in ambient temperature can also alter the phase velocity and the attenuation in the cable. The cable manufacturer specifies the sensitivity of these parameters for temperature changes. Typical values of phase variation over temperature range of 25–125°C for a phase stable cable like Sucoflex™ 104P is 0–0.1°/GHz\*m [71]. The change in attenuation with temperature due to changes in conductivity and dielectric characteristics is linear for Sucoflex™ cables, and the correction factor multiplying the nominal attenuation at 25°C varies between 0.85–1.2 for temperature range of –55...+125°C.

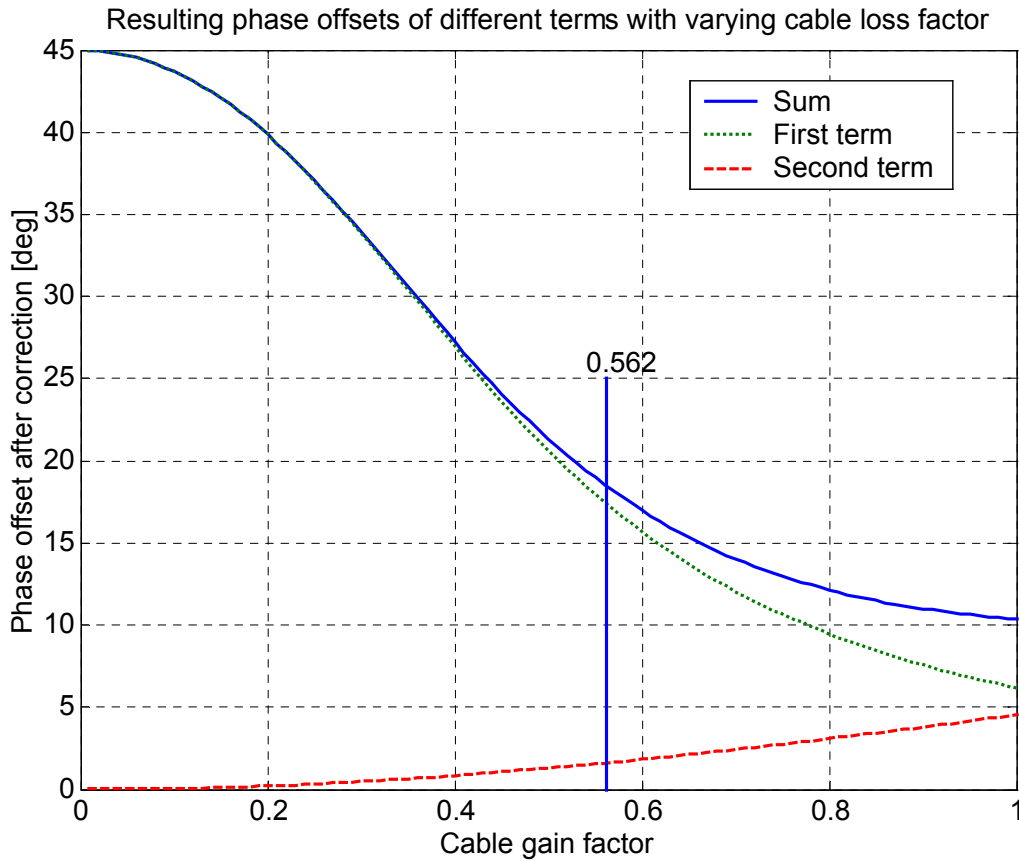


Figure 5.4 Resulting phase offsets from different terms of  $\Delta\phi_{\max}$  ( $\rho_1=0.2$ ).

The effect of  $\Delta\phi$  in the system of Figure 5.1, measuring relative phase changes in the cable, is to introduce a constant phase offset. A small phase offset does not seriously degrade the obtainable accuracy, if the offset remains stable during the measurement period. However, large phase offsets can set the phase detector away from its linear region of operation. In the developed phase correction system, small phase variations and thus linear phase detector characteristics are assumed. Figure 5.5 illustrates the deviation of the linearised model from the true sinusoidal characteristics of the double-balanced mixer used as the phase detector. According to this figure, it is reasonable to allow phase differences between  $-20\dots+20^\circ$  between the input signals. The actual measured round-trip phase error by the phase detector due to cable flexing is in the order of  $\pm 2^\circ$  which corresponds to about  $\pm 20^\circ$  at the final frequency of 310 GHz (see Figure 5.7 in the next section).

In addition to  $\Delta\phi$ , the phase offset caused by signal leakage in the directional coupler adds to the observed phase offset. The maximum phase offset due to leakage was calculated in [P1] to be  $6^\circ$  with the directivity of the coupler is 30 dB and the detected signals in quadrature. One half of this, i.e.,  $3^\circ$  is present after applying the round-trip phase correction. The resulting total worst-case phase offset after correction is then  $\Delta\phi + 3^\circ$ , corresponding to  $21.5^\circ$  if  $\rho_1=0.2$  and  $13.0^\circ$  if  $\rho_1=0.1$ . Especially the larger offset is not tolerable when very small relative phase changes are to be measured since it sets the phase detector close to the non-linear region.

The absolute phase offset needs not to be known because we are only interested in the relative phase change when the cable is flexed. The phase offset can be set to zero by fine-tuning the

pilot frequency and looking at the phase detector output voltage. Step-sizes between 1 kHz to 100 kHz in the pilot synthesizer are convenient in the adjustment. The system must be in thermal equilibrium before the adjustment takes place, otherwise a steady drifting of the phase is observed. Especially the phase responses of the amplifiers vary strongly with temperature. In the prototype system, a fan is used to stabilise the power amplifier's heatsink temperature. According to our experiments, this is enough to stabilise the phase offset for measurements lasting about one hour, but for example a water-cooled system baseplate should be used if longer measurement periods are required.

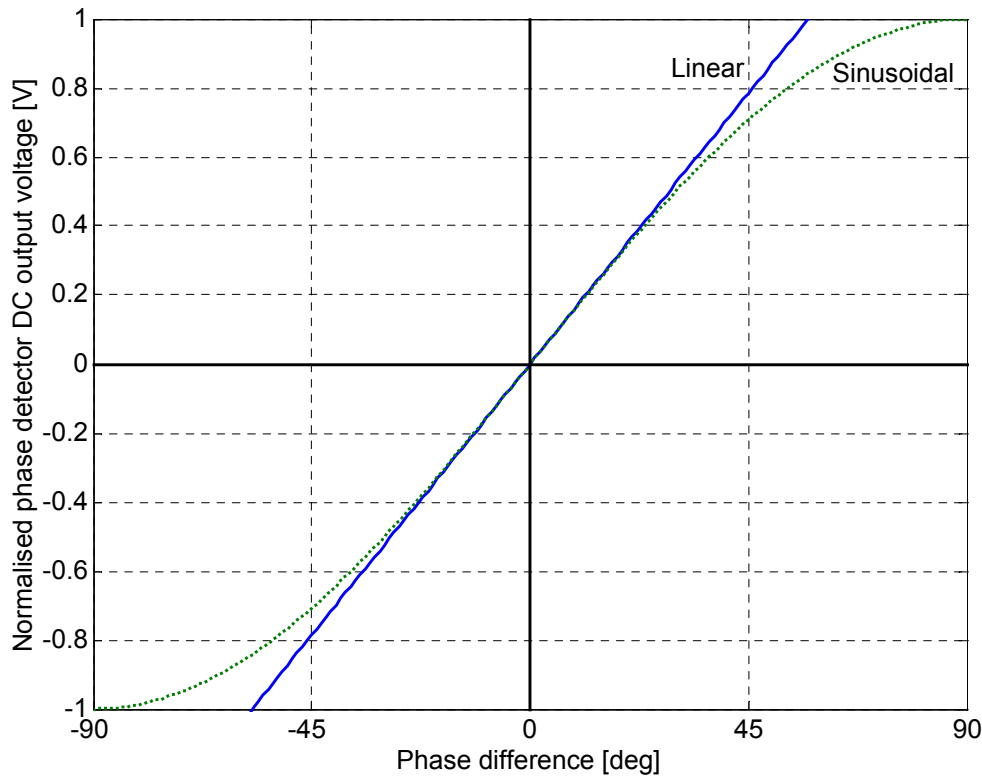


Figure 5.5 Normalised DC output voltage from linear and sinusoidal phase detectors.

The remaining phase error sources after removing the phase offsets are tabulated in Table 5.1. The temperature variation of the system components is assumed to be zero or negligible during the measurement period. The identified phase error sources contributing to the phase inaccuracy of the final corrected submillimetre wave signal are: digital voltmeter reading inaccuracy, error in determining the phase detector calibration coefficient, phase detector nonlinearity, and residual phase errors from other sources such as frequency dispersion. The calculations show that the variations in the cable's electrical length can be corrected with an accuracy of  $2^\circ$ .

**Table 5.1. Total phase error after removing phase offsets**

	Error estimate (peak-to-peak)	Phase error [deg] at	
		pilot freq. 14.50	submm freq. 310.00
Voltmeter inaccuracy	0.1 mV	0.01546	0.33052
Calibration error	0.01 deg	0.01000	0.21379
PD nonlinearity	0.02 deg	0.02000	0.42759
Residual errors	0.05 deg	0.05000	1.06897
<i>Total phase error [deg]</i>		<i>0.09546</i>	<i>2.04087</i>

Frequency dispersion in the cable can be a serious problem if strong bending and torsion are allowed. Dispersion or frequency dependence of the propagation coefficient arises when other modes than the fundamental TEM-mode can propagate in the cable [59]. Strong frequency dispersion can negate the usefulness of the proposed pilot signal phase correction method, since it assumes that the phase changes come only from changes in the electrical length of the cable. Also the power amplifier can have a frequency-dependent phase shift. However, at thermal equilibrium, the phase shifts remain constant over the measurement period and do not affect the relative phase measurement.

The frequency dispersion effect in the Stomflex II™ cable was studied by bending it into various shapes and measuring the relative phase change between 14–20 GHz compared to a reference measurement. The reference cable shape was a loop with the maximum bending radius. The phases were measured with 0.5 GHz steps by a vector network analyser Agilent E8363A. A span of 1 MHz and an averaging factor of 100 were used. Figure 5.6 shows the test results as a function of frequency. A line was fitted to the ‘one bend,  $r=50$  cm’ –data. The deviation of the measured phase from the line is only about  $0.05^\circ$ . This shows that it can be assumed that phase variations in the cable come only from changes in its electrical length. The case of one bend is the most realistic case, and the deviation of  $0.05^\circ$  caused by frequency dispersion is included in Table 5.1 as residual error. The other data sets in Figure 5.6 feature extreme bending which does not occur in real planar scanning with a floating cable. Lines with the same angle as the fitted line have been placed to cross the other data sets at 14.5 GHz. The multiple bends and loops with tight bending radii clearly introduce frequency dispersion which increases the errors in a phase measurement with the proposed system.

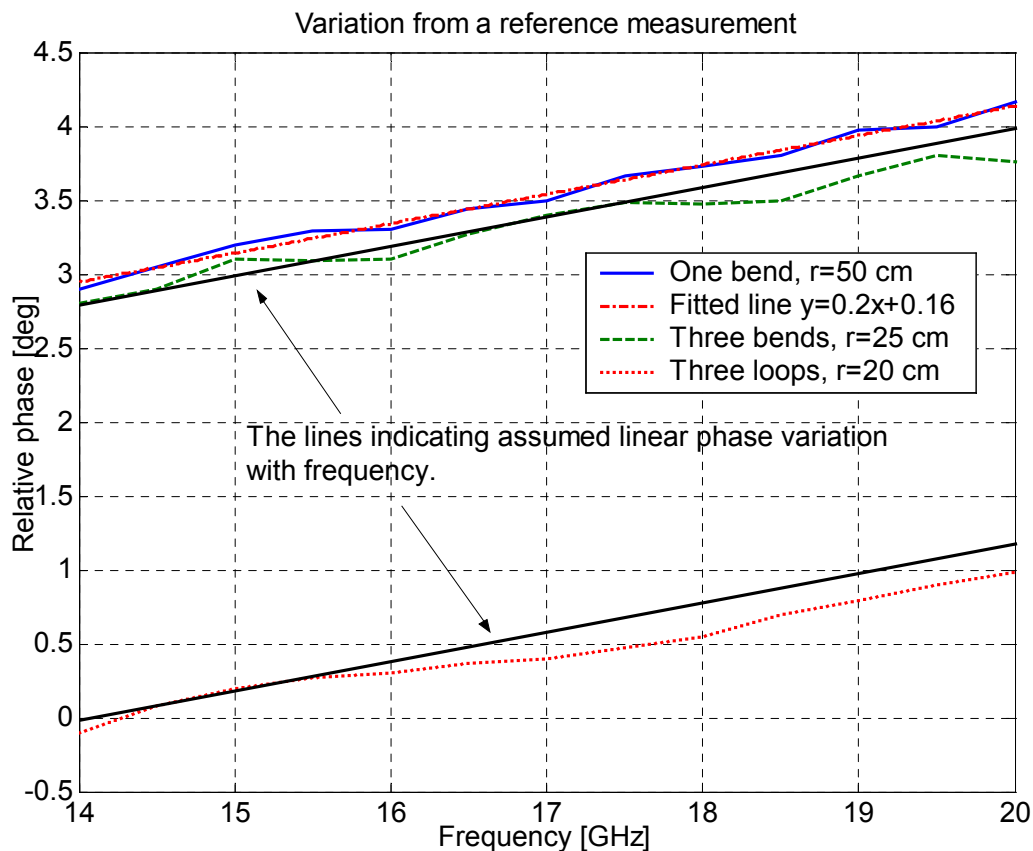


Figure 5.6 Measured phase variations compared to a reference measurement.

### 5.3 Measurement results

The constructed system was applied to quiet-zone field quality testing of a hologram CATR at 310 GHz [P1]. Uncorrected results for the same hologram are presented in [P2]. The phase error surface map shown in Figure 5.7 (frequency-scaled to 310 GHz) was measured across the maximum scanning area of  $80 \times 90 \text{ cm}^2$ . The scanning direction was vertical, starting from grid point (-40, -50).

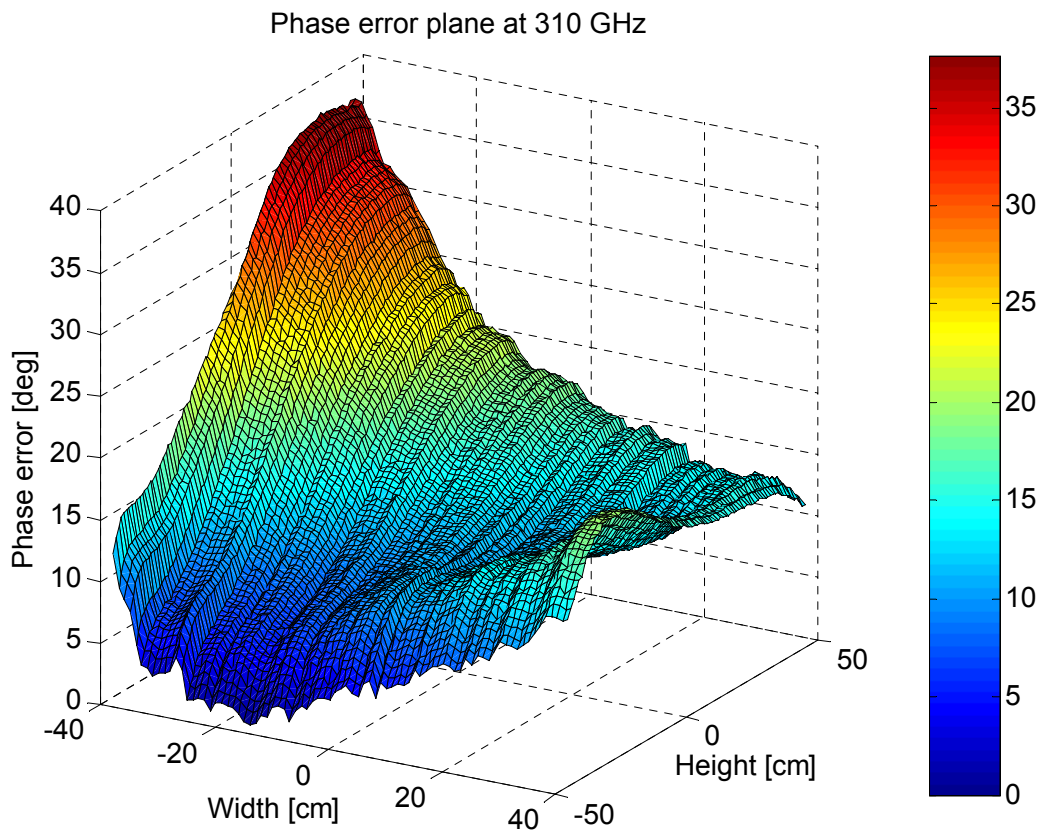


Figure 5.7 The measured phase error surface across the maximum scanning area of  $80 \times 90 \text{ cm}^2$ .

The maximum phase error inside the scanning area is  $38^\circ$ . Figure 5.7 indicates also that the phase error along a single line is nonlinear, and a simple curve fitting is not possible. Without correction of the phase errors caused by cable flexing, the indicated direction of the plane wave in the quiet-zone tests will be tilted in both vertical and horizontal directions from the true direction.

The accuracy of the phase correction was verified by having the transmitter and receiver facing each other on an optical table and by bending the receiver's local oscillator cable while simultaneously measuring the submm-wave signal and the phase correction. In the case of an ideal cable or ideal phase correction, the measured phase should be perfectly flat. The cable was tied to the near-field scanner, and phase variation due to bending over a maximum scanning area of  $50 \times 60 \text{ cm}^2$  was tested. The test setup is shown in Figure 5.8. The cable in this test has two bends while there is only one bend in a real near-field or quiet-zone scan

done with a floating cable. The resulting phase error due to cable flexing should then be doubled to Figure 5.7 which shows the maximum phase error in a real near-field measurement. Further, increased frequency dispersion due to multiple bends may increase the error after phase correction.

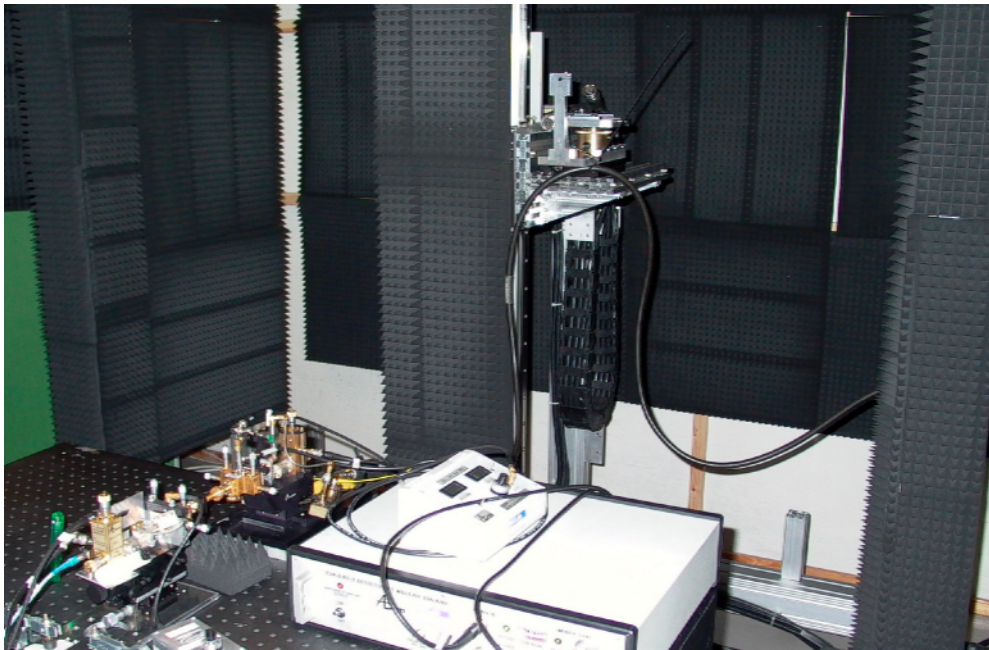


Figure 5.8. Test setup for verification of the phase correction accuracy. Scanner is at the center of the scanning area.

The phase error caused by cable flexing was measured with both horizontal and vertical scanning directions. The results are shown in Figures 5.9–5.10 for horizontal scanning and in Figures 5.11–5.12 for vertical scanning. Sample spacing in the scanning direction was 1 cm and 5 cm in the other direction. The tests were started by zeroing the phase offsets in the phase correction system at the center of the scanning area, i.e. at the grid point (5,30). In every test run, scanning was started from the grid point (-20,0). The maximum phase error due to cable flexing, as indicated by the MVNA system at 310 GHz, with horizontal scanning direction is  $85.3^\circ$  (Figure 5.9). The maximum phase error in the same scan after applying correction is  $4.4^\circ$  (Figure 5.10). With vertical scanning direction, the maximum uncorrected phase error is  $62.4^\circ$  (Figure 5.11), and the maximum phase error after correction is  $4.8^\circ$ . The horizontal and vertical results differ because the cable experiences different bending and torsion in the scanning. Further, it is not possible to measure the phase error plane prior to near-field measurement because the floating cable moves differently each time.

The correction accuracy verification measurements show that the proposed method works well even with multiple cable bends, and the phase errors can be reduced by more than an order of magnitude. The measured correction accuracy of  $5^\circ$  is worse than the expected  $2^\circ$  from Table 5.1, but this is believed to be caused by frequency dispersion and torsion arising with the added second bend to the cable. If appreciable dispersion is present, the assumption that phase variations come only from changes in electrical length, independent of exact frequency, is no longer accurate. In the real near-field scanning measurements, the cable is floating and only one bend is present and correction accuracy will be improved.

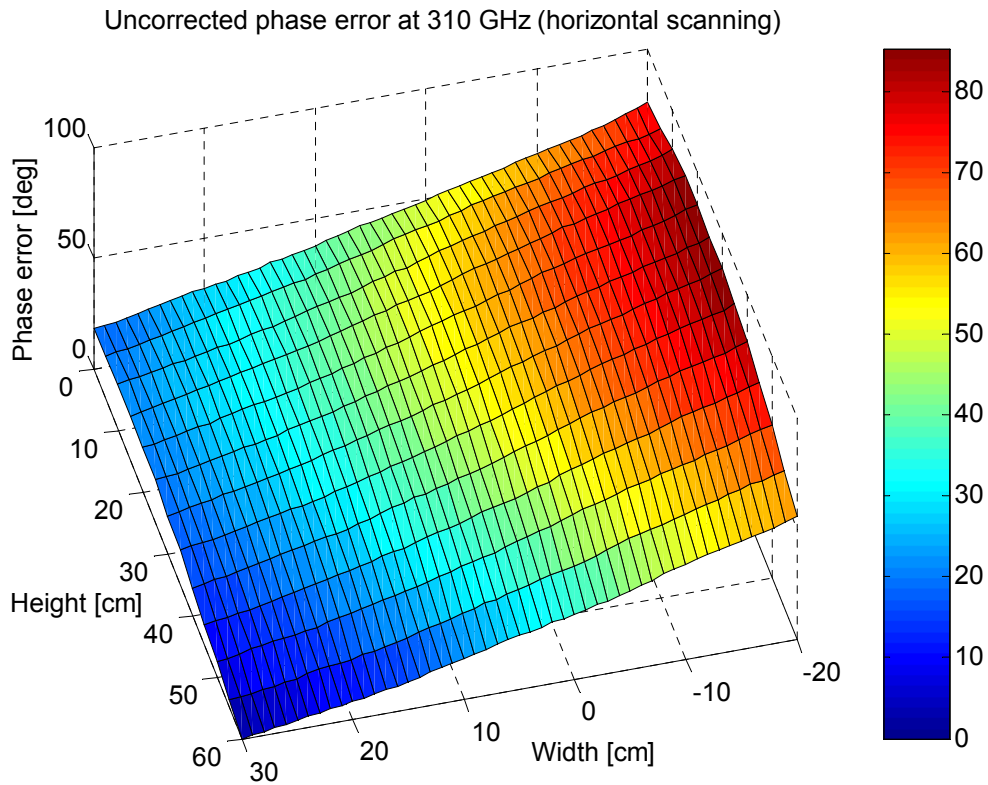


Figure 5.9 Measured (normalised) phase at 310 GHz when the cable is flexed with the near-field scanner. Horizontal scanning direction is used.

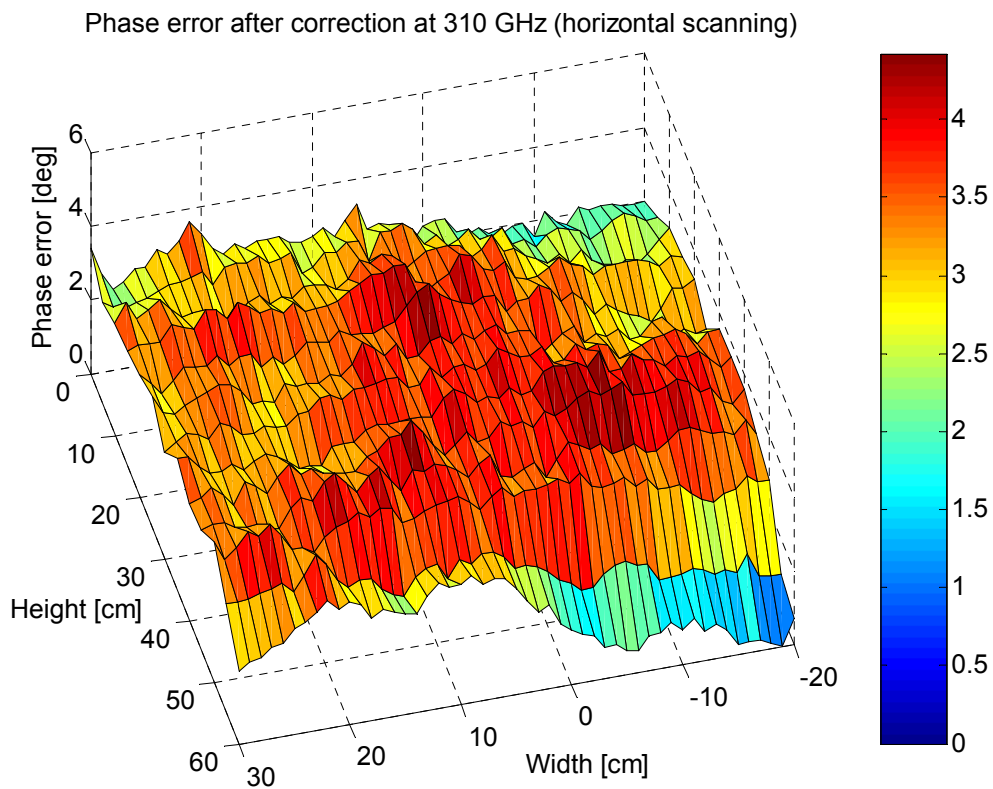


Figure 5.10 Corrected and normalised phase at 310 GHz when the cable is flexed.

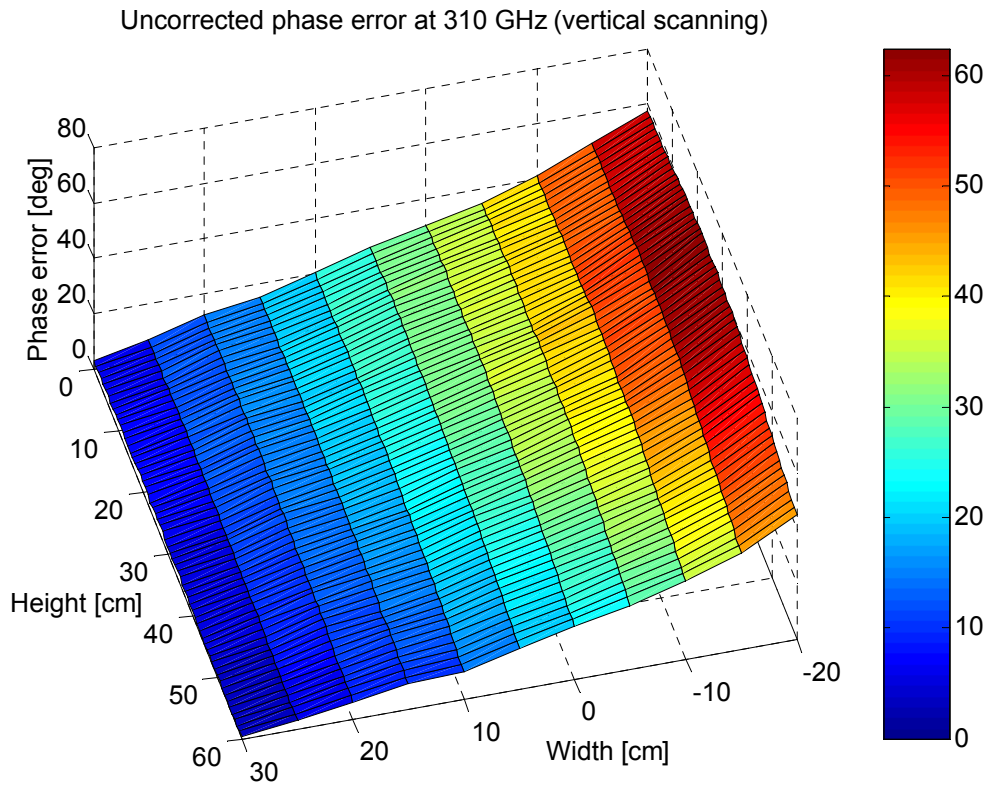


Figure 5.11 Measured (normalised) phase error at 310 GHz when the cable is flexed with the near-field scanner. Vertical scanning direction is used.

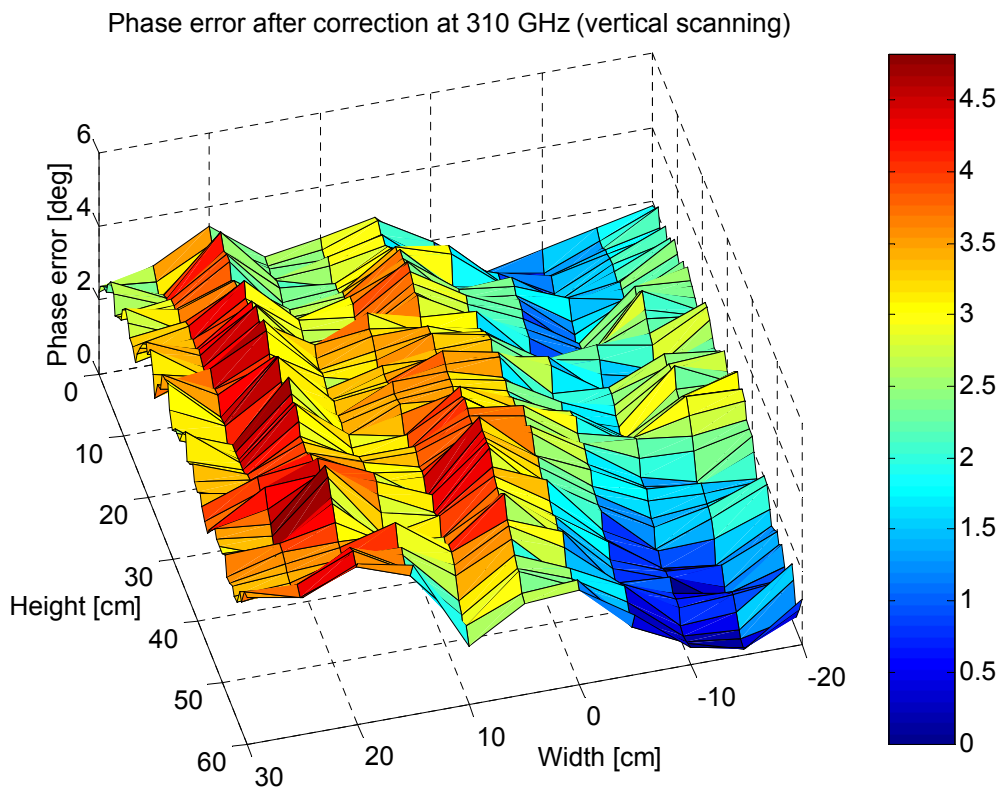


Figure 5.12 Normalised phase error after correction at 310 GHz when the cable is flexed.

## **5.4 Discussion**

The constructed phase correction subsystem works well and does not disturb the operation of neither the MVNA system nor the near-field scanner software. The presented error analysis shows that the expected maximum phase error in a real near-field measurement is about  $2^\circ$ . Phase error plane measurement results were presented for the cases of one and two bends in the local oscillator cable. When only one bend is present, a maximum phase error of  $38^\circ$  was measured. With two bends, the maximum phase error is  $85.3^\circ$  and the corresponding phase correction accuracy is  $5^\circ$ . The  $3^\circ$  increase in inaccuracy compared to the theoretical accuracy is believed to be due to the dispersion caused by the second bend.

For electrically large scan areas, where the measurement can take tens of hours, the amplifiers and other components of the phase correction system should be housed in a temperature controlled cabinet. Ambient temperature stabilisation inside the near-field scanner chamber is also required in order to minimise thermal expansion effects of the scanner frame.

## 6 Absorber materials

### 6.1 Introduction

High-quality absorbers with reflectivities below  $-40$  dB are needed for measurements of low sidelobe antennas with a CATR [2]. The limit is chosen to allow low enough added fields in the quiet-zone region. Testing of some special configurations, like the ESA's Planck Surveyor telescope, may require absorbers with a substantially lower reflectivity. The radiation pattern of the Planck telescope with its solar baffle needs to be measured down to 90 dB below its main lobe, the most demanding requirement being in direction of  $90^\circ$  from the boresight [1]. RAM materials are also used in quasioptical systems as beam dumps and black body calibration sources. The radar cross section (RCS) of military aircrafts and other targets can be reduced by applying suitable RAM sheets in their structures.

The amount of absorbers required for a large-sized range can be hundreds of square meters, so one absorber type should cover the whole intended frequency range. Accurate characterisation of the absorber material must be done prior to procurement. Millimetre wave characterisation results for some typical absorber materials between 100–200 GHz are presented in [72]. Reflectivity levels for three anechoic chambers measured between 100–200 GHz are shown in [73]. Earlier submillimetre wave absorber studies done with various materials are found in [74–78]. Some of these are done on a single frequency [74,77], or only for a single material [75]. The available data in the open literature is incomplete, and it was decided to carry out a study on both the specular and non-specular reflectivities of the commercially available materials.

The purpose of the conducted study, presented in detail in [P6], was to thoroughly characterise a set of suitable absorber materials for use in a large-sized submillimetre wave CATR facility. Overviews of electromagnetic scattering and absorber material design are also given. Furthermore, comparisons with the measured reflectivities in earlier studies with TK THz RAM [77,78] and FIRAM-500 [74,77] are made. The presented scattering results can be used in selecting suitable materials for the test range and as input data for a software that optimises the placement of absorbers inside the range. The material samples have been characterised across the frequency range of 200–600 GHz for specular and 300–400 GHz for non-specular reflectivities. In the bistatic specular reflectivity measurement setup, both the incident and receiving angles are swept continuously. In the bistatic non-specular measurement setup, the receiving angle is continuously swept for three different incident angles.

In the author's view, the published report [P6] is the first publication in the open literature analyzing both the specular and non-specular (bistatic) scattering from a set of materials across a wide frequency range and has continuous angle coverage. An overview of the specular and non-specular scattering measurements is in Sections 6.2 and 6.3.

#### 6.1.1 Tested materials

The full angular scattering performance of several commercially available absorbers (TK THz RAM, TERASORB-500, FIRAM-500, Eccosorb VFX-NRL-2) and some low-cost carpets (Bauhaus wool carpet, Bauhaus floor mat, Etola synthetic carpet 'synthetic grass') have been

measured [P6]. All the tested absorbers are based on different materials. TK THz RAM is made of carbon loaded polypropylene plastic, FIRAM-500 of iron oxide loaded silicon, TERASORB-500 of carbon loaded EVA (ethylene vinyl acetate), and Eccosorb from carbon loaded polyurethane foam. TK THz RAM has a sharp pyramidal surface when FIRAM and TERASORB have a wedged-type surface profile. Eccosorb VFX-NRL-2 is a millimetre wave pyramidal absorber, but only the flat side was tested since the pyramids are too large for obtaining meaningful results with the small test range. The carpet materials were included in the tests because of the earlier encouraging results shown in [74].

## 6.2 Specular scattering measurements at 200–600 GHz

A bistatic test bench was constructed for the specular scattering measurements (Figure 6.1). The distance between the material sample and the receiver/transmitter horns is 7 cm. The measurements were performed between 200–600 GHz with a frequency step of 100 GHz. Angular range of the continuous angle sweep is  $25^{\circ}$ – $70^{\circ}$ .

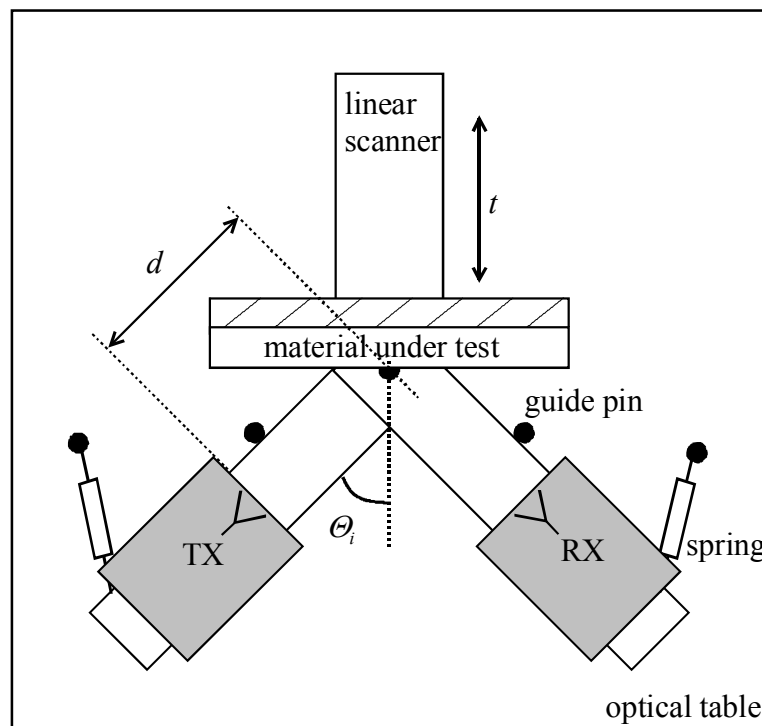


Figure 6.1 Schematic view of the specular scattering test bench [P6].

According to the measurements shown in detail in [P6], there are large variations in reflectivities as a function of the incident angle. TK THz RAM has the lowest specular reflectivity with most of the tested frequencies, being between  $-50$ ...  $-40$  dB in most cases. TERASORB-500 and FIRAM-500 are optimised for 500 GHz and above, and they clearly work better at 500–600 GHz than at 200–400 GHz. The flat side of the Eccosorb VFX-NRL-2 shows large variations in reflectivity due to some internal resonances, and is quite unpredictable in an antenna test range. The carpet materials (except Etola synthetic) have reflectivities below  $-15$  dB in most cases.

### 6.3 Non-specular scattering measurements at 300 and 400 GHz

The bistatic test bench was modified for the non-specular scattering tests to allow continuous receiving angle sweep over  $0^{\circ}$ – $90^{\circ}$  while the incident angle remains fixed (Figure 6.2). Tests were carried out at 300 and 400 GHz with three fixed incident angles of  $26.5^{\circ}$ ,  $45^{\circ}$ , and  $63.4^{\circ}$ . These angles were chosen for mechanical convenience, and they allow a wide receiving angular range to be measured. The maximum receiving angular ranges for the incident angles were  $22.5^{\circ}$ – $90^{\circ}$ ,  $5^{\circ}$ – $90^{\circ}$ , and  $0^{\circ}$ – $90^{\circ}$ , respectively.

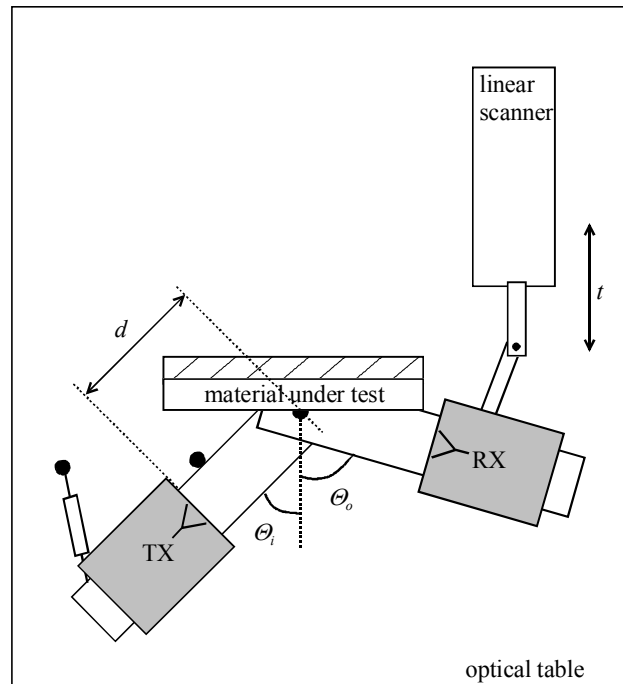


Figure 6.2 Schematic view of the non-specular scattering test bench [P6].

According to the measurements presented in detail in [P6], TERASORB-500 and FIRAM-500 with their grooves horizontal have the best non-specular performance. The performance of these materials is consistent and predictable over the full tested angular range. In most tested cases, TK THz RAM features a sharp dip in scattered power close to the specular direction, and considerably higher lobes around this direction. The angular scattering pattern from TK THz RAM consists of sharp resonant-like minima and maxima. Eccosorb and Bauhaus floor mat have also periodic minima and maxima between  $-15$ ... $-50$  dB in their angular scattering pattern.

### 6.4 Conclusions

It can be concluded from the measurements that TK THz RAM has the best performance in applications where scattering only in the specular direction is of interest. The symmetrical nature of the pyramidal surface also permits operation on both the vertical and the horizontal polarisations without adjusting the absorbers. The findings of [P6] agree with the bistatic work presented earlier in [79] for microwave pyramidal absorbers. The pyramidal absorber

works as an incoherent scatterer and has very wide two-dimensional angular scattering spectrum. The incoherent scattering from the pyramid tips is aggravated by the small size of the individual tiles and difficulties in aligning them with each other. Further, sharp grating peaks are observed in the angular spectrum of TK THz RAM as in [78] when the plane of incidence is parallel to the pyramid needle rows. The grating effect can be minimised by rotating the absorber around its surface normal.

TERASORB-500 and FIRAM-500 are the best if only one polarisation is used, and the scattered power into the surroundings should be minimised. The selection between the two materials should be done according to the needed RAM size, as in general they are equal in performance. The material panels can be rotated and tilted according to the used polarisation and the range geometry in order to provide scattering minima in the directions of most interest. Modeling and measurements of bistatic scattering from wedge absorbers at microwave frequencies are reported in [80]. The wedge absorber works as a coherent scatterer and has a clearly defined one-dimensional scattering pattern around the specular direction, which drops off rapidly when moving to higher/lower angles. Similar effect is observed and reported in [P6].

Eccosorb VFX-NRL-2 with its large pyramids is likely to perform better than the flat side included in these tests by increasing the number of reflections. The low cost carpet materials with their better than  $-15$  dB reflectivity can be used to reduce backscatter in a large antenna test range.

The results shown in [P6] were measured in the near-field of the scattering materials, and although it was shown by varying the measurement distance that there are no rapidly changing fields present, the true far-field patterns of the materials can be somewhat different. For example, the true far-field patterns would show more well-defined diffraction peaks at certain angles. However, the measured total scattered power from the materials is the same for both near-field and far-field tests, so the presented results are useful in comparing the materials.

## 7 Compact antenna test range design

### 7.1 Testing environment for submm-wave CATRs

The atmospheric gases, and especially water vapour are significant sources of signal attenuation in mm- and submm-wave antenna test ranges. Water vapour has several attenuation bands between 30–1000 GHz [2]. The strong attenuation in these bands is caused by excitation of certain molecular rotational modes. The bands are centered around the molecular resonance frequencies of water and their widths are determined by the total air pressure. The integrated band strengths are determined by the water vapour concentration in the air. Other major atmospheric gases include nitrogen, carbon dioxide, and oxygen. Nitrogen and carbon dioxide do not directly attenuate THz signals, but oxygen has several absorption bands in the THz range. However, oxygen-related absorption is much weaker than the water vapour absorption. All gas molecules in the air add to the total air pressure and thus contribute to the widening of the absorption bands.

Another problem related to atmospheric water vapour is the variation of the phase-delay of a signal beam in time or in space [2]. In a CATR facility, the variations of phase-delay in time do not have significant effect on the measurement of antenna power pattern. Instead, spatial variations in the refractive index of air can distort the measurement by spoiling the planarity of the plane-wave phase-front in the quiet-zone. This effect is minimised by keeping the water vapour concentration inside the antenna range as low as possible.

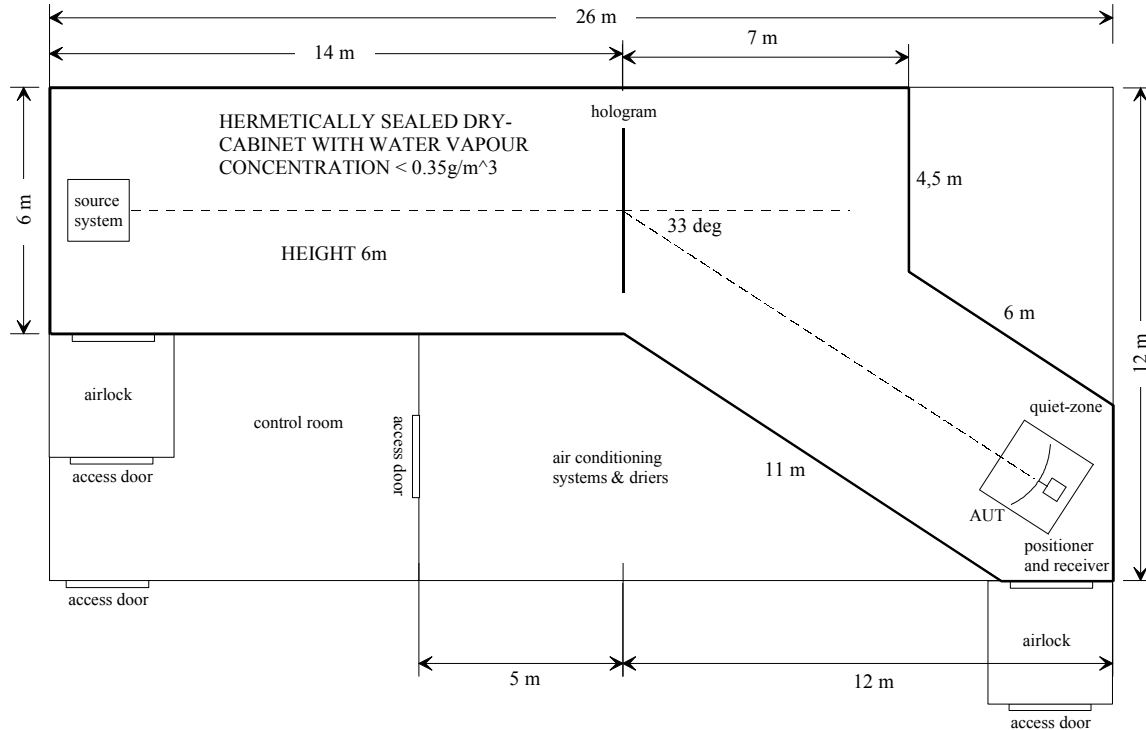


Figure 7.1 Layout of the hologram CATR with 2.5 meter quiet-zone [O6].

A perfect vacuum inside the test chamber would be the best alternative, but the large size of the chamber makes it impossible. The most cost effective way to reduce the attenuation to an

acceptable level of 1 dB/10 m [2] is to lower the water vapour concentration by using circulating-air driers inside a hermetically sealed chamber. This means a relative humidity of 2% ( $0.35 \text{ g/m}^3$ ) when the temperature is 293 K and the atmospheric pressure 1013 mbar. One possible design for a hologram CATR inside a sealed dry-cabinet is shown in Figure 7.1 [O6]. The volume of the enclosure is about  $1000 \text{ m}^3$ . According to an inquiry from Bassaire Ltd in the UK, the cost of such a chamber with the airlocks and driers would be hundreds of thousands of euros (dollars).

## 7.2 Instrumentation

The large CATR facility needs positioners for the source system and for the AUT. The source positioner should have motor controls in the  $x$ ,  $y$ , and  $z$ -axes for precise adjustment of the feed horn position. The heavy-duty AUT positioner needs to be able to move precisely loads of over 300 kg, and it should have both azimuth and elevation axis controls. A movable accurate near-field scanner is needed for the initial and periodical quiet-zone verification procedures.

A heavy-duty antenna positioner was constructed during year 2002 by HUT Laboratory of Machine Design for MilliLab. The positioner was modified from a Bofors air defense gun by removing the weapon systems and mounting a 2 meter wide elevation cradle built from steel profile over the azimuth table. AC drives with gearboxes are used to move the axes. 26-bit absolute angle encoders were fitted in both azimuth and elevation axes, and give an angle readout accuracy of  $0.0001^\circ$ . A near-field scanner, mountable inside the elevation cradle for quiet-zone quality verification, is being constructed at the time of writing. The windmill-type scanner will consist of a single 2 m long linear stage that can be accurately mounted in vertical, horizontal, and diagonal directions. The positioner and scanner will be used to test the ESA ADMIRALS antenna by using a hologram CATR at 322 GHz [P3].

The MVNA vector network analyser described in Chapter 3 of this thesis can be used as the measurement controller. Depending on the frequency band and the required dynamic range, a BWO or a frequency-multiplied Gunn oscillator can be used as the source. The Gunn-source ABmm ESA-1 was discussed earlier in Section 3.2.1 and the BWO in Sections 4.4–4.5. A sensitive receiver is needed for ensuring high dynamic range. One alternative is the ABmm ESA-2 receiver introduced in Section 3.3.1. A more sensitive 5<sup>th</sup> harmonic mixer operating between 600–700 GHz has been designed and constructed in the HUT Radio Laboratory for use with the BWO-PLL system. It can also be used as the antenna measurement receiver.

## 8 Summary of publications

Paper [P1] presents the developed system for measurement and correction of the phase errors caused by cable flexing in submillimetre wave near-field antenna testing. Antenna testing with planar near-field scanning and testing of the quiet-zone of the compact antenna test range (CATR) require moving receivers with cables attached to them. The receiver uses harmonic mixing, and phase changes in its local oscillator cable get multiplied and added to the detected phase. The novel system described in this paper is based on the use of a pilot signal to continuously measure changes in the phase response of the cable. The error analyses in [P1] and in Section 5.2.3 of this thesis show that correction of the cable flexing related phase errors is possible down to a level of  $2^\circ$  at 310 GHz.

Paper [P2] presents the quiet-zone field quality measurement results for the first submillimetre wave hologram CATR operating at 310 GHz. The results show the applicability of the hologram CATR for submm wavelengths and that the manufacturing of the hologram by conventional PCB lithography was successful. The measured peak-to-peak amplitude and phase ripples are 1.0 dB and  $10^\circ$ , respectively. The design of the 60 cm hologram is described in detail in [O1] and the manufacturing in [O2]. The cross-polarisation results for this hologram are presented in [P4].

Paper [P3] discusses the applications of the hologram CATR for testing of satellite antennas and the ongoing and future developments. The main beam measurement results for the Swedish Odin spacecraft are presented in this paper and in [27]. The ongoing development and preliminary design of a hologram CATR suitable for measuring antennas in the 1.5 meter class at 322 GHz are shown. Also a design for a demonstrator CATR at 650 GHz is discussed. The relative quiet-zone size of a hologram CATR can be extended by using a dual reflector feed system (DRFS) to provide modified illumination. The simulated improvement in quiet-zone size over the conventional feed horn illumination is also presented in this paper.

Paper [P4] presents a numerical method for predicting the cross-polarisation level produced by a hologram. The method takes into account the whole hologram structure with curved slots. Cross-polarisation produced by a hologram has been measured at 39 GHz and at 310 GHz, showing good correlation between the predicted and measured levels. The maximum measured cross-polarisation level inside the quiet-zone is about  $-20$  dB.

Paper [P5] describes the constructed system for phase-locking of submillimetre wave backward-wave oscillators (BWO) and associating them with a millimetre wave vector network analyser (MVNA). The obtainable improvement in the dynamic range compared to the standard solid-state source by using the phase-locked BWO source is also given. The PLL system can be used for phase-locking BWOs in the frequency range of 180–714 GHz. The measured improvement in dynamic range between 300–400 GHz by using the BWO is 16–20 dB. The estimated improvement at 700 GHz, based on the power level difference between the standard source and the BWO, is close to 40 dB.

Paper [P6] discusses the results of the reflectivity measurements performed between 200–600 GHz for several commercially available absorber samples and carpet materials. Measurements of both specular and non-specular scattering from several submillimetre wave absorber materials and low-cost carpet materials are presented. The carpets were included in the tests because some earlier publications noted that they can be used in non-critical areas to reduce

material cost. The frequency range in specular scattering is 200–600 GHz, and 300–400 GHz in non-specular scattering measurements. The constructed bistatic test bench allows automatic testing over the full continuous angular range of  $0^{\circ}$ – $90^{\circ}$ . The measurement results show large differences in performance between materials. The best specular performance of  $-50$  dB was measured for the pyramidal TK THz RAM. However, the same material scatters considerable amounts of power into non-specular angles. The scattered power from wedged-type TERASORB-500 and FIRAM-500 materials is concentrated close to the specular direction, and very little power is found at other angles if the wedges are properly oriented. Low-cost carpet materials have better than  $-15$  dB reflectivities in most angles, and are very useful in the non-critical areas of the antenna range. The results presented in [P6] can be used to optimise the absorber placement inside the antenna range, concerning both maximum performance and lowest cost.

## 9 Discussion and conclusions

Several scientific satellites carrying submillimetre wave instrumentation and antennas will be launched within the next ten years. The spacecraft antenna assemblies need to be verified before launch, which is problematic with the presently available antenna test ranges. The compact antenna test range (CATR) and the near-field scanning methods are commonly seen as the best alternatives. The commonly used reflector CATR has some disadvantages at high frequencies, the most severe being the required high surface accuracy. The phase and amplitude ripples caused by the surface inaccuracies limit the operating range of large reflectors to about 200 GHz [3]. Accurately milled large reflectors are also extremely expensive. Advantages of reflector CATRs include their wide operating bandwidth (limited at low end by edge diffraction and surface inaccuracy at high end), low coupling losses, and low cross-polarisation level compared to the hologram CATR. A method based on modeling the reflector surface inaccuracies and calculating them out of the antenna measurements has been proposed, but no real pattern comparison data is available in public [4]. The near-field scanning systems have been used for main beam testing at frequencies up to 650 GHz [6]. The problems associated with high frequency near-field systems are the required extreme accuracy of the field sampling plane (planarity with planar scanners), the large amount of data points, and the long measurement time. Radiation pattern measurements over full solid angle are also not possible with near-field tests. A CATR based on a hologram is a possible alternative to reflector CATRs, as the surface accuracy demand of the hologram is not so stringent [5]. The manufacturing cost of a hologram is potentially much smaller than that of a reflector. However, the transmission loss of an amplitude hologram is relatively high (15...20 dB), it operates only on a single linear polarisation, and is narrowband (5–10%). Further, the cross-polarisation level of –20 dB may limit its usability for testing communication antennas.

This thesis presents the developed instrumentation and measurement techniques for testing of submillimetre wave CATRs. The developed techniques can also be applied to improve the accuracy of planar near-field scanning systems. In this thesis, the applicability of the hologram CATR for submillimetre wavelengths has been demonstrated. The dynamic range of a commercial vector network analyser can be extended by using a powerful backward-wave oscillator (BWO) as the source. A phase-locking system for 180–714 GHz BWOs has been developed in this thesis. The obtainable improvement in measurement dynamic range over a standard source configuration based on a frequency multiplied Gunn oscillator is 16–40 dB over the frequency range of 300–700 GHz.

The phase measurement accuracy of the near-field scanning system used in measuring the quiet-zone field quality of a hologram CATR has been improved by introducing a new-type of phase error measurement subsystem. The phase error measurement and correction system is based on the use of a pilot signal to detect changes in the phase response (electrical length) of a microwave coaxial cable. The error analysis shows that cable flexing related phase errors can be corrected down to a level of 2°. The accuracy of the phase correction system has also been verified by measurements, and an improvement of more than an order of magnitude to the phase measurement accuracy with a moving cable is possible.

The specular and non-specular scattering properties of several commercially available absorber materials and floor carpets between 200–600 GHz have been measured. According to the measurements, there are large variations in reflectivities as a function of the incident angle. The pyramidal absorber TK THz RAM, with its better than –40 dB specular reflectivity

in most angles, is best suited for reducing specular reflection. The wedged absorbers FIRAM-500 and TERASORB-500 have the lowest scattering into non-specular directions. One must be careful in aligning the absorbers to the incident angle and polarisation, so that the grating effects are minimised. In a CATR facility, different types of absorbers can be mixed to have the lowest overall scattered power at the quiet-zone volume. The floor carpet materials with their  $-15$  dB reflectivity can be used in the non-critical areas to reduce backscatter.

Also in this thesis, a complete hologram CATR facility suitable for 300–1000 GHz is studied. The problems associated with atmospheric water vapour are emphasized, and an air-drying system is proposed for the facility. The facility needs also large quantities of high performance absorber material.

The future work regarding the hologram CATR include manufacturing of a  $3 \times 3$  m<sup>2</sup> hologram for testing of a 1.5 meter class dish antenna (ESA ADMIRALS) and construction of a 1 m<sup>2</sup> demonstrator CATR for 650 GHz. The manufacturing of accurate slot patterns over large areas is problematic, and direct laser exposing and wet etching are used. The pattern accuracy with this method is about  $5 \mu\text{m}$  and the minimum etched linewidth about  $30 \mu\text{m}$ .

A modified illumination for the hologram using a dual reflector feed system (DRFS) has been simulated to give an increase of close to 15% to the quiet-zone/hologram size ratio [P3,O25]. The DRFS provides amplitude tapered illumination to the hologram. So far, the tapering has been done by narrowing the hologram slots at the edges which creates manufacturing difficulties due to the required narrow slot widths. The DRFS has been manufactured and testing is still ongoing at the time of writing. The initial beam pattern tests at 310 GHz show that manufacturing and the reflector positioning has been successful despite the tight tolerances. The system will be applied to hologram CATR design in the near future.

A new subject of study is the phase hologram [O15,O34]. It can be manufactured on a dielectric substrate by machining grooves on its surface that act as a diffraction grating. Suitable substrate materials include teflon and rexolite. The local groove widths and depths are optimized by a specially developed software package using rigorous electromagnetic diffraction theory. Also, FDTD based simulation methods for phase holograms are being developed. The phase hologram can achieve a much better efficiency compared to the amplitude hologram (transmission loss of ca. 4 dB compared to 15...20 dB), and it can be used to provide an accurate plane wave with amplitude and phase ripples of  $\pm 0.5$  dB and  $\pm 5^\circ$ , e.g., for CATR and RCS applications.

As the final conclusion of this thesis, the following was achieved:

- 1) The feasibility of the compact antenna test range based on an amplitude hologram has been demonstrated in the submm-wave region.
- 2) A pilot signal based phase error correction system for flexing cables in near-field scanning measurements has been developed and presented.
- 3) The full angular scattering performance of several commercial absorbers has been measured and presented. The tests include both the specular and non-specular scattering.

- 4) The use of a phase-locked BWO to extend the dynamic range of commercial vector network analyser in the submm-wave region has been presented and published for the first time.



## References

- [O1] J. Ala-Laurinaho, J. Säily, J. Häkli, J. Tuovinen, A. Lehto, A.V. Räsänen, "Design of a 310 GHz Hologram Compact Antenna Test Range", *Proceedings of the 22<sup>nd</sup> ESTEC Antenna Workshop on Antenna Measurements*, WPP-164, ESTEC, Noordwijk, The Netherlands, May 11-12, 1999, pp. 159–162
- [O2] J. Säily, J. Ala-Laurinaho, J. Häkli, J. Tuovinen, A. Lehto, A.V. Räsänen, "Development of a 310 GHz Hologram Compact Antenna Test Range", *Proceedings of the 21<sup>st</sup> Annual Meeting & Symposium of the Antenna Measurement Techniques Association (AMTA)*, Monterey Bay, CA., USA, Oct. 4-7, 1999, pp. 464–469
- [O3] J. Häkli, J. Ala-Laurinaho, J. Säily, J. Tuovinen, A. Lehto, A.V. Räsänen, "Hologram compact test range for submillimetre-wave region", *URSI/IEEE XXIV National Convention on Radio Science*, Tuorla Observatory Reports, Informo No. 181, Turku, 1999, pp. 34–35
- [O4] A.V. Räsänen, J. Ala-Laurinaho, J. Säily, J. Häkli, "Millimeter and submillimeter wave antenna testing with a hologram CATR" (invited paper), *Proceedings of the COST-712 Workshop on Techniques and Facilities in the mm and submm Range for Atmospheric Research*, Bern, Switzerland, December 9-10, 1999, pp. 104–111
- [O5] J. Tuovinen, J. Ala-Laurinaho, J. Säily, J. Häkli, A. Lehto, A.V. Räsänen, "Hologram - Modern Optics for Millimetre and Submillimetre Wave Antenna Testing", *Proceedings of the AP-2000 Conference*, Davos, Switzerland, Apr. 9-14, 2000, CD-ROM
- [O6] J. Säily, J. Ala-Laurinaho, J. Häkli, J. Tuovinen, A. Lehto, A.V. Räsänen, "Instrumentation and testing of submillimeter wave compact antenna test ranges", *Proceedings of the 11<sup>th</sup> International Symposium on Space Terahertz Technology*, Ann Arbor, MI., USA, May 1-3, 2000, pp. 590–597
- [O7] J. Ala-Laurinaho, J. Häkli, A. Lehto, P. Piironen, A.V. Räsänen, J. Säily, J. Tuovinen, "Submillimetre wave antenna testing using a hologram CATR", *Abstract, Summary Report and Task Reports*, ESTEC Contract No. 13096/98/NL/SB, June 2000, 92 p.
- [O8] J. Säily, J. Mallat, A.V. Räsänen, "Development of a phase-locking system for submillimetre wave backward-wave oscillators", *Abstracts of the URSI XXV National Convention on Radio Science*, FMI Reports 2000:5, Helsinki, Sept. 21-22, 2000, pp. 64–65
- [O9] J. Säily, J. Mallat, A.V. Räsänen, "Reflectivity measurements of several commercial absorbers in the 200–600 GHz range", *Electronics Letters*, Vol. 37, No. 3, 2001, pp. 143–145
- [O10] J. Salo, J. Meltaus, E. Noponen, J. Westerholm, M.M. Salomaa, A. Lönnqvist, J. Säily, J. Häkli, J. Ala-Laurinaho, A.V. Räsänen, "Millimeter-wave Bessel beams using computer holograms", *Electronics Letters*, Vol. 37, No. 13, 2001, pp. 834–835

- [O11] J. Säily, J. Mallat, A.V. Räisänen, "Reflectivity measurements of commercial absorbers in the 200–600 GHz range", *Proceedings of the 12<sup>th</sup> International Symposium on Space Terahertz Technology*, San Diego, CA., USA, Feb. 14-16, 2001, pp. 383–389
- [O12] J. Häkli, J. Säily, J. Ala-Laurinaho, T. Koskinen, A. Lönnqvist, A. Lehto, J. Tuovinen, A.V. Räisänen, "Development of a hologram CATR for submm-wavelengths", *Proceedings of the 12<sup>th</sup> International Symposium on Space Terahertz Technology*, San Diego, CA., USA, Feb. 14-16, 2001, pp. 390–399
- [O13] A.V. Räisänen, J. Ala-Laurinaho, J. Säily, J. Häkli, T. Koskinen, A. Lönnqvist, J. Tuovinen, "Radio hologram CATR – a feasible method for FIRST/Herschel Space Observatory antenna testing?", *Proceedings of the Submillimeter Astronomy Science Workshop for the Herschel Space Observatory/Far Infrared and Submillimeter Telescope (FIRST)*, San Diego, CA., USA, Feb. 11-13, 2001, in press
- [O14] A.V. Räisänen, J. Ala-Laurinaho, J. Säily, J. Häkli, T. Koskinen, A. Lönnqvist, E. Noponen, J. Salo, J. Meltaus, J. Westerholm, M.M. Salomaa, "Experimental studies on radio holograms at mm- and submm-wavelengths" (invited paper), *MSMW'2001 Proceedings*, Kharkov, Ukraine, June 4-9, 2001, pp. 57–62
- [O15] J. Salo, J. Meltaus, E. Noponen, J. Westerholm, M.M. Salomaa, A. Lönnqvist, J. Säily, J. Häkli, J. Ala-Laurinaho, J. Mallat, A.V. Räisänen, "Generation of millimeter-wave Bessel beams using amplitude and phase holograms", European Optical Society, topical meeting, *Electromagnetic Optics 2*, Paris, France, August 26–30, 2001, p. 57
- [O16] P. Eskelinen, J. Säily, "Phase stability tests with a millimeter wave network analyzer", *Proceedings of the 31<sup>st</sup> European Microwave Conference*, London, UK, Sept. 25-27, 2001, pp. 411–414
- [O17] A.V. Räisänen, J. Ala-Laurinaho, J. Säily, J. Häkli, T. Koskinen, A. Lönnqvist, V. Viikari, J. Mallat, E. Noponen, J. Salo, J. Meltaus, M. Weber, M.M. Salomaa, "Computer generated holograms for mm- and submm-wave applications: CATR, Bessel beams and radiowave vortices" (invited paper), *Proceedings of the 9<sup>th</sup> International Conference on Terahertz Electronics*, Charlottesville, VA., USA, Oct. 15–16, 2001
- [O18] J. Säily, P. Eskelinen, A.V. Räisänen, "Measurement and correction of the phase errors introduced by flexible cables in submm-wave planar near-field testing", *Proceedings of the 23<sup>rd</sup> Annual Meeting & Symposium of the Antenna Measurement Techniques Association (AMTA)*, Denver, CO., USA, Oct. 21-26, 2001, pp. 78–83
- [O19] J. Säily, J. Mallat, A.V. Räisänen, "Reflectivity measurements of various commercial absorbers in the 200–600 GHz", *Proceedings of the 23<sup>rd</sup> Annual Meeting & Symposium of the Antenna Measurement Techniques Association (AMTA)*, Denver, CO., USA, Oct. 21-26, 2001, pp. 294–298
- [O20] T. Koskinen, J. Ala-Laurinaho, J. Säily, J. Häkli, A. Lönnqvist, A.V. Räisänen, J. Tuovinen, "Analysis of an RF hologram for CATR", *Digest of the URSI XXVI*

- Convention on Radio Science and 2<sup>nd</sup> Finnish Wireless Communications Workshop*, Tampere, Oct. 23–24, 2001, pp. 99–100
- [O21] A. Lönnqvist, J. Ala-Laurinaho, J. Häkli, T. Koskinen, V. Viikari, J. Säily, J. Tuovinen, A.V. Räsänen, "Effects of hologram joints to the quiet-zone field in a CATR", *Digest of the URSI XXVI Convention on Radio Science and 2<sup>nd</sup> Finnish Wireless Communications Workshop*, Tampere, Oct. 23–24, 2001, pp. 101–102
- [O22] J. Häkli, T. Koskinen, J. Ala-Laurinaho, J. Säily, A. Lönnqvist, J. Tuovinen, A.V. Räsänen, "Development of a dual reflector feed system for hologram compact antenna test range", *Digest of the URSI XXVI Convention on Radio Science and 2<sup>nd</sup> Finnish Wireless Communications Workshop*, Tampere, Oct. 23–24, 2001, pp. 103–104
- [O23] P. Eskelinen, J. Säily, "Frequency and phase stability in a millimeter wave network analyzer", *Proceedings of the XVI European Time and Frequency Forum*, St. Petersburg, Russia, Mar. 12–14, 2002
- [O24] J. Salo, J. Meltaus, E. Nojonen, M. M. Salomaa, A. Lönnqvist, T. Koskinen, V. Viikari, J. Säily, J. Häkli, J. Ala-Laurinaho, J. Mallat, and A. V. Räsänen, "Holograms for shaping radio-wave fields", *Journal of Optics A: Pure and Applied Optics*, No. 4, Aug. 2002, pp. 161–167
- [O25] J. Häkli, T. Koskinen, J. Ala-Laurinaho, J. Säily, A. Lönnqvist, J. Mallat, J. Tuovinen, A. V. Räsänen, "A dual reflector feed system for a sub-mm hologram CATR", *the Proceedings of the 13<sup>th</sup> International Symposium on Space Terahertz Technology*, Cambridge, MA., USA, March 26–28, 2002, pp. 327–336
- [O26] T. Koskinen, J. Ala-Laurinaho, J. Säily, J. Häkli, A. Lönnqvist, J. Mallat, J. Tuovinen, A. V. Räsänen, "On the design of sub-mm wave amplitude holograms for CATR", *the Proceedings of the 13<sup>th</sup> International Symposium on Space Terahertz Technology*, Cambridge, MA., USA, March 26–28, 2002, pp. 537–543
- [O27] J. Meltaus, J. Salo, E. Nojonen, M.M. Salomaa, A. Lönnqvist, T. Koskinen, J. Säily, J. Häkli, J. Ala-Laurinaho, J. Mallat, A.V. Räsänen, "Holograms for shaping radio-wave fields", *Digest of 2002 IEEE MTT-S International Microwave Symposium*, Seattle, Washington, June 3–7, 2002, Vol. 2, pp. 1305–308
- [O28] A. Lönnqvist, J. Ala-Laurinaho, J. Häkli, T. Koskinen, V. Viikari, J. Säily, J. Mallat, J. Tuovinen, A.V. Räsänen, "Manufacturing of large-sized amplitude holograms for a submm-wave CATR", *Digest of 2002 IEEE Antennas and Propagation Society International Symposium*, San Antonio, Texas, USA, June 16–21, 2002, Vol. 4, pp. 394–397
- [O29] J. Häkli, J. Ala-Laurinaho, T. Koskinen, J. Säily, A. Lönnqvist, J. Mallat, J. Tuovinen, A. V. Räsänen, "Synthesis of a dual reflector feed system for a hologram CATR", *Digest of 2002 IEEE Antennas and Propagation Society International Symposium*, San Antonio, Texas, USA, June 16–21, 2002, Vol. 4, pp. 580–583

- [O30] J. Säily, P. Eskelinen, "Improving the frequency and phase stability of a commercial millimeter wave vector network analyzer", *Digest of the URSI General Assembly 2002*, Maastricht, The Netherlands, Aug. 17–24, 2002
- [O31] T. Koskinen, J. Häkli, J. Säily, A. Lönnqvist, J. Ala-Laurinaho, J. Mallat, J. Tuovinen, A.V. Räisänen, "Hologram CATRs for 322 GHz and 650 GHz: A progress report", *Proceedings of the 25<sup>th</sup> ESA Antenna Workshop on Satellite Antenna Technology*, ESTEC, Noordwijk, The Netherlands, September 18–20, 2002, pp. 165–171
- [O32] A.V. Räisänen, J. Meltaus, J. Salo, T. Koskinen, A. Lönnqvist, J. Häkli, J. Säily, J. Ala-Laurinaho, J. Mallat, E. Noponen, M.M. Salomaa, "Computer-generated holograms for mm- and submm-wave beam shaping", *Proceedings of the IRMMW2002*, San Diego, CA., USA, in press
- [O33] T. Koskinen, A. Lönnqvist, J. Häkli, J. Säily, J. Ala-Laurinaho, J. Mallat, J. Tuovinen, A.V. Räisänen, "Development of hologram CATRs for 322 and 650 GHz", *Digest of the URSI/IEEE XXVII Convention on Radio Science*, Espoo, Oct. 17–18, 2002, pp. 140–142
- [O34] J. Mallat, J. Ala-Laurinaho, E. Noponen, V. Viikari, A. Lönnqvist, T. Koskinen, J. Säily, J. Häkli, J. Meltaus, A.V. Räisänen, "A phase hologram RCS range for scale model measurements", *Digest of the URSI/IEEE XXVII Convention on Radio Science*, Espoo, Oct. 17–18, 2002, pp. 143–145
- [O35] J. Säily, J. Mallat, P. Eskelinen, A.V. Räisänen, "Specular and non-specular scattering studies of radar absorbing materials at 200–600 GHz", *Digest of the URSI/IEEE XXVII Convention on Radio Science*, Espoo, Oct. 17–18, 2002, pp. 156–158
- [O36] P. Eskelinen, J. Säily, "A measuring system for millimeter wave backscattering", *Digest of the URSI/IEEE XXVII Convention on Radio Science*, Espoo, Oct. 17–18, 2002, pp. 167–169
- [O37] J. Meltaus, J. Salo, E. Noponen, M. M. Salomaa, V. Viikari, A. Lönnqvist, T. Koskinen, J. Säily, J. Häkli, J. Ala-Laurinaho, J. Mallat, and A. V. Räisänen, "Radio-wave beam shaping using holograms", *IEEE Transactions on Microwave Theory and Techniques*, Vol. 51, Apr. 2003, pp. 1274–1280
- [O38] A. Lönnqvist, J. Mallat, E. Noponen, J. Ala-Laurinaho, J. Säily, T. Koskinen, J. Häkli, A. V. Räisänen, "A Phase Hologram Compact RCS Range for Scale Model Measurements", *Proceedings of 3<sup>rd</sup> ESA Workshop on Millimetre Wave Technology and Applications*, WPP-212, Espoo, Finland, 21-23 May 2003, pp. 511-516.
- [O39] J. Häkli, T. Koskinen, A. Lönnqvist, J. Ala-Laurinaho, J. Mallat, J. Säily, J. Tuovinen, A. V. Räisänen, J. Lemanczyk, "Dual Reflector Feed System for Sub-mm Wave Region Hologram CATR", *Proceedings of 3<sup>rd</sup> ESA Workshop on Millimetre Wave Technology and Applications*, WPP-212, Espoo, Finland, 21-23 May 2003, pp. 353-358.
- [O40] J. Ala-Laurinaho, J. Säily, T. Koskinen, J. Häkli, A. Lönnqvist, J. Mallat, J. Tuovinen, A. V. Räisänen, J. Lemanczyk, "Preparations for Testing the ADMIRALS RTO in an

- Ad Hoc CATR Based on a Hologram”, *Proceedings of 3<sup>rd</sup> ESA Workshop on Millimetre Wave Technology and Applications*, WPP-212, Espoo, Finland, 21-23 May 2003, pp. 389-394.
- [O41] J. Häkli, J. Mallat, J. Säily, J. Ala-Laurinaho, A. Lönnqvist, T. Koskinen, A. V. Räisänen, "Improving the Measurement Accuracy of a Planar Near-Field Scanner for Submillimetre Wave Antenna Testing”, *Proceedings of 3<sup>rd</sup> ESA Workshop on Millimetre Wave Technology and Applications*, WPP-212, Espoo, Finland, 21-23 May 2003, pp. 399-405.
- [O42] J. Säily, A.V. Räisänen, “Scattering studies from radar absorbing materials (RAM) at 200–600 GHz”, *Proceedings of 3<sup>rd</sup> ESA Workshop on Millimetre Wave Technology and Applications*, WPP-212, Espoo, Finland, 21-23 May 2003, pp. 453–458.
- [O43] T. Koskinen, J. Mallat, A. Lönnqvist, J. Säily, J. Häkli, J. Ala-Laurinaho, J. Tuovinen, A.V. Räisänen, “Performance of a Small 650 GHz Hologram”, *Digest of the 2003 IEEE International Symposium on Antennas and Propagation*, Columbus, OH, USA, June 22-27, 2003, Vol. 3, pp. 532–535
- [1] P. de Maagt, G. Crone, “(Sub)millimetre wave antenna technology for upcoming ESA missions”, *Proceedings of the AP-2000 Conference*, Davos, Switzerland, 2000, CD-ROM
- [2] P.R. Foster, D. Martin, C. Parini, A.V. Räisänen, J. Ala-Laurinaho, T. Hirvonen, A. Lehto, T. Sehm, J. Tuovinen, F. Jensen, K. Pontoppidan, “Mmwave antenna testing techniques - Phase 2”, 1996, *MAAS Report 304*
- [3] J. Habersack, W. Lindemer, H.-J. Steiner, ”High performance mm-wave measurements upto 200 GHz in the compensated compact range”, *Proceedings of the 2nd ESA Workshop on Millimetre Wave Technology and Applications: Antennas, Circuits and Systems*, WPP-149, Espoo, Finland, May 27–29, 1998, pp. 529–535
- [4] J. Hartmann, J. Habersack, H.-J. Steiner, J. Lemanczyk, P. de Maagt, “Calibration and verification measurements in compensated compact ranges up to 500 GHz”, *Proceedings of the 23<sup>rd</sup> Annual Meeting and Symposium of the AMTA*, Denver, CO., USA, Oct. 21–26, 2001, pp. 377–382
- [5] J. Tuovinen, A. Vasara, A.V. Räisänen, ”A new type of compact antenna test range”, *Proceedings of the 22<sup>nd</sup> European Microwave Conference*, Espoo, Finland, Vol. 1, 1992, pp. 503–508
- [6] D. Slater, P. Stek, R. Cofield, R. Dengler, J. Hardy, R. Jarnot, R. Swindlehurst, ”A large aperture 650 GHz near-field measurement system for the Earth Observing System microwave limb sounder”, *Proceedings of the 23<sup>rd</sup> Annual Meeting and Symposium of the AMTA*, Denver, CO., USA, Oct. 21–26, 2001, pp. 468–473
- [7] IEEE Standard Test Procedure for Antennas, *IEEE Std 149-1979*, IEEE Inc., 1979, 143 pages

- [8] A. Lehto, A.V. Räisänen, "Mikroaaltomittaustekniikka", in Finnish, 3. edition, Helsinki 1995, Otatieto Oy, 215 pages
- [9] G.E. Evans, "Antenna Measurement Techniques", Artech House, Boston, 1990, 229 pages
- [10] D. Slater, "Near-field Antenna Measurements", Artech House, Norwood, MA, 1991, 310 pages
- [11] A.D. Yaghjian, "An overview of near-field antenna measurements", *IEEE Transactions on Antennas and Propagation*, Vol. AP-34, No. 1, Jan. 1986, pp. 30–45
- [12] A.C. Newell, "Error analysis techniques for planar near-field measurements", *IEEE Transactions on Antennas and Propagation*, Vol. 36, No. 6, Jun. 1988, pp. 754–768
- [13] N. Erickson, V. Tolls, "Near-field measurements of the submillimetre wave astronomy satellite antenna", *Proceedings of the 20th ESTEC Antenna Workshop on Millimetre Wave Antenna Technology and Antenna Measurements*, WPP-128, Noordwijk, The Netherlands, June 18–20, 1997, pp. 313–319
- [14] A.D. Olver, "Compact antenna test ranges", *Proceedings of the 7th International Conference on Antennas and Propagation (ICAP)*, York, UK, 1991, pp. 99–108
- [15] C.G. Parini, C.J. Prior, "Radiation pattern measurements of electrically large antennas using a compact antenna test range at 180 GHz", *Electronics Letters*, Vol. 24, No. 25, Dec. 1988, pp. 1552–1554
- [16] C.G. Parini, M.R. Rayner, C. Rieckmann, "A millimetrewave compact antenna test range with a spherical main reflector", *Proceedings of the 2nd ESA Workshop on Millimetre Wave Technology and Applications: Antennas, Circuits and Systems*, WPP-149, Espoo, Finland, May 27–29, 1998, pp. 523–528
- [17] J.R. Descardecì, C.G. Parini, "Trireflector compact antenna test range", *IEE Proceedings – Microwave, Antennas and Propagation*, Vol. 144, No. 5, Oct. 1997, pp. 305–310
- [18] C.G. Parini, M. Rayner, C. Rieckmann, "Design and construction of a 200 GHz demonstrator of a trireflector compact antenna test range with spherical main reflector", *Proceedings of the 22nd ESTEC Antenna Workshop on Antenna Measurements*, WPP-164, Noordwijk, The Netherlands, May 11–12, 1999, pp. 147–152
- [19] A.D. Olver, A.A. Saleeb, "Lens-type compact antenna range", *Electronics Letters*, Vol. 15, No. 14, Jul. 1979, pp. 409–410
- [20] A.A.E.M. Saleeb, "Theory and Design of Lens-type Compact Antenna Ranges", *Doctoral Thesis*, Department of Electrical and Electronic Engineering, Queen Mary and Westfield College, London, 1982, 279 pages

- [21] W. Menzel, B. Huder, "Compact range for millimetre-wave frequencies using a dielectric lens", *Electronics Letters*, Vol. 20, No. 19, Sept. 1984, pp. 768–769
- [22] T. Hirvonen, J. Tuovinen, A.V. Räsänen, "Lens-type compact antenna test range at mm-waves", *Proceedings of the 21st European Microwave Conference*, Stuttgart, Germany, 1991, pp. 1079–1083
- [23] T. Hirvonen, J. Ala-Laurinaho, J. Tuovinen, A.V. Räsänen, "A compact antenna test range based on a hologram", *IEEE Transactions on Antennas and Propagation*, Vol. 45, No. 8, 1997, pp. 1270–1276
- [24] J. Ala-Laurinaho, T. Hirvonen, J. Tuovinen, A.V. Räsänen, "Numerical modeling of a non-uniform grating with FDTD", *Microwave and Optical Technology Letters*, Vol. 15, No. 3, 1997, pp. 134–139
- [25] J. Ala-Laurinaho, T. Hirvonen, A.V. Räsänen, "A 40 GHz CATR based on a hologram", *Proceedings of the 2nd ESA Workshop on Millimetre Wave Technology and Applications: Antennas, Circuits, and Systems*, WPP- 149, Espoo, Finland, May 27–29, 1998, pp. 542–547
- [26] T. Sehm, J. Ala-Laurinaho, T. Hirvonen, A.V. Räsänen, "Antenna measurements using a hologram CATR", *Electronics Letters*, Vol. 35, No. 10, May 1999, pp. 757–758
- [27] J. Ala-Laurinaho, T. Hirvonen, P. Piironen, A. Lehto, J. Tuovinen, A.V. Räsänen, U. Frisk, "Measurement of the Odin telescope at 119 GHz with a hologram type CATR", *IEEE Transactions on Antennas and Propagation*, Vol. 49, No. 9, Sept. 2001, pp. 1264–1270
- [28] T. Hirvonen, J. Ala-Laurinaho, A.V. Räsänen, "Performance analysis of a submillimeter wave hologram CATR", *Proceedings of the 27<sup>th</sup> European Microwave Conference*, Jerusalem, Israel, Sept. 8–12, 1997, pp. 681–686
- [29] T. Isernia, G. Leone, R. Pierri, "New approach to antenna testing from near field phaseless data: the cylindrical scanning", *IEE Proceedings-H*, Vol. 139, No. 4, Aug. 1992, pp. 363–368
- [30] R.G. Yaccarino, Y. Rahmat-Samii, "Phaseless bi-polar planar near-field measurements and diagnostics of array antennas", *IEEE Transactions on Antennas and Propagation*, Vol. 47, No. 3, Mar. 1999, pp. 574–583
- [31] R.G. Yaccarino, Y. Rahmat-Samii, "A comparison of conventional and phaseless planar near-field antenna measurements: the effect of probe position errors", *Proceedings of the 2000 IEEE Conference on Phased Array Systems and Technology*, Dana Point, CA, USA, May 21–25, 2000, pp. 525–528
- [32] O.M. Bucci, G. D'Elia, M.D. Migliore, R. Pierri, "Phaseless near-field measurements", *Proceedings of the 2001 IEEE International Symposium on Electromagnetic Compatibility*, Aug. 13–17, 2001, pp. 389–394

- [33] R.G. Yaccarino, Y. Rahmat-Samii, "Progress in phaseless near-field antenna measurement research at the University of California, Los Angeles", *Proceedings of the 2001 IEEE International Symposium on Antennas and Propagation*, Jul. 8–13, 2001, pp. 416–419
- [34] S. Costanzo, G. Di Massa, M.D. Migliore, "Integrated microstrip probe for phaseless near-field measurements on plane-polar geometry", *Electronics Letters*, Vol. 37, No. 16, Aug. 2001, pp. 1018–1020
- [35] K.S. Farhat, J.C. Bennett, A.J.T. Whitaker, N. Williams, "A millimetre wave semi-compact antenna test range", *Proceedings of the 8<sup>th</sup> International Conference on Antennas and Propagation*, Edinburgh, UK, 1993, pp. 384–387
- [36] K.S. Farhat, N. Williams, J.C. Bennett, "Hybrid techniques in antenna measurements: the semi-compact range", *Proceedings of the IEE Colloquium on Novel Antenna Measurement Techniques*, London, UK, 1994, pp. 10/1–4
- [37] C.R. Birtcher, C.A. Balanis, V.J. Vokurka, "RCS measurements, transformations and comparisons under cylindrical and plane wave illumination", *IEEE Transactions on Antennas and Propagation*, Vol. 42, No. 3, Mar. 1994, pp. 329–334
- [38] P.F. Goldsmith, N.R. Erickson, "Holographic measurements", Chapter 6-22 in book: J.D. Kraus, "Radio Astronomy", 2<sup>nd</sup> Edition, Cygnus-Quasar Books, Powell, Ohio, 1986
- [39] G. Junkin, T. Huang, J.C. Bennett, "Holographic testing of terahertz antennas", *IEEE Transactions on Antennas and Propagation*, Vol. 48, No. 3, Mar. 2000, pp. 409–417
- [40] R.C. Johnson, H.A. Ecker, J.S. Hollis, "Determination of far-field antenna patterns from near-field measurements", *Proceedings of the IEEE*, Vol. 61, No. 12, Dec. 1973, pp. 1668–1694
- [41] W.H. Carter, "On refocusing a radio telescope to image sources in the near field of the antenna array", *IEEE Transactions on Antennas and Propagation*, Vol. 37, No. 3, Mar. 1989, pp. 314–319
- [42] P. Goy, "Antenna vector characterization in the mm- and submm-wave regions", *Microwave Journal*, Jun. 1994, pp. 98–104
- [43] P. Goy, M. Gross, "Vector transceiver for mm-wave antennas", *Proceedings of the 20<sup>th</sup> ESTEC Antenna Workshop on Millimetre Wave Antenna Technology and Antenna Measurement*, WPP-128, Noordwijk, The Netherlands, June 18–20, 1997, pp. 289–294
- [44] P. Goy, M. Gross, S. Caroopen, "Millimeter and submillimeter wave vector measurements with a network analyzer up to 1000 GHz. Basic principles and applications", *Proceedings of the 4<sup>th</sup> International Conference on Millimeter and Submillimeter Waves and Applications*, San Diego, CA, USA, July 20–23, 1998, 25 pages

- [45] F.M. Gardner, “*Phaselock Techniques*”, 2<sup>nd</sup> Edition, John Wiley & Sons, Inc., New York, NY, 1979, 285 pages
- [46] U.L. Rohde, “*Microwave and Wireless Synthesizers: Theory and Design*”, John Wiley & Sons, Inc., New York, NY, 1997, 638 pages
- [47] B.-G. Goldberg, “*Digital Techniques in Frequency Synthesis*”, McGraw-Hill, Inc., New York, NY, 1996, 319 pages
- [48] P. Horowitz, W. Hill, “*The Art of Electronics*”, 2<sup>nd</sup> Edition, Cambridge University Press, 1995, 1125 pages
- [49] V.F. Kroupa, “Noise properties of PLL systems”, *IEEE Transactions on Communications*, Vol. Com-30, No. 10, Oct. 1982, pp. 2244–2252
- [50] G. Kantorowicz, P. Palluel, ”Backward wave oscillators”, Chapter 4 (pp. 185–212) in book: K.J. Button (Editor), “*Infrared and Millimeter Waves*”, Vol. 1, Academic Press, Inc., New York, NY, 1979
- [51] J. Neilson, L. Ives, M. Caplan, “Development of efficient backward wave oscillators for submillimeter applications”, *Proceedings of the 11<sup>th</sup> International Symposium on Space THz Technology*, Ann Arbor, MI, USA, May 1–3, 2000, pp. 296–303
- [52] Moscow State Pedagogical University, “*How to work with BWO*”, Instruction manual for BWO tubes OB-66, OB-65, OB-32, and OB-74, 8 pages
- [53] P.S. Henry, “Frequency-agile millimeter-wave phase lock system”, *Review of Scientific Instruments*, Vol. 47, No. 9, Sept. 1979, pp. 1020–1025
- [54] A. van Ardenne, E.E.M. Woestenburg, L.J. van der Ree, “350-GHz phase/frequency locked loop for use with a carcinotron backward wave oscillator”, *Review of Scientific Instruments*, Vol. 57, No. 10, Oct. 1986, pp. 2547–2553
- [55] A. Godone, E. Bava, C. Novero, “Phase lock of submillimetric backward-wave oscillators”, *IEEE Transactions on Instrumentation and Measurement*, Vol. 37, No. 3, Jun. 1989, pp. 794–798
- [56] S. Rosnell, J. Liukkonen, “*APLAC 7.0 System Simulation Manual: Part I PLL Simulations Using APLAC*”, HUT & Nokia Research Center, 1996, 31 pages
- [57] A. van Ardenne, W. Melis, ”Quasi-optical measurement of carcinotron phase noise at 350 GHz”, *Electronics Letters*, Vol. 24, No. 23, Nov. 1988, pp. 1411–1413
- [58] A.R. Harvey, G.M. Smith, J.C.G. Lesurf, “Phase noise measurements of a D-band backward wave oscillator”, *IEEE Microwave and Guided Wave Letters*, Vol. 4, No. 8, Aug. 1994, pp. 271–273
- [59] J. J. Krempasky, “Analysis of TEM mode on a curved coaxial transmission line”, *IEEE Transactions on Microwave Theory and Techniques*, Vol. 38, No. 6, June 1990, pp. 739–747

- [60] A. R. Thompson, J. M. Moran, G.W. Swenson, Jr., “*Interferometry and Synthesis in Radio Astronomy*”, John Wiley & Sons, Inc., New York, N.Y., USA, 1986, 534 pages
- [61] T. H. Legg, “Microwave phase comparators for large antenna arrays”, *IEEE Transactions on Antennas and Propagation*, Vol. AP-13, No. 3, May 1965, pp. 428–432
- [62] M. C. Thompson, Jr., L.E. Wood, D. Smith, W. B. Grant, “Phase stabilization of widely separated oscillators”, *IEEE Transactions on Antennas and Propagation*, Vol. AP-16, No. 6, Nov. 1968, pp. 683–688
- [63] A. G. Little, “A phase-measuring scheme for a large radiotelescope”, *IEEE Transactions on Antennas and Propagation*, Vol. AP-17, No. , Sept. 1969, pp. 547–550
- [64] T. M. P. Percival, A. C. Young, “Accurate digital control and rotation of the phase of microwave signals”, *IEEE Transactions on Instrumentation and Measurement*, Vol. 37, No. 4, Dec. 1988, pp. 626–630
- [65] L. R. D’Addario, “Time synchronization in orbiting VLBI”, *IEEE Transactions on Instrumentation and Measurement*, Vol. 40, No. 3, June 1991, pp. 584–590
- [66] L. Primas, R. Logan, G. Lutes, L. Maleki, “Distribution of ultra-stable reference frequency signals over fiber optic cable”, *Digest of the 1990 IEEE MTT-S International Symposium*, Vol. 1, May 8–10, 1990, Dallas, TX, USA, pp. 241–244
- [67] M. Shadaram, V. Gonzalez, J. Cenicerros, N. Shah, J. Mayers, S. Pappert, D. Lafaw, “Phase stabilization of reference signals in analog fiber-optic links”, *Technical Digest of the 1996 International Topical Meeting on Microwave Photonics*, Kyoto, Japan, Dec. 3–5, 1996, pp. 229–232
- [68] D.J. van Rensburg, “A technique to evaluate the impact of flex cable phase instability on mm-wave planar near-field measurement accuracies”, *Proceedings of the 22<sup>nd</sup> ESTEC Antenna Workshop on Antenna Measurements*, WPP-164, ESTEC, Noordwijk, NL, May 11–12, 1999, pp. 163–166
- [69] J. Tuovinen, A. Lehto, A.V. Räisänen, ”A new method for correcting phase errors caused by flexing of cables in antenna measurements”, *IEEE Transactions on Antennas and Propagation*, Vol. 39, No. 6, June 1991, pp. 859–861
- [70] R. W. Lampe, “Compensation of phase errors due to coaxial cable flexure in near-field measurements”, *Digest of the 1990 IEEE AP-S International Symposium*, Vol. 3, May 7–11, 1990, Dallas, TX, USA, pp. 1322–1324
- [71] Huber+Suhner Coaxial Cable Division, “Suhner Sucoflex™: the flexible microwave cable”, *Product Guide*, 142 pages
- [72] A. Lehto, J. Tuovinen, A.V. Räisänen, ”Reflectivity of absorbers in the 100–200 GHz range”, *Electronics Letters*, Vol. 27, No. 19, Sept. 1991, pp. 1699–1700

- [73] A. Lehto, J. Tuovinen, A.V. Räsänen, "Reflections in anechoic chambers in 100–200 GHz range", *Electronics Letters*, Vol. 27, No. 19, Sept. 1991, pp. 1708–1709
- [74] R.H. Giles, A.J. Gatesman, J. Fitzgerald, S. Fisk, J. Waldman, "Tailoring artificial dielectric materials at terahertz frequencies", *Proceedings of the 4<sup>th</sup> International Symposium on Space THz Technology*, Apr. 1993, Los Angeles, CA.
- [75] S. Janz, D.A. Boyd, R.F. Ellis, "Reflectance characteristics in the submillimeter and millimeter wavelength region of a vacuum compatible absorber", *International Journal of Infrared and Millimeter Waves*, Vol. 8, No. 6, 1987, pp. 627–635
- [76] B.E. Prewer, B. Milner, "Radiation absorber and method of making it", *U.S. Patent # 4,942,402*, Jul. 17, 1990
- [77] R.H. Giles, J.C. Dickinson, J. Waldman, W.E. Nixon, "Evaluation of submillimeter-wave anechoic materials at 500 GHz", *Project Report*, Submillimeter Technology Laboratory, University of Massachusetts Lowell, Feb. 1995, 20 pages
- [78] T.O. Klaassen, M.C. Diez, J.H. Blok, C. Smorenburg, K.J. Wildeman, G. Jakob, "Optical characterization of absorbing coatings for sub-millimeter radiation", *Proceedings of the 12<sup>th</sup> International Symposium on Space THz Technology*, Feb. 2001, San Diego, CA., USA, pp. 400–409
- [79] B.T. DeWitt, W.D. Burnside, "Electromagnetic scattering by pyramidal and wedge absorber", *IEEE Transactions on Antennas and Propagation*, Vol. 36, No. 7, July 1988, pp. 971–984
- [80] C.-F. Yang, W.D. Burnside, R.C. Rudduck, "A doubly periodic moment method solution for the analysis and design of an absorber covered wall", *IEEE Transactions on Antennas and Propagation*, Vol. 41, No. 5, May 1993, pp. 600–609